UNIVERSIDAD DE CONCEPCIÓN
FACULTAD DE CIENCIAS FÍSICAS Y MATEMÁTICAS

The Cosmic Dust Experiment CODE

Development of a single nanoparticle non-destructive mass spectrometer for astrochemical studies

By: Nicolás Antonio Martínez Sepúlveda

Tesis presentada a la Facultad de ciencias físicas y matemáticas de la Universidad de Concepción para optar al grado académico de Doctor en Ciencias con Mención en física

Agosto 2025
Concepción, Chile

Advisor: Stefano Bovino

AGRADECIMIENTOS

A mis amigos, familia y mi Fernanda, sin su apoyo esta tesis no habria sido posible.

Al equipo de CODE, el laboratorio LAMP y laboratorio Cepia quienes fueron invaluables en el desarrollo de este proyecto

Resumen

Esta tesis presenta el diseño e implementación de un espectrómetro de masa no destructivo, con un sistema de injeccion triboelectrico para el estudio de propiedades físico-químicas en el superficie de nanoparticulas de silica con un enfoque astroquímico. Se presenta como introducción conceptos claves para entender la motivación y contexto astroquímico del experimento, enfocándonos a procesos asociados al polvo interestelar, para pasar a las bases teoricas de manipulacion de iones que embarca la base técnica del funcionamiento del experimento CODE. Luego se presenta el experimento, detallando los distintos sistemas que lo conforman (trampa de iones, sistema optico, cámara de vació, sistema de injeccion,etc) y el trabajo realizado tanto experimental como simulaciones y teórico para llegar al estado en el que se encuentran actualmente. Luego se continua con los pruebas de funcionamiento que le dan validez experimental tanto a cada sistema por separado como a el experimento en su conjunto. Finalmente se presenta el trabajo futuro del experimento para poder avanzar en su capacidad de medir procesos físico químicos en la superficie de nanoparticulas

Keywords – Mass spectroscopy, Astrochemistry, ion manipulation

Abstract

This thesis presents the design and implementation of a non-destructive mass spectrometer, with a triboelectric injection system, for the study of physico-chemical properties on the surface of silica nanoparticles with an astrochemical focus. Key concepts for understanding the motivation and astrochemical context of the experiment are presented as an introduction, focusing on processes associated with interstellar dust. This leads into the theoretical foundations of ion manipulation that form the technical basis for the operation of the CODE experiment. The experiment is then presented, detailing the various systems that comprise it (ion trap, optical system, vacuum chamber, injection system, etc.) and the work performed, both experimental and through simulations and theory, to reach its current state. This is followed by the operational tests that provide experimental validation for each system individually, as well as for the experiment as a whole. Finally, the future work for the experiment is presented, aimed at advancing its capacity to measure astrochemical processes on the surface of nanoparticles.

Keywords – Mass spectroscopy, Astrochemistry, ion manipulation

Contents

List of Tables

List of Figures

Chapter 1

Introduction

1.1 Astrochemistry & Laboratory astrochemistry

Dust particles, although a small percentage of the composition of the Interstellar medium (ISM), play an important role in the physical and chemical properties of the ISM. In this section, I will review the role that dust plays in the evolution of the ISM and how these processes are studied experimentally in other laboratories across the world.

Laboratory astrophysics bridges studies of atomic and molecular species in interstellar and circumstellar media and planetary atmospheres conducted through astronomical observations, and studies of these species or their analogues that we can create in the laboratory and probe *in situ*. Laboratory astrophysics provides spectroscopic fingerprints of species that are necessary for decoding astronomical spectra and allows us to study physical-chemical processes in the conditions of cosmic environments. It helps to comprehensibly understand these processes and to build reliable astrochemical models that, being supported by astronomical observations, can reveal our astrochemical past and future.

1.1.1 Dust particles in the ISM

The following section is based on the 2021 review by Alexei Potapov (Potapov and McCoustra, 2021).

Dust grains play a key role in the physics and chemistry of the ISM. It is only

around 1% of the mass of the ISM and about 0.1% of the mass of the galaxy, however it influences the optical and thermal properties of the ISM by absorption and re-emision of light from stars, it acts as a surface on which chemical reactions occur such as the formation of H_2, additionally it plays a key role as the precursor material for comets-asteroids and planets.

1.1.1.1 Formation & and Composition of Dust

The Formation of interstellar dust is still not a fully understood process; however, one of the main formation pathways is via gas-phase reactions in the envelope of evolved AGB stars (Tielens, 2022). This high-temperature environment has high quantities of oxygen, silicon and carbon, the main components found in interstellar dust. In oxygen rich stars ($n(O)/n(C) > 1$) oxygen reacts with silicon and other metals to form silicate grains and other crystalline oxides whereas in carbon-rich stars ($n(O)/n(C) < 1$) carbon is not predominantly trapped as carbon monoxide and can form graphite or amorphous carbon grains Ventura et al. (2012). Grains formed in the stellar envelope escape from these environments by winds caused by radiation pressure, where it can be destroyed by supernova shocks from nearby stars. This process cannot account for the totality of the dust found in the ISM, so other, more efficient processes must account for the amount of interstellar dust found Criscienzo et al. (2013).

Dust can be divided into two main groups from its composition: carbonaceous and siliceous dust. Other types of dust exist, but it is a very low % of the dust found in the ISM. Silicate dust is the most abundant form of dust in the ISM, and almost all of it is in an amorphous form. These grains are the main contributors to dust emission in the ISM; their $Si-O$ $10\mu m$ stretching mode and $O-Si-O$ $18\mu m$ bending modes are consistently seen in absorption features across the galaxy. Carbonaceous grains exist in both crystalline and amorphous forms; it can also be found in the form of hydrocarbons such as polycyclic aromatic hydrocarbons.

Interstellar dust is generally approximated to be spherical or cylindrical. To reduce the complexity of computational studies; in reality, this is not the case. Dust grains in the ISM collide with each other, either shattering or sticking together. They can shatter due to the high-energy interactions with supernova shocks and cosmic radiation. This leads to random shapes and a wide range of sizes. Studying the polarisation of the interstellar radiation, we can deduce that a percentage of

larger grains are non/spherical and aligned.

Dust grains absorb and scatter much of the stellar radiation of our galaxy, about $30\% - 50\%$. This energy is then re-emitted as far-infrared continuum emission. By looking at the extinction curves of the ISM, we can see it rises from the near-IR to the near-UV, with a steep rise at 100 nm to the far-UV. This increase with the reduction of wavelength corresponds to an increase in the abundance of dust of corresponding sizes. The size distribution of dust are power laws that monotonically decrease with an increase in size. Additionally, observations have shown characteristic absorption and emission features of different materials that can be found as dust grains, such as graphites (broad $217.5\mu m$ absorption feature), PAHs Li and Draine (2012) ($3.3, 6.2, 7.7, 8.6, 11.3\mu m$ emission features). Larger grains of radius $r \sim 1\mu m$ have been detected entering the solar system by the Ulysses dust detector. Even larger grains with $r \sim 10\mu m$ have been detected by radar methods.

All of the destruction and agglomeration processes of dust make ISM dust particles very porous Sabri et al. (2013), Ossenkompf (1993), as shown by analysis of cometary dust particles, dust evolution models and laboratory experiments. This research showed that dust in all environments (protoplanetary disks, protostellar envelopes and interstellar clouds) has very high porosities of $\sim 80\%$.

1.1.1.2 Dust in cold environments

Dust grains can be found in cold molecular clouds where temperatures can go as low as 10 K. In these environments atoms and molecules present in the gas such as H, O, C, N and S will absorb onto the dust grains forming ices. In these conditions, molecule formation can occur. Atoms with high enough energy will move across the surface of the dust until they meet other atoms and react forming basic molecules such as H_2 and H_2O (H_2O ice is one of the most abundant ices observed in the ISM and H_2 on of the most abundant molecules in the ISM). In clouds with higher density, where other molecules can be found in gas phase, such as CO and N_2, icy mantles will form from a variety of molecules such as CO, CO_2, NH_3, CH_4, and CH_3OH. One could imagine that these molecules are frozen in time, trapped in these ices, yet this is far from the truth. Extensive chemical networks are formed in these ices, producing a variety of complex organic molecules (COMs) such as alcohols, amines and aldehydes (within the astrophysics

community carbon bearing molecules larger than 6 atoms are considered complex organic molecules).

Gas-surface interactions between molecules in the ISM is described by three processes: Adsorption, desorption and diffusion. These processes are influenced by both the composition of the dust grain as well as its size and shape.

Adsorption

Adsorption can be divided into two sub-categories, *chemisorption* and *physisorption*. Chemisorption describes an adsorption guided by the transfer of electrons and the formation of covalent bonds between the dust surface and the adsorbate, whilst physisorption is a lower energy process that is determined by van der Waals interactions and hydrogen bonding. Both of these interactions are moderated through a potential energy surface (PES). We will focus on physisorption since it is most relevant for the cold environments of molecular clouds.

Physisorption is a barrierless process, which means that the desorption energy E_{des} is equal to the adsorption energy E_{ads}. This is in contrast to chemisorption, where some reactions require an activation energy and $E_{des} = E_{act} + E_{ads}$.

When studying adsorption, we can consider that the interaction between the gas phase and the surface can be described as a balance of fluxes to and from the grain surface J_{in} & J_{des} Here J_{in} can be described using the classical wall collision rate shown in Fig. 1.1.1:

$$J_{in} = Z_w = \frac{P}{\sqrt{2\pi m k_b T}} = \frac{nRT}{\sqrt{2\pi MRT}} \tag{1.1.1}$$

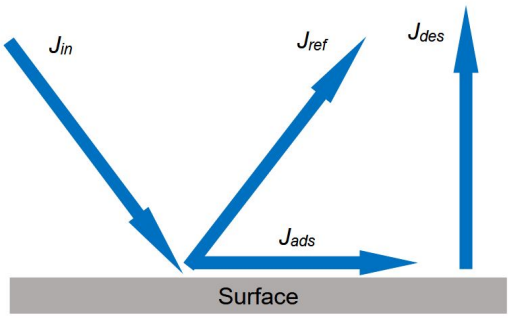

Figure 1.1.1: Balance of flux on a surface. J_in is the input flux, J_{ref} is the reflected flux, J_{ads} is the adsorbed flux and J_{des} the desorbed flux

Here P is the partial pressure of a gas of molecular mass m at a temperature T and M is the molar mass. We can then define the sticking coefficient S as the relation between the input flux and the rate of adsorbed particles.

$$S = \frac{J_{ads}}{J_{in}} \tag{1.1.2}$$

If we now consider that there is an additional desorption rate J_{des}, we can define the accommodation coefficient α as:

$$\alpha = \frac{J_{abs} + J_{des}}{J_{in}} \tag{1.1.3}$$

We can see that α and S will be equal in the absence of desorption. Measuring these values is crucial for understanding the adsorption rates of molecules onto surfaces.

When measuring adsorption, one can expect that this value will not be constant on a surface; S or α will vary as the binding sites on the surface are filled and after reaching a monolayer coverage. If we follow the Langmuir adsorption model, we can then define the sticking coefficient as:

$$S = S_0 \left(1 - \frac{n_{ads}}{n_{ads,mono}}\right) \tag{1.1.4}$$

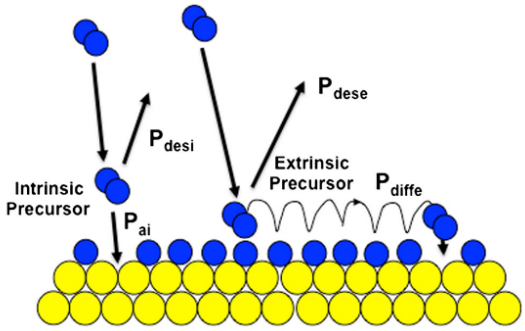

Figure 1.1.2

Here $n_{ads,mono}$ is the full coverage of a mono layer and the ratio $\frac{n_{ads}}{n_{ads,mono}}$ is commonly known as θ coverage, and S_0 is the initial sticking probability. However, this is rather simplistic in its approach to the various conditions when adsorbing molecules. In 1957, P. Kisluk developed a model for chemisorption where two precursor states to chemisorption exist. Intrinsic and Extrinsic precursors. Intrinsic precursors are molecules that physisorbed onto an available chemisorption site, and extrinsic precursors are molecules that physisorbed onto an occupied site, as shown in Fig. 1.1.2, and will need to diffuse onto an unoccupied site before chemisorbing.

We will then have to consider the diffusion rate of the extrinsic precursors to empty sites when calculating the adsorption rateBowker (2016). We can then expand on equation 1.1.4 as:

$$S = S_0 \left[\frac{1 - \frac{n_{ads}}{n_{ads,mono}}}{1 + (K-1)\frac{n_{ads}}{n_{ads,mono}}} \right] \tag{1.1.5}$$

$$K = S_0 P_{des} / P_{ads} \tag{1.1.6}$$

Here K is the equilibrium constant, and P_{des} and P_{ads} are the probability of desorption for an extrinsic precursor and the probability of adsorption for an intrinsic precursor, respectively. When the equilibrium constant is very small, there is a large extrinsic precursor effect that maintains the values of S high even at high coverages.

For large values of S or α, the Kings and Wells method is the standardised, historical way of studying sticking coefficient and the accommodation coefficient.

This method measures these values by comparing the gas inflow in a calibrated chamber with the pressure of said chamber. The difference between these values will correspond to the adsorbed gas. Since this method uses some considerable assumptions and estimations, such as a constant pumping pressure and an estimation of adsorption on other surfaces in the experiment, it is not well-suited for high precision measurements. For more precise measurements, the construction of adsorption isotherms using systems like XPS & RAIR can be used to measure precise coverage of surfaces as a function of time for a fixed gas flow and temperature. By studying adsorption isotherms, one can also predict the binding energy of molecules, as shown in Kumar et al. (2019). The simplest method is by using the Langmuir adsorption isotherm equation:

$$q_h = \frac{NKp_e}{1 + Kp_e} \tag{1.1.7}$$

Here q_h is the amount of molecules adsorbed onto a homogenous surface, N the amount of binding sites, p_e the pressure at equilibrium and K is the binding energy for said sites.

Diffusion

As mentioned previously, adsorbed molecules on a surface can diffuse. This process is a fundamental part of surface reactivity. Classically, we can explain this phenomenon as the adsorbed molecule hopping randomly between sites from potential well to potential well.

Quantum mechanically, this process can be explained in more detail. Particles within a potential can move within their restricted and frustrated translations (frustrated translations are restricted motions of particles within the potential well of the binding site) or, if energised enough, can move above the barrier energy in free diffusion. An alternative means of diffusion over the barrier, barrier hopping, is resonant tunnelling through the barrier, if we accept the continuity of the wave functions of each energy level across potential barriers.

Desorption

Now that we have discussed both adsorption and diffusion, the final "movement" phenomenon we must discuss before reaching chemical reactions is desorption. In the context of astronomy, the most studied method of desorption is thermal desorption; however, other types of desorption processes exist as chemical desorption and photo desorption.

Thermal desorption

Most of the experimental measurements of binding energies E_{bind} are done by thermal desorption, specifically by temperature programmed desorption experiments (TPD experiments). The binding energies of the adsorbates are calculated using the Polanyi-Wigner equation:

$$r_{des} = \frac{dn_{ads}}{dt} = v(n_{ads})^m e^{-E_{bind}(n_{ads})/RT} \tag{1.1.8}$$

Here r_{des} is the desorption rate, v is the surface concentration dependent pre-exponential factor, m is the order of desorption, E_{bind} is dependent on the interaction, either it will adsorb onto the surface or on top of a pre-existing layer of adsorbate. To correctly measure binding energies using this method, it is crucial to correctly characterise the order of desorption present in the system. For systems

of astrophysical interest, we can safely consider only two modes, zero-order and first-order desorption. First-order desorption is seen at the mono/sub-mono layer, and zero-order desorption is given by multi-layer desorption. In TPD experiments, the amount of adsorbate desorbed from the surface is usually characterised by mass spectrometer data, when looking at the concentration signal from the temperature vs mass signal graphs, examples shown in Fig. 1.1.3, zero and first order desorption can be identified.

Zero-order desorption, in contrast, will reach its peak at higher temperatures with increasing surface concentration. First-order desorption can be identified by a fixed temperature for the peak desorption with varying surface concentration whilst maintaining the condition of mono/sub-mono layer concentration and a small variation of binding sites (considering only small variations of E_{bind} for different sites). When the surface presents a large heterogeneity, which has been found to be the more common condition as previously thought, E_{bind} is then no longer a single value, and we must then define a new equation for E_{bind}. We then apply a direct inversion of the Polanyi-Wigner equation:

$$E_{bind} = -RT \ln \left(\frac{dn_{ads}/dt}{v n_{ads}(t)^m} \right) \tag{1.1.9}$$

we can determine $n_{ads}(t)$ if we have a precise deposition system by multiplying the rate of bombardment or deposition Z_W with the dose time τ

$$n_{ads} = Z_W \tau = \frac{PS\tau}{\sqrt{2\pi m k_B \tau}} \tag{1.1.10}$$

Here Z_W is the wall collision rate from Eq. 1.1.1. If the deposition is done at low temperatures, then the desorption rate for the deposition can be considered low and the sticking coefficient close to unity. More complex models exist, such as the extended inversion method from Smith et al., where the surface-dependent pre-exponential factor is also made variable $v_{des} \sim 10^{12\pm10} s^{-1}$. In all of these methods, E_{bind} is measured for every sub mono layer dose and a E_{bind} vs n_{ads} graph. From here, a fit is made to the averaged E_{bind} vs n_{ads} data to obtain a

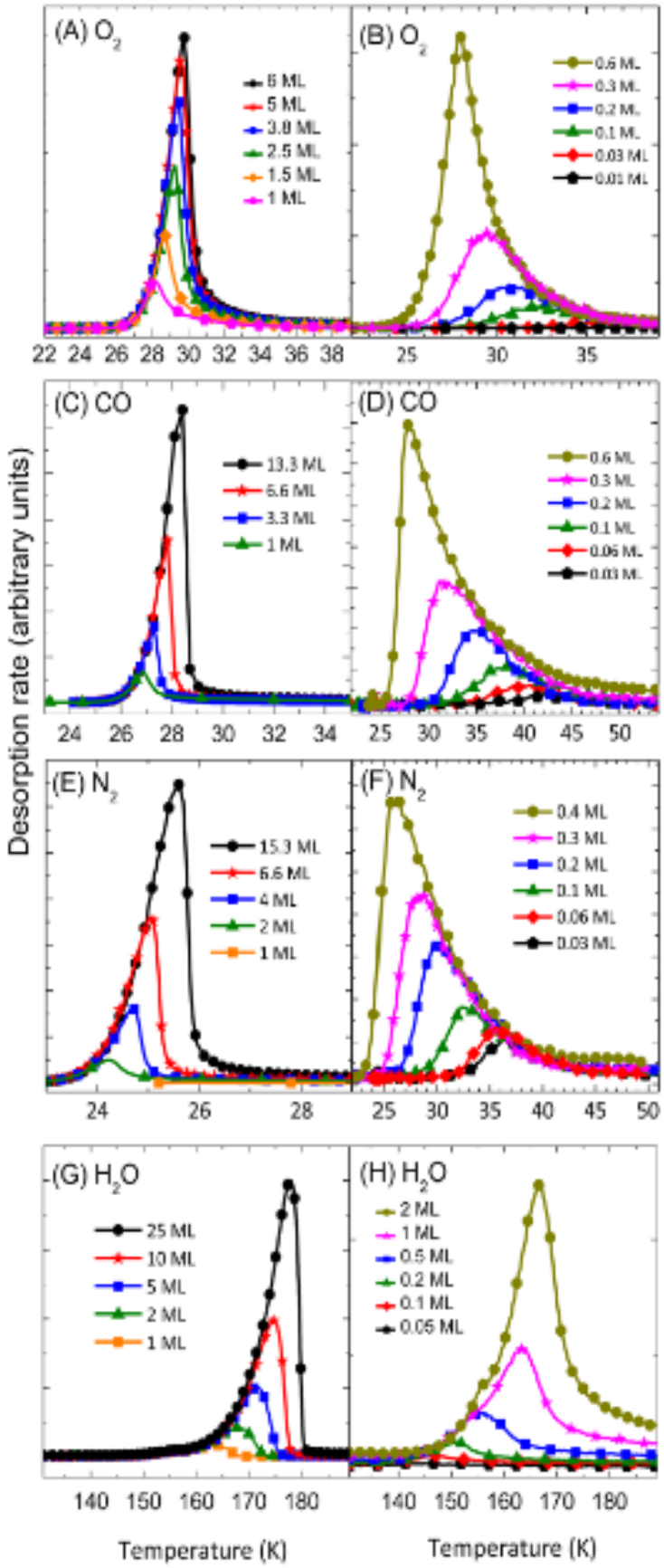

Figure 1.1.3: TPD profiles for some simple molecules such as O_2, CO, N_2, H_2O. Graphs A through F show typical behaviour for first-order desorption, whilst graphs G and H show behaviour more keen to zero-order desorption.

function for $E_{bind}(n_{ads})$.

Chemical desorption

This desorption process refers to a desorption product of the excess energy from a chemical reaction; as such, it is also referred to as reactive desorption. Garrod and Herbst (2006) used the Rice-Ramsperger-Kessel (RRK) theory to model this process, they model the surface molecule bond as an additional vibration mode to obtain a probability P for an energy E larger than the binding energy E_{bind} of the molecule to be present in the bond from the reaction energy E_{reac}:

$$P = \left[1 - \frac{E_{bind}}{E_{reac}}\right]^{s-1} \tag{1.1.11}$$

Here s is the number of vibrational modes of the molecule-surface bond system, if the molecule is diatomic s=2 for all other amounts $s = 3N - 5$. We can then consider that in a real scenario, this energy will not always mean that the molecule will desorb, as this is not the only means by which this excess energy can dissipate. For a hypothetical scenario in which this is the only means of dissipation, we can relate this probability to the desorption rate as $v_r = vP$, where v is the frequency of the surface molecule bond. For a more realistic scenario, we consider that the energy can be dissipated by the surface. We can then define a rate v_s at which the energy is dissipated by the surface. We then have that the fraction of reactions that desorb the bound molecule is:

$$f = \frac{vP}{v_s + vP} = \frac{aP}{aP + 1} \tag{1.1.12}$$

where a is the ratio of surface bond frequency vs the energy dissipation rate $a = v/v_s$. Garrod and Herbst (2006) results show that a will have a low value ~ 0.01; furthermore, his results show that this process is indeed useful for explaining gas phase abundance of molecules such as methanol.

Photo desorption

Far ultraviolet (FUV) photons interact with adsorbed ices on the surface of dust

particles in the ISM; this interaction induces various processes on the ices, such as photodissociation and photo desorption. Photo desorption is an important process to desorb molecules into the gas phase in conditions where thermal desorption is not an efficient method of desorption. This process only occurs on the topmost layers of the solid, so its photodesorption rate is unaffected by ice thickness. The UV radiation can come from different sources depending on the conditions of the ISM. In dark molecular clouds the FUV radiation can come from the excitation of H_2 molecules by cosmic rays, in weak photodissociation regions there is no internal source of radiation rather it comes from external sources, in star forming regions the radiation will come for the forming stars, however in these regions thermal desorption will dominate in all but the farthest portions of the stellar envelopes.

Photodesorption rates in astrochemical studies has a fairly straightforward approachCuppen et al. (2017), photodesorption yields (Y_x in molecules per photon) for molecules is experimentally determined, then the photo desorption rate will be given by the flux of FUV radiation photons $\mathrm{cm}^{-2}\,\mathrm{s}^{-1}$, the cross sectional area of the grain surface per unit volume $\sigma_g n_g$, and the surface fraction of the molecule in the first two monolayers $\theta_X = n_X/n_s$. We then have a desorption rate given by:

$$k_X^{pd} = \theta_X Y_X n_g \sigma_g F_{UV} \quad cm^{-3}s^{-1} \tag{1.1.13}$$

Here n_d is the number density of grains, σ_g is their geometrical cross section, and n_X is the number density of species X. If wavelength-dependent data for the photodesorption yield exists, then the total photodesorption yield for the FUV can be defined as:

$$Y_X = \int_\lambda Y_X(\lambda) F_{UV}(\lambda) d\lambda \tag{1.1.14}$$

Wavelength-dependent data is available for only some molecules, such as CO, N_2, O_2 and CO_2. In the process of photodesorption, there is an alternative method of desorption called co-desorption or the "kickout" method in which a desorbed or photodisociated species has enough energy to remove another molecule from the ice

by collision, this process is parallel to both photodesorption and photodisociation, as such we can see that radiation induced processes in the surface of ices are very complex and sensible.

Photodissociation is a process in which a molecule is broken down by the absorption of a photon. This phenomenon is an important driver for chemical reactions in interstellar ices and has been used to explain chemical complexity found in the ISM. Ices in the ISM are optically thin to FUV radiation, so photodissociation can occur in any layer of the ice. When modelling photodissociation, its rate for specific species is given by integrating the photodissociation cross section with the FUV spectrum along the wavelength:

$$\int_{\lambda} \sigma_X(\lambda) F_{UV}(\lambda) d\lambda \tag{1.1.15}$$

By treating photodissociation and photodesorption processes as parallel, models for solid phase chemistry on dust particles can account for the production of reactive radicals both within and on the surface of the ice mantle. The models also include loss of radicals to the gas phase or by reaction with other radicals.

Chemical reactions

Now that we have discussed adsorption, diffusion, and desorption, we can begin the discussion on surface chemistry. The efficiency of chemical reactions will depend on the type of reactions and the conditions of the environment, such as the morphology of the surface, the number of monolayers, the number of species, temperature, and molecule abundances. There are three common types of reactions in the context of chemical reactions on the surface of dust in astrophysics. Eley-Rideal reactions, Langmuir-Hinshelwood reactions, and Kasemo-Harris reactions.

Eley-Rideal reactions are the simplest of the three. It is a reaction of an adsorbed molecule with a gas-phase molecule as shown in fig1.1.4. We can write it as a chemical equation as

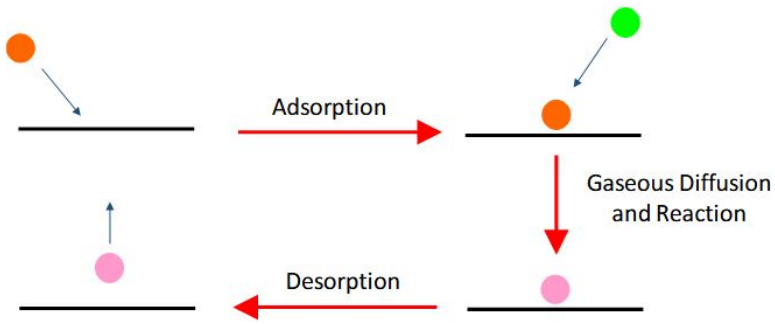

Figure 1.1.4: Sketch of Eley Rideal reactions

$$\mathrm{A(ads)} + \mathrm{B(gas)} \longrightarrow \mathrm{C(Product)} \tag{1.1.16}$$

and its reaction rate

$$v_r = k_{er}\theta_A P_B \tag{1.1.17}$$

Here θ_A is the surface concentration of the reactant A and P_B is the gas pressure of reactant B; we can expand this by applying the Langmuir isotherm equation for surface concentration and applying it to the reaction rate.

$$\theta_A = \frac{b_A P_A}{1 + P_A b_A} \tag{1.1.18}$$

$$v_r = k_{er}\frac{b_A P_A P_B}{1 + P_A b_A} \tag{1.1.19}$$

If we consider astrophysical conditions such as low pressure and low surface concentrations, we are left with a reaction rate as:

$$v_r = k_{er} b_A P_A P_B \tag{1.1.20}$$

Langmuir-Hinshelwood reactions refer to reactions from one or two adsorbed molecules, as shown in Fig. 1.1.5. Here, one molecule can decompose into smaller molecules or vice versa. In the case of a single molecule, the reaction equation and reaction rate are

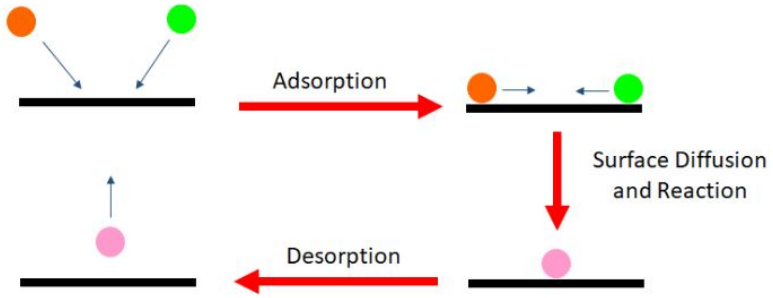

Figure 1.1.5: Sketch of the Langmuir Hinshelwood reaction

$$\mathrm{A(ads)} \longrightarrow \mathrm{C(Products)} \tag{1.1.21}$$

$$v_r = k_{LHuni}\theta_A \tag{1.1.22}$$

$$v_r = k_{LHuni}\frac{b_A P_A}{1 + b_A P_A} \tag{1.1.23}$$

If we consider again astrophysical conditions, we get a reaction rate of:

$$v_r = k_{LHuni} b_A P_A \tag{1.1.24}$$

In the latter case, when the Langmuir-Hinshelwood reactions involve two different molecules, we would have:

$$\mathrm{A(ads)} + \mathrm{B(ads)} \longrightarrow \mathrm{C(Products)} \tag{1.1.25}$$

$$v_r = k_{LHbi}\theta_A\theta_B \tag{1.1.26}$$

$$v_r = k_{LHbi}\frac{P_A P_B b_A b_B}{(1 + b_A P_A + b_B P_B)^2} \tag{1.1.27}$$

Here we can see a few different versions of the reaction rate. First, we can consider

a base astrophysical environment, a low concentration of both reactants. Here we would have:

$$v_r = k_{LHbi} P_A P_B b_A b_B \tag{1.1.28}$$

Here, the dependence of the reaction rate is of first order for both reactants. In the case in which one of the reactants is in much higher abundance than the other, let us say B is much lower than A:

$$v_r = k_{LHbi} \frac{b_A b_B P_A P_B}{(1 + b_A P_A)^2} \tag{1.1.29}$$

The reaction then would have a maximum for the pressure of reactant A and would be first order for reactant B.

The last reaction, the Kasemo and Harris reaction, is a hot-atom surface reaction. These hot atoms can come mainly from two sources, either from photodissociation of a larger molecule or, remembering from the adsorption phenomenon, an extrinsic adsorption in which the adsorbant has not bound to a site yet, as shown in Fig. 1.1.6.

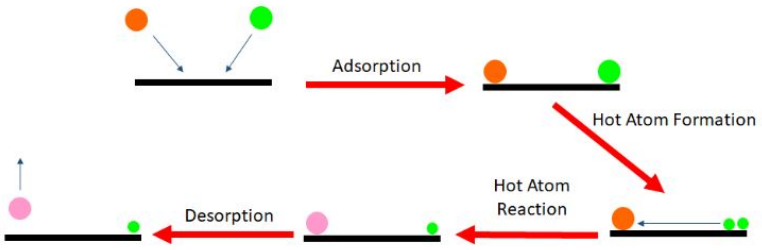

Figure 1.1.6: Sketch for a Kasemo Harris hot atom reaction

This type of reaction is more complex, from Kammler et al. (2000) we know that we must consider the diffusion process of hot atoms, there will be a probability associated with the hot atom sticking (p_s) to a binding site or reacting (p_r) the relationship between this two probabilities will define the reaction, if the ratio p_r/p_s is close to 1, the reaction will be similar to Eley-Rideal reactions, if the

ratio is small then these reactions will be starchly different from an Eley-Rideal reaction. The model used by Kammler for the hot atom reaction in the case when p_r/p_s is low is:

$$v_r = \sigma\Phi\theta_{b0}e^{-\sigma\Phi t} \tag{1.1.30}$$

Here σ is the reactive cross section, Φ the flux of reactant A and θ_{b0} the surface coverage of reactant B at a time t=0. In Kammler's work, this equation is used for the study of hot-atom H-D reactions. In this case, either of the reactants can be the hot atom depending on the gas-surface reactions previous to the diffusion.

1.1.1.3 Experimental astrochemistry

As mentioned, laboratory astrochemistry is the third point in the triangle that is astrochemical studies. On one corner, we have observations, probably the most important aspect of these studies, since it is observations that show the conditions of the ISM, what species we can find and where. Theoretical models are the second corner of this triangle: theoretical work gives us a glimpse into the underlying processes that we observe and allows us to view astronomical processes in both time scales and resolution that are not possible to view in observations. Our final corner is experimental analysis. Computational models are not able to correctly recreate astronomical conditions without proper experimental data, real measurements of values like desorption and photodissociation rates, binding energies and chemical reactions. This data is not obtainable without experimental work; therefore, this area is the last cornerstone for our current understanding of astrochemistry.

In this subsection, we will present some experiments relevant to this thesis that exist or have existed around the world. This is only a brief list of many more experiments, such as Ioppolo et al. (2013), Santoro et al. (2020) and Potapov et al. (2020), to give insight into the work done in this area.

Interaction of electrons and molecules with a single trapped nanoparticle Schlemmer et al. (2004)

Schlemmer's experiment is a direct predecessor to the CODE experiment, and

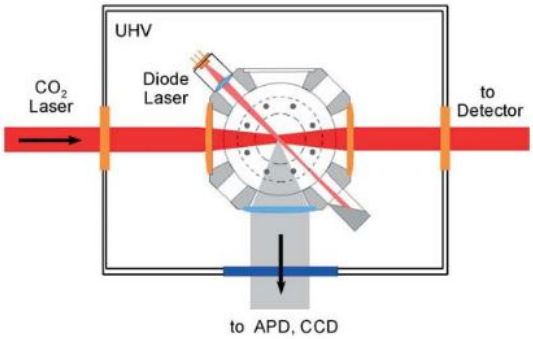

Figure 1.1.7: Sketch of the experiment, shown from a top view. both the heating and the illumination laser are shown.

as such, our work is inspired greatly by its design. This experiment is also a nanoparticle mass spectrometer built upon an ion trap. The experiment consisted of an octopole ion trap placed in a vacuum with a continuous monitoring system in the form of an optical detection system that measures the light scattered by the trapped nanoparticle. A large viewing angle of $0.6\,sr$ was used to maximise the amount of scattered light collected by the system. The trap's geometrical parameters are $z_0 = 5.50\,mm$ and $r_0 = 7.77\,mm$. Only the top and bottom end caps are energised by an AC power source; the 8 rods are energised with a DC potential, with an opposing pair of rods charged identically. this allows for control over the particles position in the X, Y plane as shown in Fig. 1.1.7 the system usually works with a AC voltage of $\sim 750\,V$ and AC frequency of $500\,Hz$. The system uses a $635\,nm$ 50 mW light source placed inside the vacuum chamber to reduce micromotions.

Particles are injected by using a UHV compatible speaker that vibrates at 1.5 kHz with an amplitude of $100\,\mu$m the particles injected are 500 nm SiO_2 particles reach a maximum height of 10 cm that corresponds to the centre of the ion trap to maximize trapping, the particles carry a few tens of positive charges. The light system splits the incoming light 50/50 to an APD system and a CCD camera for Fast Fourier Transform (FFT) analysis and control, respectively.

For charge stepping the experiment uses an electron gun aimed at the centre of the trap, and the temperature of the particle is controlled using a CO 10.6μm laser with a power output of $0.5 - 25$ W with a maximum intensity of $10^5\,\mathrm{W\,cm^{-2}}$, however such high power is not needed for the objective temperatures of the experiment. This laser system allows for quick heating of the nanoparticle without

heating the rest of the experiment, additionally, the experiment is capable of injecting various gases such as He, H_2 and air and can deposit C_{60} by using an oven to evaporate this material.

To set the temperature of the particle Schlemmer's experiment uses a calculated power output to estimate their desired temperature. The temperature T of the particles with radius r is calculated by balancing the absorbed power from the laser $P_{abs,laser}$, the power absorbed from the blackbody radiation of the surrounding chamber P_{abs,T_0}, to the radiation emitted from the particle $P_{em,T}$

$$P_{abs,laser} + P_{abs,T_0} = P_{em,T} \tag{1.1.31}$$

The power absorbed from the laser will be the output intensity of the laser I_{laser} and the absorption efficiency Q_{abs} for a particle of radius r within the Rayleigh limit.

$$P_{abs,laser} = Q_{abs} I_{laser} \pi a^2 \tag{1.1.32}$$

$$Q_{abs} = \frac{8\pi r}{\lambda} Im\left[\frac{m^2-1}{m^2+2}\right] \tag{1.1.33}$$

for laser power of $3\mathrm{W/cm^2}$ a SiO_2 nanoparticle of 500nm will absorb $\sim$ 100pW of power. The power emitted by the nanoparticle will be given by:

$$P_{em,T} = 4\pi r^2 \int_0^\infty d\lambda \varepsilon(\lambda, a) P_\lambda(T) \tag{1.1.34}$$

Here the spectral emissivity $\varepsilon(\lambda, r)$ is identical to the absorption efficiency Q_{abs} and $P\lambda(T)$ is Planck's black-body distribution function for the energy flux:

$$P_\lambda(T) = \frac{2\pi c^2}{\lambda^5 [e^{\frac{hc}{\lambda k T}} - 1]} \tag{1.1.35}$$

$T[K]$	$I[Wcm^{-}2]$
300	0.01
350	1.07
400	2.61
450	4.60
500	7.02

Table 1.1.1: Necessary IR laser intensity to heat the particle to temperature T

cooling via gas collision only accounts for 0.01pW for a helium gas pressure of 10^{-4} mbar so its considered negligible for the objective temperatures of $300-500K$. Table 1.1.1 shows a list of objective temperatures of the experiment and their corresponding laser intensity.

Mass determination of the trapped nanoparticle is done by charge stepping, charge step is done at low electron current to ensure charge steps of ne during 6 hours, particle mass was determined at 128 ± 0.02fg corresponding to a nanoparticle of size 497nm in agreement with the suppliers size distribution for 500 nm SiO_2 particles, Fig. 1.1.8 shows the charge stepping process for the mass determination.

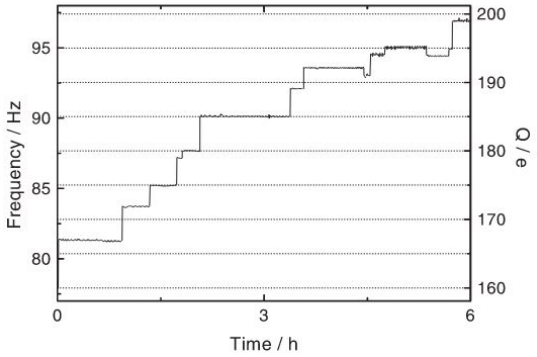

Figure 1.1.8: Charge stepping for mass determination, ω_r was measured to determine the absolute charge and mass. The charge Q is changed due to electron bombardment, and mass was determined by the smallest step size $\Delta Q = -e$ larger steps are due to secondary electron emission.

Schlemmer studied the secondary electron yield of the particle when bombarded with a calibrated electron gun. Their results are summarised in Fig. 1.1.9 showing a reduction of secondary electron emission with a C_{60} coating.

Millimetre/Submillimetre Spectroscopic Detection of Desorbed Ices: A New Technique in Laboratory Astrochemistry Yocum et al. (2019)

The experiment they designed was made to combine an ice analogue setup

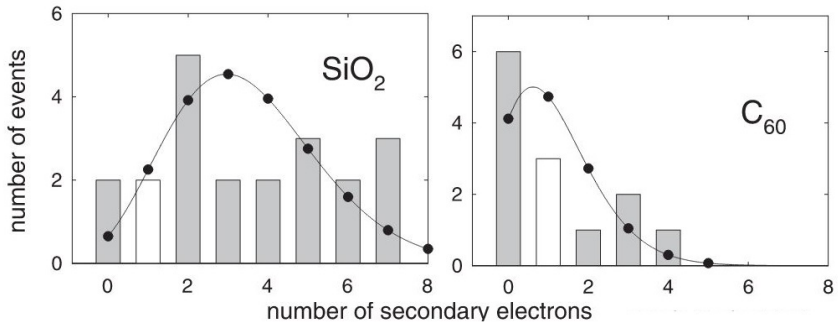

Figure 1.1.9: Secondary electron emission for a bare SiO_2 particle (left), and covered with a 40nm C_{60} (right). Solid lines are least-square fits of a Poisson distribution to the histogram data.

(i.e deposition of ices on a test substrate) with a millimetre/sub-millimetre spectrometer setup to study gas species thermal or photodesorption from ice films. This method has an advantage over traditional ice studies, where the desorbed species are studied via mass spectrometry. Mass spectrometry is insensitive to structural isomers; furthermore, solving this issue with isotopic substitutions can be problematic, as photodesorption yields for isotopologues are different.

The experiment consists of a vacuum chamber (1×10^{-9}Torr). Inside the chamber, a gold substrate is placed at the centre of the chamber connected to a cold head that can cool the sample down to $12K$ and can be heated up to $300K$. The millimetre/sub millimetre spectrometer has 3 frequency ranges (75-1000GHz, 1.8-1.9 THz and 2.5-2.6 THz). The chamber is also fitted with a $670nm$ laser that is aimed at the gold substrate at an angle of 29.4° for ice thickness measurement. The laser is reflected on the gold substrate and detected in a photodiode. To measure the ice thickness, the oscillations of the intensity of the laser are measured. These oscillations are induced by destructive and constructive interference caused by the formation of the ice layers on top of the substrate. The voltage from the photodiode creates an interference fringe pattern that is used to calculate the ice thickness using the Bragg equation:

$$d = \frac{m\lambda}{2\sqrt{n^2 - \sin^2\theta}} \tag{1.1.36}$$

The chamber is also fitted with a UV photolysis lamp for ice photolysis

($\lambda = 121.6$nm) and fine-control all metal gas dosing valves connected by capillary to the centre of the chamber for direct gas deposition on the substrate. The system also includes a UV photolysis lamp, a 670 nm laser diode, a residual gas analyser, and a fine-control gas-dosing valve to manipulate the samples. Fig. 1.1.10 shows a sketch of the design of the experiment.

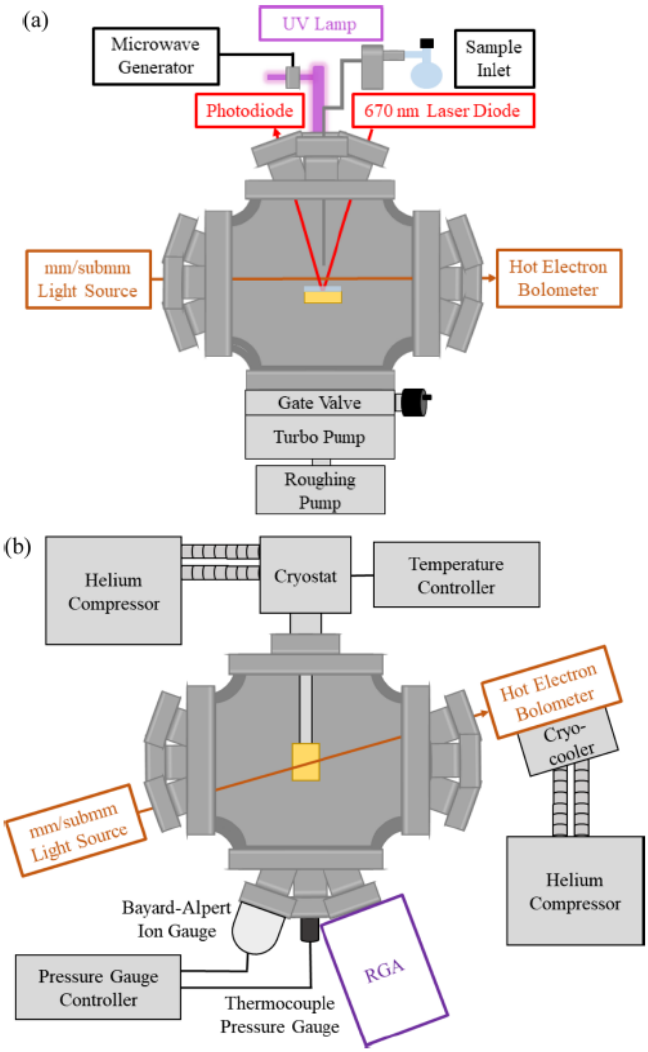

Figure 1.1.10: Schematics of the (a) side and (b) top views of the experimental setup.

The spectrometer system consists of 3 different systems, shown in Fig. 1.1.11. First, a signal generator emits radiation within the $0.000250 - 50$ GHz. The frequency range is then amplified by a set of multipliers to reach the intended frequency range. The radiation is then focused into the chamber passing $\sim 1 - 2$ cm above the substrate by a Teflon lens and is then focused again after exiting the chamber by another Teflon lens into the cryo-cooled THz hot-electron bolometer. Lastly, a

lock-in amplifier increases the signal-to-noise ratio. The emitted signal is frequency modulated at 0.2 kHz, and the received signal has a resolution of 0.10 MHz. The system has a limit of detection of a S/N of 3; this S/N is determined for the lowest of 5 rotational transitions for each species

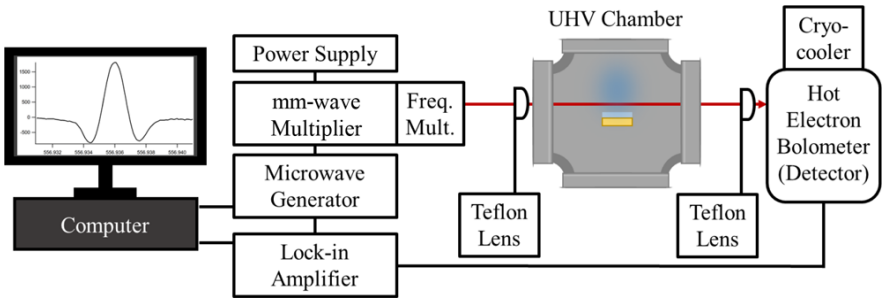

Figure 1.1.11: Diagram of the Terahertz detection system

Table 1.1.2 shows the results for the SNR for 3 species H_2O, D_2O, CH_3OH. For each species, the pressure was increased in increments of 1×10^{-8}Torr. Once a SNR of 3 is reached, the pressure is recorded and converted to density

analyte	LOD(molecules cm^{-3})	Frequency (MHz)	number of scans averaged	SNR
H_2O	1.1×10^9	556935.99	30	5.6
D_2O	1.7×10^9	607349.44	30	3.8
CH_3OH	3.1×10^{10}	627170.48	30	8.3

Table 1.1.2: Limit of Detection studies for H_2O, D_2O, CH_3OH

Measurements for the thermal desorption rate R_{des} for H_2O were done by studying the relation between the spectra peak intensity $I(T)$, the desorption rate, and the loss of ice molecules over time. The linear proportionality of these values was calibrated using the RGA system to account for extra variables such as the effective pumping speed of the system and the recondensation of gas-phase species onto the cryostat. This calibration yield a linear proportionality for peak intensity of H_2O to desorption rate of

$$I(T) = 3.04 \times 10^{-9}(R_{des}) - 4.37 \tag{1.1.37}$$

High-Resolution Gas Phase Spectroscopy of Molecules Desorbed from an Ice Surface: A Proof-of-Principle Study Theulé et al. (2019)

This experiment is designed to study gas-phase complex organic molecules. The experiment consists of a high vacuum chamber 1×10^{-6}mbar with a cryostat system. Connected to the cryostat, a U-shaped Ku band $(11 - 20GHz)$ waveguide, a sketch of the experiment is shown in Fig. 1.1.12. A teflon gas line is connected to the waveguide for gas deposition. The waveguide is connected to a chirped-pulse Fourier transform spectrometer (CP-FTMW) for species analysis.

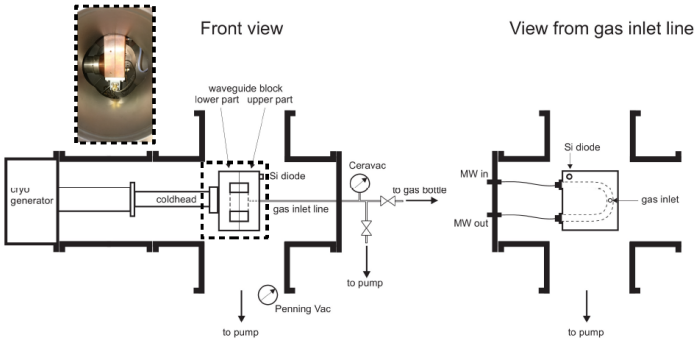

Figure 1.1.12: Experimental setup of the main chamber. The U-shaped wave guide is connected to the coldhead to maximise cooling. The gas is injected directly into the waveguide.

Ice samples are deposited in the waveguide's inner walls, and desorbed molecules are detected with a chirped pulsed Fourier transform within a frequency range of $2 - 50$GHz. The microwave chirped pulse is broadcast into the waveguide; the gas-phase molecules whose transitions fall into the chosen frequency range will be polarised by the pulse; they will then undergo broadband free induction decay (FID). This signal is received by an antenna, it is then amplified, down-converted and digitalized. The system employs phase-synchronised repetition to allow for correct averaging of the signal. The digitalized averaged signal is then fast Fourier transformed into the frequency domain for analysis. Typical parameters for the experiment were 700-nanosecond chirped pulses, with a 1GHz frequency span. 1000 scans were averaged; this process takes $\sim$ 2s

The experiment was benchmarked by measuring the inversion spectrum of desorbing ammonia ice in a TPD experiment. Ammonia gas with purity 5.5 was injected directly into the waveguide through a 1mm diameter inlet hole. The amount of molecules injected was determined by the injection time and the dosing pressure, with the assumptions that the sticking coefficient is 1 at cryogenic temperatures and that the surface coverage is uniform along the inner surface. The

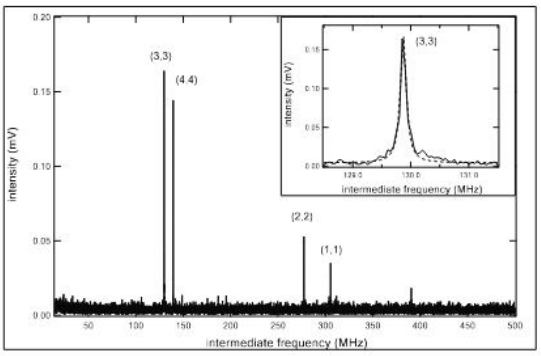

Figure 1.1.13: The inversion spectrum of NH_3 between $23500 - 24500\,\mathrm{MHz}$. The spectrum corresponds to the desorption at 110K of 1.4 monolayers of NH_3. The J and K (1,1),(2,2),(3,3) and (4,4) inversion transitions are shown, with the fitting of the (3,3) transition with a Lorentzian function shown in the subplot.

thickness was also calibrated by integrating the line intensities during desorption. The TPD experiment was done with a ramp rate of $.4\,\mathrm{K\,min^{-1}}$ with an initial temperature of $20\,\mathrm{K}$. The CP-FTMW measured the four inversion transitions of ammonia between 23500 and 24500 MHz. Fig. 1.1.13 shows the inversion spectrum of NH_3 as recorded by the CP-FTMW.

TPD curves were obtained for the (3,3) transition signal and are shown in Fig. 1.1.14. The desorption peak was expected at a value of 95 but was found at a temperature of 105 K. This shift of the temperature peak is attributed to a low gas flow rate from the waveguide to the main chamber, this rate was measured at $5 \times 10^3\,L/s$, it could also be caused by water contamination in the NH_3 ice. Fitting the TPD data with a zero-order (for multi-layer) Polanyi-Wigner equation yields a binding energy for ammonia of $E_{des} = 31.6 \pm 0.1\,kJmol^{-1}$. This value is in reasonable agreement with the standard value from Fourier transform infrared spectroscopy of $25.6\,\mathrm{kJmol^{-1}}$

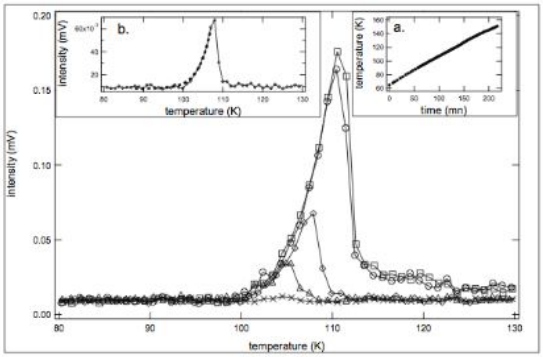

Figure 1.1.14: TPD curves for NH_3. Open squares correspond to 1.5ML, open circles to 1.4ML, open diamonds to 0.8ML, open triangles to 0.4ML and crosses to 0.1ML ice thickness. signal was measured for the (3,3) transition, the temperature ramp for the TPD experiment was $0.4\,K/min$

The sensitivity of the experiment was studied by setting a pressure inside both the chamber and the waveguide by removing the teflon gas inlet from the waveguide to equalise the pressure in both the chamber and the waveguide. Pressure was lowered until line intensity for the (3,3) transition reached the limit of 3σ. This value corresponds to 3×10^{12} molecules in $19.1\,\mathrm{cm}^3$ of the waveguide, this is about 5 picomoles.

1.2 Objectives

Now that we have established the scientific background for this PhD thesis, we can define its main objective:

- Design and develop an experiment to study surface interactions of astronomically relevant species on the surface of dust nanoparticles.

To achieve this goal, we must then define smaller objectives that we must reach:

- Implement an injection system to inject nanoparticles into vacuum.
- Trap a single nanoparticle in an ion trap.
- Measure the nanoparticles' secular frequencies
- Manipulate the charge of the trapped nanoparticles.
- Calculate the mass of the trapped nanoparticles
- Adsorb species onto the surface of trapped nanoparticles

It is clear from the objectives that a critical requirement for the CODE experiment is a fundamental understanding of the workings of ion manipulation systems, which will be discussed in the following section.

Chapter 2

Theoretical Framework

2.1 Ion Manipulation System

2.1.1 Theory of Quadrupolar devices

The following discussion on quadrupolar devices is a summary of the study done in March and Todd (2005).

The theory presented here is an ideal case based on the behaviour of a single ion (charge q=e) in an infinite ideal quadrupole field in the total absence of any background gas.

A quadrupolar device described with reference to rectangular coordinates, the potential $\phi_{x,y,z}$ at any given point within the device can be expressed in its most general form as

$$\phi_{x,y,z} = A(\lambda x^2 + \sigma y^2 + \gamma z^2) + C \tag{2.1.1}$$

where A is a term independent of x, y, and z that includes the electric potential applied between the electrodes of opposing polarity (an RF potential alone or in combination with a DC potential), C is a "fixed" potential (which also may be an RF potential either alone or in combination with a DC potential), and λ, σ, and γ are weighting constants for the x, y, and z coordinates, respectively. It can

be seen from Eq. 2.1.1 that in each coordinate direction the potential increases quadratically with x, y, and z, respectively, and that there are no "cross terms" of the type xy, and so on. This property of Eq. 2.1.1 has important implications for the treatment of the motion of ions within the field, in that we can consider the components of motion in the x, y, and z directions to be independent of each other.

In an electric field, it is essential that the Laplace condition

$$\nabla^2 \phi_{x,y,z} = 0 \tag{2.1.2}$$

substituting 2.1.1 in 2.1.2 yields

$$\nabla^2 \phi_{x,y,z} = A(2\lambda + 2\gamma + 2\sigma) = 0 \tag{2.1.3}$$

We will work with the $A \neq 0$ solution, thus

$$\lambda + \gamma + \sigma = 0 \tag{2.1.4}$$

We will now work with two sets of solutions, one for analysing the two-dimensional Quadrupole Mass Filter (QMF) and the other to study the Quadrupole Ion Trap (QIT).

For the QMF, we have

$$\lambda = -\sigma = 1 \qquad \gamma = 0 \tag{2.1.5}$$

and for the QIT

$$\lambda = \sigma = 1 \qquad \gamma = -2 \tag{2.1.6}$$

Using the values from 2.1.5 we now have a potential for a QMF

$$\phi_{x,y} = A(x^2 - y^2) + C \tag{2.1.7}$$

This quadrupolar potential corresponds to a configuration of two pairs of electrodes with hyperbolic cross sections defined by:

$$\frac{x^2}{x_0^2} - \frac{y^2}{a^2} = \quad 1 \tag{2.1.8}$$

$$\frac{x^2}{b^2} - \frac{y^2}{y_0^2} = \quad -1 \tag{2.1.9}$$

For the x and y pair of electrodes, respectively. In order to establish a quadrupolar potential, it is a condition that the hyperbola share common asymptotes, even though it is not a requirement that $x_0 = y_0$. In practice, though, all mass filters produced are constructed symmetrically according to the condition

$$x_0 = y_0 = r_0 \tag{2.1.10}$$

Here, r_0 is the radius of the inscribed circle tangential to the inner surface of the electrodes. We can now redefine the equations for the electrode surfaces as

$$x^2 - y^2 = r_0^2 \tag{2.1.11}$$

$$x^2 - y^2 = -r_0^2 \tag{2.1.12}$$

For the x and y pair, respectively.

Most modern QMF systems are composed of arrays of round rods. When such rods are used for a QMF, a good approximation of a quadrupolar field can be obtained by using a value r for their radius in the range of $r = 1.12 \times r_0$ to $r = 1.13 \times r_0$.

We will continue the study of QMF, considering a QMF made of two pairs of circular rods as shown in Fig. 2.1.1

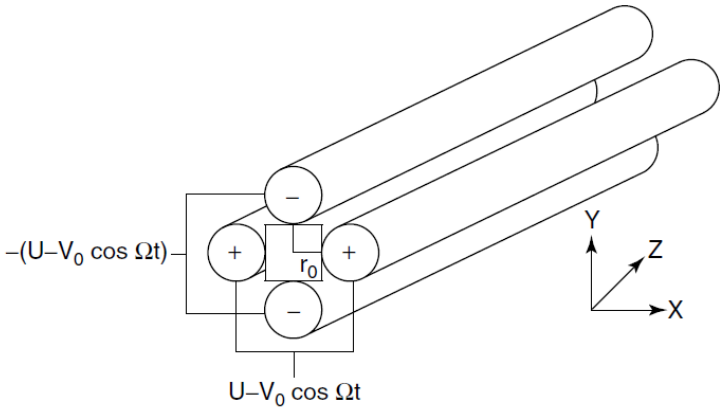

Figure 2.1.1: Quadrupole mass filter. The ions enter and travel in the z direction, while oscillating in the x–y plane. The oscillation is controlled by the DC (U) and RF (V) potentials applied to each pair of rods. Only those ions with stable trajectories at the selected U and V values will travel the length of the QMF and be detected.

The ions enter the QMF and travel in the z direction. While travelling in the z direction, the ions also oscillate in the x–y plane, due to the potentials applied to the rods. This oscillation is a property of the mass/charge ratio of a given ion species. Therefore, ions of a specific mass/charge ratio will all react equally to the electric potentials imposed by the quadrupole assembly. Under appropriate electrical conditions, ions of a single mass/charge ratio will have a stable trajectory for the entire length of the quadrupole. A QMF can be operated to transmit either all ions or only a specific range of mass/charge ratios and to focus them at the exit aperture.

The quadrupolar potential to which the ions are subjected, ϕ_0 is given by the difference between the potentials applied to the x and y pair of electrodes

$$\phi_0 = \phi_x - \phi_y \tag{2.1.13}$$

since the potential must be the same across the whole of the electrode surface, we can write that when $y = 0$, $x_0^2 = r_0^2$

$$\begin{aligned} \phi_x &= A(r_0^2) + C && (2.1.14)\\ \phi_y &= A(-r_0^2) + C && (2.1.15)\\ A &= \frac{\phi_0}{2r_0^2} && (2.1.16)\\ & && (2.1.17) \end{aligned}$$

applying the resulting potentials to Eq 2.1.13 it is simple to deduce that

$$\phi_{x,y} = \frac{\phi_0}{2r_0^2}(x^2 - y^2) + C \tag{2.1.18}$$

This expression is generally used with C=0 (the electrode structure is floated at ground potential).
We can now proceed to examine the motion of an ion when subjected to this potential.

The force acting of an ion along the x axis $(x, 0)$ F_x is given by

$$F_x = -e\frac{d\phi}{dx} = m\frac{d^2x}{dt^2} = -e\frac{\phi_0 x}{r_0^2} \tag{2.1.19}$$

Let us now consider a real system in which

$$\phi_0 = 2(U + Vcos(\Omega t)) \tag{2.1.20}$$

where V is the zero-to-peak amplitude of an RF potential oscillating with angular frequency Ω (expressed in radians per second) and $\pm U$ is a DC voltage applied

to the x and y pairs of electrodes, respectively. If we apply this potential to Eq. 2.1.19, we obtain

$$\frac{d^2x}{dt^2} = -\left(\frac{2eU}{mr_0^2} + \frac{2eVcos(\Omega t)}{mr_0^2}\right)x \tag{2.1.21}$$

We can solve this equation as a Mathew Equation of the form

$$\frac{d^2u}{d\xi^2} + (a_u - 2q_ucos(2\xi))u = 0 \tag{2.1.22}$$

with $\xi = \Omega t/2$, we find then the values for a_x and q_x are

$$a_x = \frac{8eU}{mr_0^2\Omega^2} \tag{2.1.23}$$

$$q_x = \frac{-4eV}{mr_0^2\Omega^2} \tag{2.1.24}$$

When this derivation is repeated to obtain the force on an ion in the y direction in a QMF, one finds that $ax = -ay$ and $qx = -qy$. These values a_x, q_x are particularly interesting because they are functions of the instrumental parameters that govern the functioning of the QMF.

The solutions to the Mathieu equation are now accessible to us and can be interpreted in terms of ion trajectory stability (and instability) in each of the x and y directions, of confinement within the totality of the quadrupole field (when conditions correspond simultaneously to ion trajectory stability in each of the x and y directions), and of the characteristic fundamental secular frequencies of ion motion in the x and y directions. Because the fields in the QMF are uncoupled, one needs to examine the solutions to the Mathieu equation in one dimension only. Figure 2.1.2 shows us the stability diagrams for the x and y axis superlapped the stability regions showed are delimited by characteristic numbers of a cosine type function (a_m) of order m and a sine-type function (b_m) of order m (in figure

2.1.2 m values are 0 and 1 for a and 1 and 2 for b). Figure 2.1.3 is a close up of region A. Region A is symmetric along the q_u axis; thus, if an ion's a_x, q_x lie within region A its a_y, q_y must necessarily lie also within stability region A.

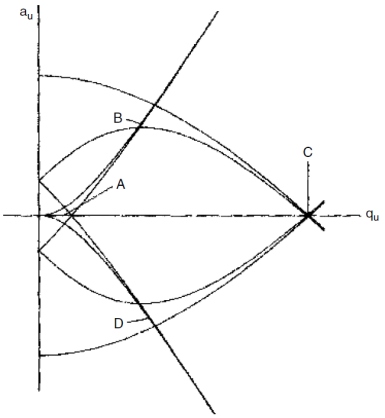

Figure 2.1.2: Superposition of two Mathieu stability diagrams (x and y). Regions of simultaneous overlap are labelled

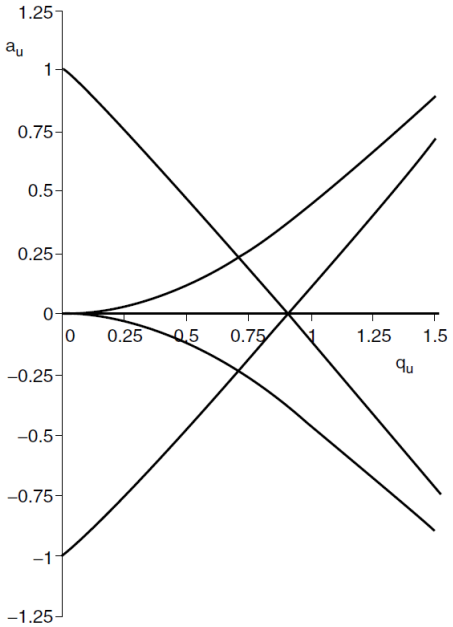

Figure 2.1.3: Boundaries of stability region A in a_u and q_u for QMF. The boundaries represent the limits in a_u and q_u for stable ion trajectories and satisfy the Mathieu equation. The stability diagram is symmetric about the q_u axis.

2.1.1.1 Quadrupole Ion trap

Following the same work we did with the QMF configuration of the λ, σ, γ parameters, we shall define our potential $\phi_{x,y,z}$ for a QIT comprised of three electrodes, two hyperbolic "end cap" electrodes and a central ring electrode, as shown in fig 2.1.4

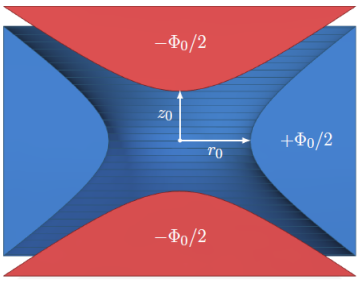

Figure 2.1.4: a quadrople ion trap cut in half along the axis of cylindrical symmetry

We then have a potential of the form

$$\phi_{x,y,z} = A(x^2 + y^2 - 2z^2) + C \tag{2.1.25}$$

Converting to cylindrical coordinates, we have

$$\phi_{r,z} = A(r^2 - 2z^2) + C \tag{2.1.26}$$

We can now write the equations for the electrode surfaces as

$$\frac{r^2}{r_0^2} - \frac{z^2}{a^2} = 1 \tag{2.1.27}$$

$$\frac{r^2}{b^2} - \frac{z^2}{z_0^2} = -1 \tag{2.1.28}$$

for the ring and end cap electrodes, respectively. As in the previous treatment of the mass filter, we note that in order to establish a quadrupolar field, the ring

and the end-cap electrodes must share common asymptotes, so that $m = m'$, thus $a^2b^2 = r_0^2 z_0^2$. We can reorganise our equations using these values to obtain the following equations for the electrodes

$$\frac{r^2}{r_0^2} - \frac{2z^2}{r_0^2} = 1 \tag{2.1.29}$$

$$\frac{r^2}{2z_0^2} - \frac{z^2}{z_0^2} = -1 \tag{2.1.30}$$

for the ring and end cap electrodes, respectively. If we now proceed as with the QMF to evaluate the constants A and C in the general expression for the potential, we find without much effort that

$$A = \frac{\phi_0}{r_0^2+2z_0^2} \tag{2.1.31}$$

$$\phi_r, z = \frac{\phi(r^2-2z^2}{r_0^2+2z_0^2} + C \tag{2.1.32}$$

For the case of QIT systems, not all QITs work with an opposite potential for the r and z electrodes.The QIT system can be used with the end cap electrodes held at ground potential, thus

$$\phi_{0,z} = \frac{\phi_0(0-2z_0^2}{r_0^2+2z_0^2} + C = 0 \tag{2.1.33}$$

$$C = \frac{2\phi_0 z_0^2}{r_0^2+2z_0^2} \tag{2.1.34}$$

However, for the following calculation of the a_u, q_u parameters of the QIT, we will not consider this particular case.

We now use again consider a real system in which

$$\phi_0 = (U + Vcos\Omega t) \tag{2.1.35}$$

and examine the force acting on an ion along the z axis

$$F_z = -e\frac{d\phi}{dz} = m\frac{d^2z}{dt^2} = e\frac{4\phi_0 z}{r_0^2 + 2z_0^2} \tag{2.1.36}$$

which may be expanded to give

$$\frac{d^2z}{dt^2} = \left(\frac{4eU}{m(r_0^2 + 2z_0^2)} + \frac{4eVcos\Omega t}{m(r_0^2 + 2z_0^2)}\right) z \tag{2.1.37}$$

As with the QMF, we solve this equation as a Mathieu equation to obtain the relationships

$$a_z = -\frac{16eU}{m(r_0^2 + 2z_0^2)\Omega^2} \tag{2.1.38}$$

$$q_z = \frac{8eV}{m(r_0^2 + 2z_0^2)\Omega^2} \tag{2.1.39}$$

doing this process for r one finds that

$$a_z = -2a_r \qquad q_z = -2q_r \tag{2.1.40}$$

So far in this formulation of the motion occurring within the ion trap we have made no assumption concerning the relationship between the dimensions r_0 and z_0. Historically, we see that ever since the early descriptions of the ion tra,p the relationship

$$r_0^2 = 2z_0^2 \tag{2.1.41}$$

has been selected as a requirement for forming the ideal quadrupolar potential distribution.

As with the QMF the QIT operation is concerned with the criteria that govern the stability of the trajectory of an ion within the electrical field.Ions can be stored in the ion trap provided that their trajectories are stable in the r and z directions simultaneously; such trajectory stability is obtained in the region closest to the origin. Figure 2.1.5 is a close up of the stability region of greatest importance for an ideal QIT.

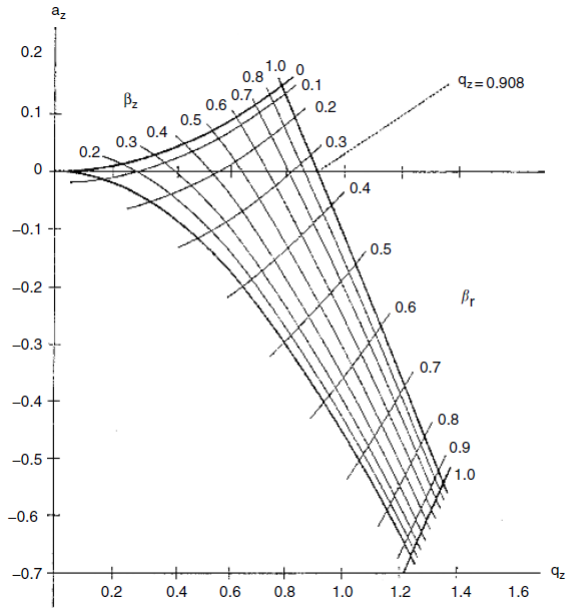

Figure 2.1.5: Stability diagram in (a_z, q_z) space for region of simultaneous stability A in both r and z directions near origin for three-dimensional QIT, the iso-β_r and iso-β_z lines are shown.

Since the purpose of a QIT is trapping ions, their motion inside the trap is of interest. Ion trajectory inside the trap is composed of two fundamental frequency components, $\omega_{r,0}$ and $\omega_{z,0}$. The description "fundamental" implies that there exist other higher order (n) frequencies and the entire family of frequencies is thus described by $\omega_{r,n}$ and $\omega_{z,n}$. These secular frequencies are given by

$$\omega_{u,n} = (n + 0.5\beta_u)\Omega \qquad 0 \leq n < \infty \tag{2.1.42}$$

$$\omega_{u,n} = -(n + 0.5\beta_u)\Omega \qquad -\infty < n < 0 \tag{2.1.43}$$

where

$$\beta_u = \sqrt{(a_u + 0.5q_u^2)} \tag{2.1.44}$$

Chapter 3

The CODE experiment

The CODE experiment is subdivided into multiple subsystems that work in unison. The following section details the work done in our facilities during the development of the PhD thesis for each subsystem, highlighting the challenges we overcame.

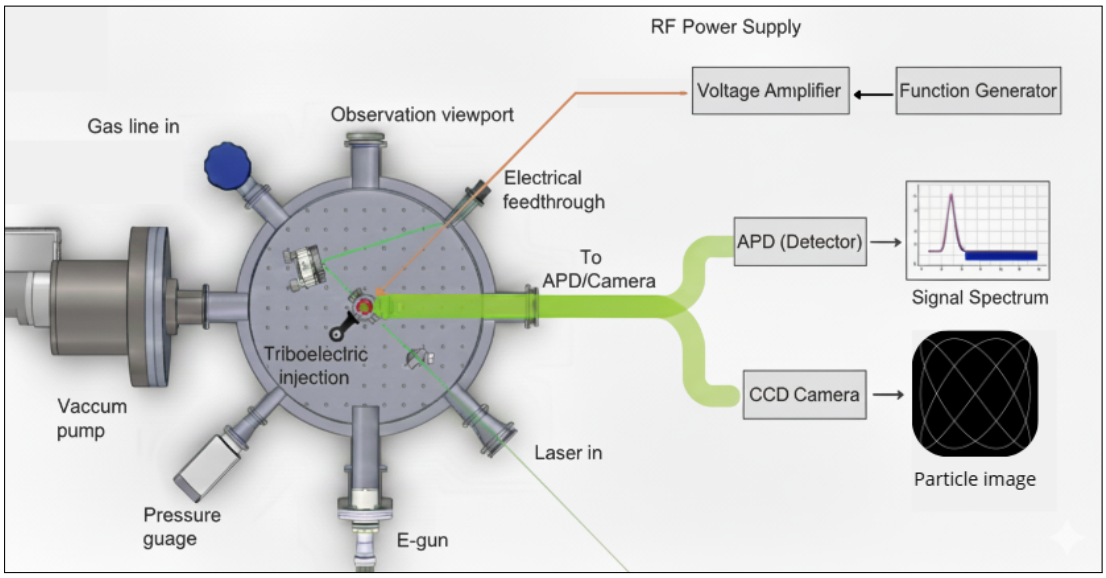

Figure 3.0.1: General sketch of the CODE experiment with its components listed, the image summarises the workings of the system to be detailed in the following section

3.1 The vacuum chamber

The CODE experiment requires ultra high vacuum (UHV) ($< 5 \times 10^{-6}\, mbar$) to properly function, as this is the minimum working pressure for the electron

gun; however, it is not strictly necessary to reach the low ends of the UHV. These vacuum levels are achieved using an Agilent Twistorr 305Fs turbo-molecular vacuum pump coupled with an Agilent IDP-15.

As the CODE development was a new branch of experimental work within the Universidad de Concepcion, it was designed with O-ring seals to allow for quick and easy manipulation of connections and minimise leakage by mishandling of conflat (CF) connections.

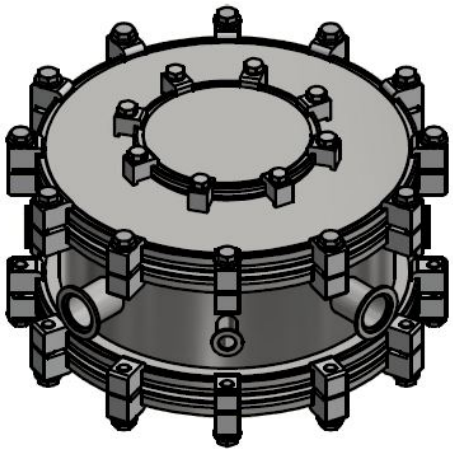

Figure 3.1.1: Isometric rendering of the CODE main chamber

The Main chamber of the CODE experiment, shown in Fig. 3.1.1, is where the ion-trap is housed inside the CODE experiment. The main chamber has 4 KF40 parts and 2 KF25 and KF16 ports. The placement of the ports is shown in fig 3.1.2. The main chamber is separated into 3 different parts: The Top and bottom lids, LF320 connections, and the main cylinder. The top lid also has a connection for an LF-160 connection where the cold head is to be placed, the bottom lid has a screw bed for M6 screws with a distance of 2.5cm to other screws shown in fig 3.1.3 the bed has 109 screw positions with the (0,0) screw in the centre of the lid to allow for easy alignment of the trap and all other components (electron gun, optical system UV lamp). The chamber was a custom design by the author of this thesis, and it was fabricated by the ANCORP company in the USA. The chamber is certified for 10^{-8}torr with a measured leak of 10^{-9}std cc/sec. The chamber is mounted on an aluminium frame shown in fig 3.1.6 and is kept in place by 4 M6 screws connected to the frame. The bottom lid has an alternative design, shown in 3.1.3 with an adaptor for the turbo pump so that it can be fitted from below

and free up one of the KF40 ports used for vacuuming. For this update to be used, we must first connect the cold head and mount the trap onto the cold head, since we have no place to connect to in the centre of the new bottom lid.

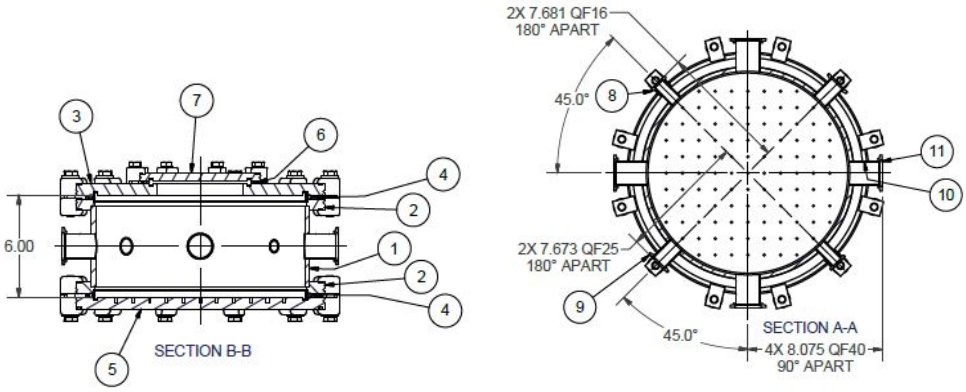

Figure 3.1.2: Sketch of the Main chamber. Listed are the different components in ascending order: 1 The main cylinder, 2 The welded connectors from the Main cylinder to the LF320 connection, 3 the top lid, 4 the viton orings, 5 the bottom lid, 6 the LF160 oring, 7 the LF 160 blank, 8 the KF16 ports, 9 the KF25 ports, 10 and 11 the KF 40 ports.

Of the 8 ports of the Main chamber shown in fig 3.1.2 (not considering the top and bottom lid as ports), the KF 16 ports are used for the electrical feedthrough and the pressure gauge, the KF 25 ports are used for the optical system and the gas line all metal leak valve, and the KF40 ports are used for the optical system, the electron gun, the UV lamp and the Electro Spray Ionization (ESI) system or the pumping system depending on if the new bottom lid is used.

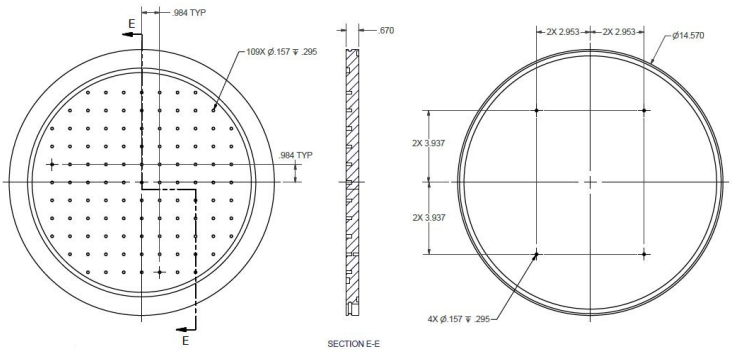

Figure 3.1.3: Bottom lid of the CODE experiment. All units are in inches; both the screw bed on the inside of the lid and the 4 connection screws for the aluminium frame are shown.

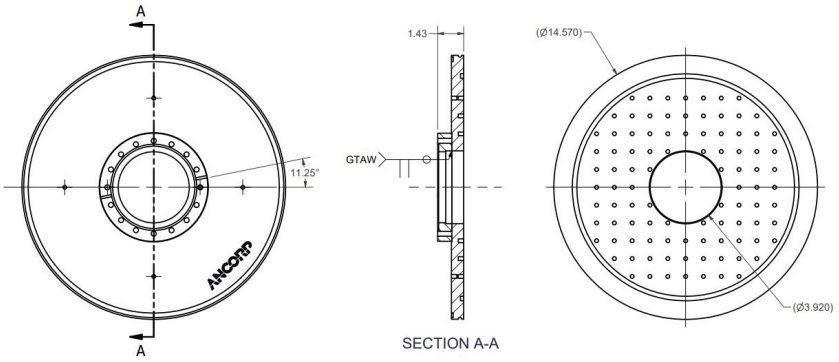

Figure 3.1.4: Modified bottom lid of the CODE experiment

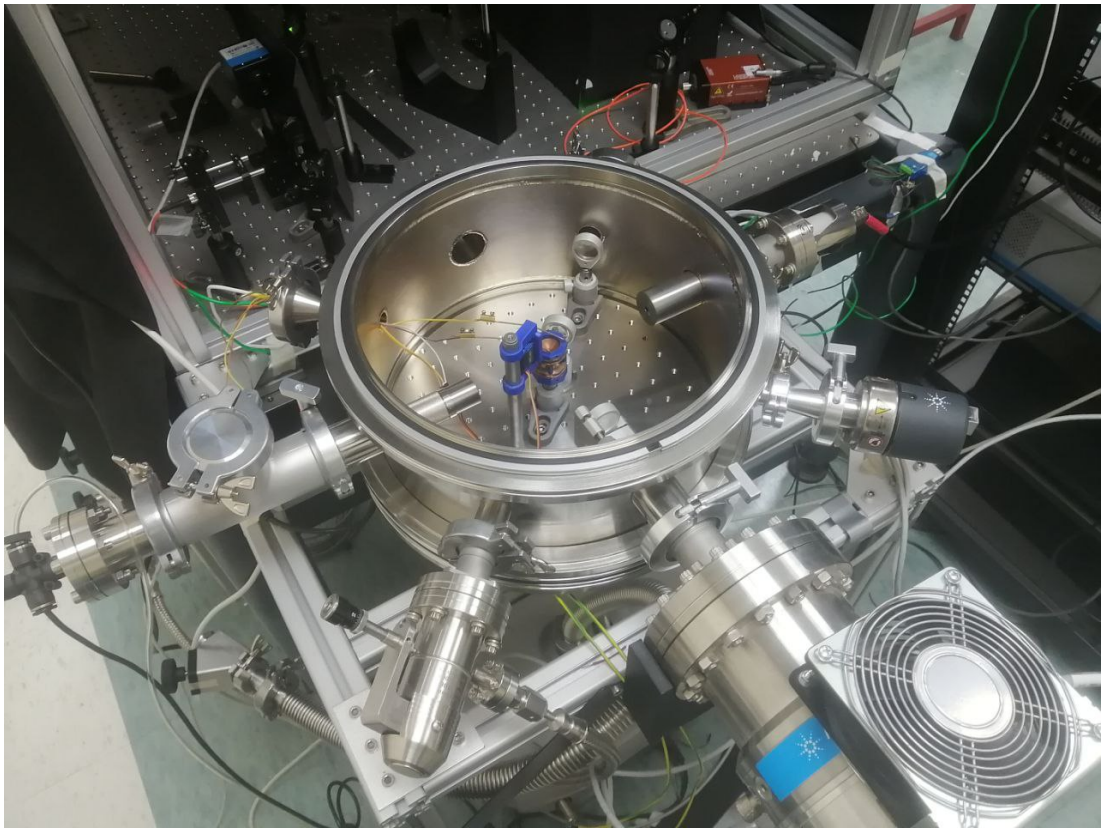

Figure 3.1.5: The CODE vacuum chamber without the top lid. Inside, we can see the Electron gun, the UV lamp, the Ion trap, the triboelectric injection, and the pumping system.

3.1.1 Mechanical support

The experiment supported on an $900 \times 1200mm$ optical table (Thorlabs SDH90120 frame and B90120AX breadboard) which has passive vibration isolation, the aluminium frame that holds the vacuum chamber is partly mounted on the optical

table to ensure that any vibrations in the system do not affect the optical system, (see fig 3.1.6), the 3 remaining legs are mounted on standard duty Thorlabs PWA074 dampeners to reduce vibrations, the optical table has an aluminium frame fitted with aluminium panels painted matte black to reduce unwanted light in the experiment (see fig 3.1.7), the panels cover the top and 2 exterior sides of the experiment. The remaining sides are covered with black curtains to allow for easy handling of optical components and to quickly reach the stepper mirror to switch from camera to APD modes.

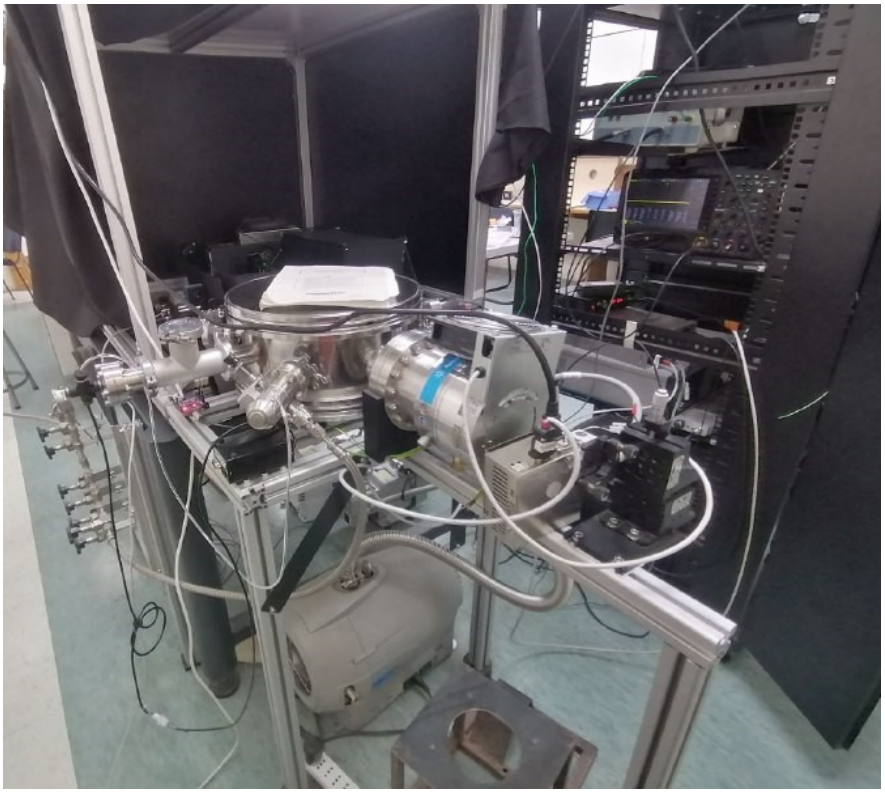

Figure 3.1.6: Picture of the CODE experiment (May 2025) showing the aluminium frame on which it is mounted, as we can see the frame is in part mounted directly onto the optical table, heavier elements such as the turbo pump are supported directly onto the frame to reduce stress on the vacuum chamber.

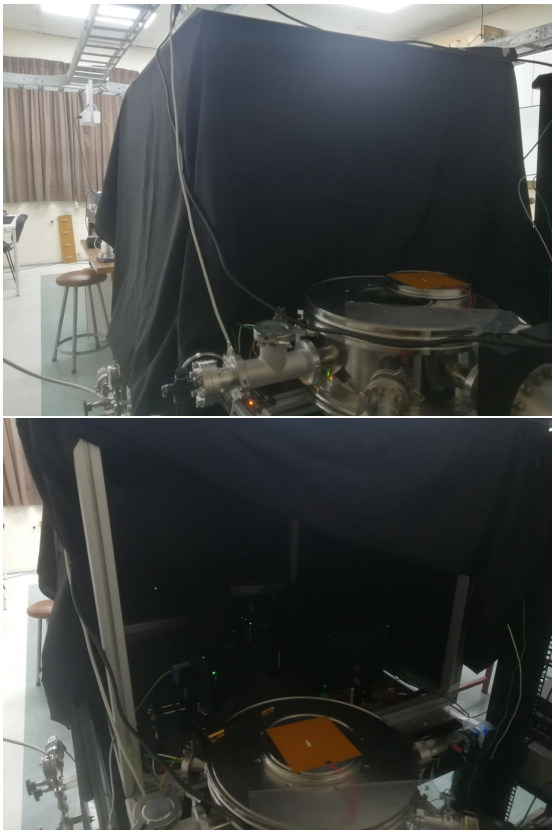

Figure 3.1.7: The code experiment as seen with its enclosure, since the chamber itself is closed, only the viewports are covered with the enclosure to ensure only the light from the optical system reaches the APD/camera system.

3.1.2 The Gas line

The CODE experiment features a Swagelok custom-made gas line for gas mixture preparation, see fig3.1.8. It features 5 entrance ports for different gases, each with its own unique valve. The system has two different pressure gauges, an Agilent CDG500 capacitance diaphragm valve $1.3 - 1333\,mbar$. This type of gauge allows absolute measurement of gas pressure, allowing us to make accurate mixtures of gases at low pressures, if we wish to make high-pressure mixtures for high amounts of dosage, the system has a Swagelok absolute pressure gauge for $-1 - 6.5\,bar$. Currently, the CODE Gas line is connected to an Argon reservoir used for particle deceleration and pressure control of the CODE experiment. The gas line is connected to an Agilent variable leak valve model ($10^{-10}\,Torr - L/sec$) fig 3.1.9 for precise flow control into the system.

Figure 3.1.8: The CODE gas line system, we can see 4 gas lines for additional connections in the bottom and to the left is the argon line, the connection on the right goes to the vacuum chamber.

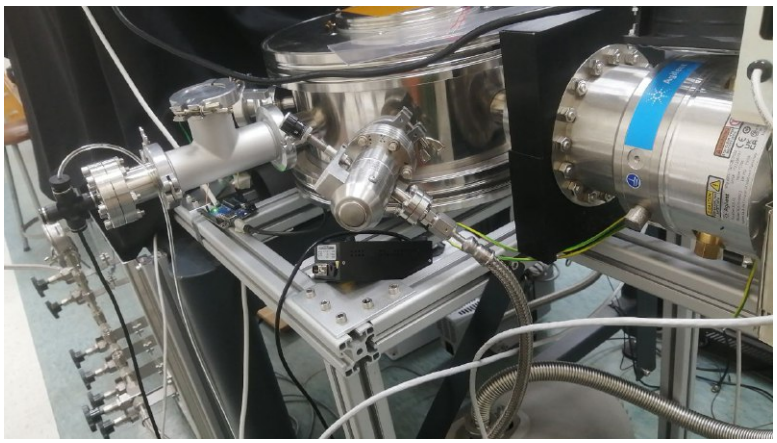

Figure 3.1.9: The leak valve used in the CODE experiment. Since the vacuum chamber has only one large space inside, we can assume that the distribution of gas inside the chamber is homogeneous.

3.2 The Ion trap

The central part of the experiment is the ion trap. Thus, the design of this system is critical for the correct functioning of the CODE experiment; however, when we wish to apply QIT systems in experimental physics, we find that the geometry of the ideal QIT presents practical issues. First and foremost is the issue of line

of sight; there is little room for any system to interact with the trapped particle, and the injection of the particles becomes a great issue. To solve both of these issues, we could change the geometry of the ion trap. Solutions like an octopole ion trap have been used Schlemmer et al. (2004); however, using a non-continuous electrode like in an octopole trap can affect the shape of the electric potential. The shape of the potential is crucial for our approximations, as the equations used to calculate the mass-to-charge ratio of the nanoparticles act under the assumption that we are working close to the ideal potential of the Paul trap design. To solve these geometrical issues, alternative geometries can be used; the only condition that they must fulfil is that the potential generated must be equal or nearly equal to the ideal QIT. This will allow us to use the unmodified versions of the QIT equations. For the CODE experiment, we require ample line of sight into the

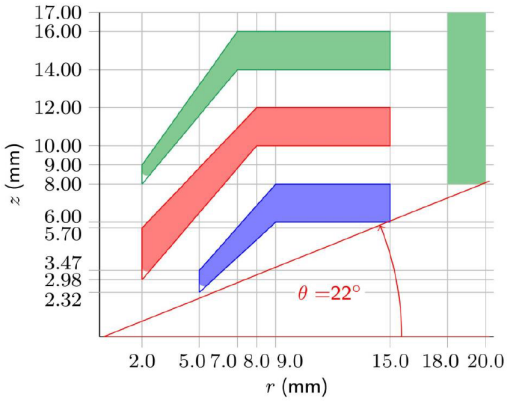

Figure 3.2.1: Exact dimensions of the cryogenic split ring electrode trap. The solid lines define the electrode geometry. The green regions define a collimation electrode not included in CODE at the moment Esser et al. (2019).

centre of the trap. We found that the Split Ring Electro Trap designed by Esser et al. (2019). This design, shown in figure 3.2.1, was designed and optimised using the ion flight simulation program SIMION. The potential of the system differs by 0.1% to the ideal QIT potential, allowing us to use the equations listed in 2.1.1.1.

The trap is placed in the centre of the vacuum chamber, either mounted from the bottom (when the cryogenic system is not connected) or from the top, connected to the cold head to perform cryogenic experiments. Fig. 3.2.2 shows the ion trap with its surface and cryogenic mount, respectively. The trap uses only a few mWatts of power as it uses minimal current, ensuring that the heat load from the trap's power is minimal. The spacers and support for the trap system were initially made with 3D printers in PLA plastic, as it is readily available in the lab

and allows for quick iterations between different versions. The final version of the support structure has been fabricated from PEEK plastic. This material has low outgassing rate and is a good electrical insulator and with a low linear expansion coefficient of $\sim 57.1 \times 10^{-6}\mathrm{K}^{-1}$.

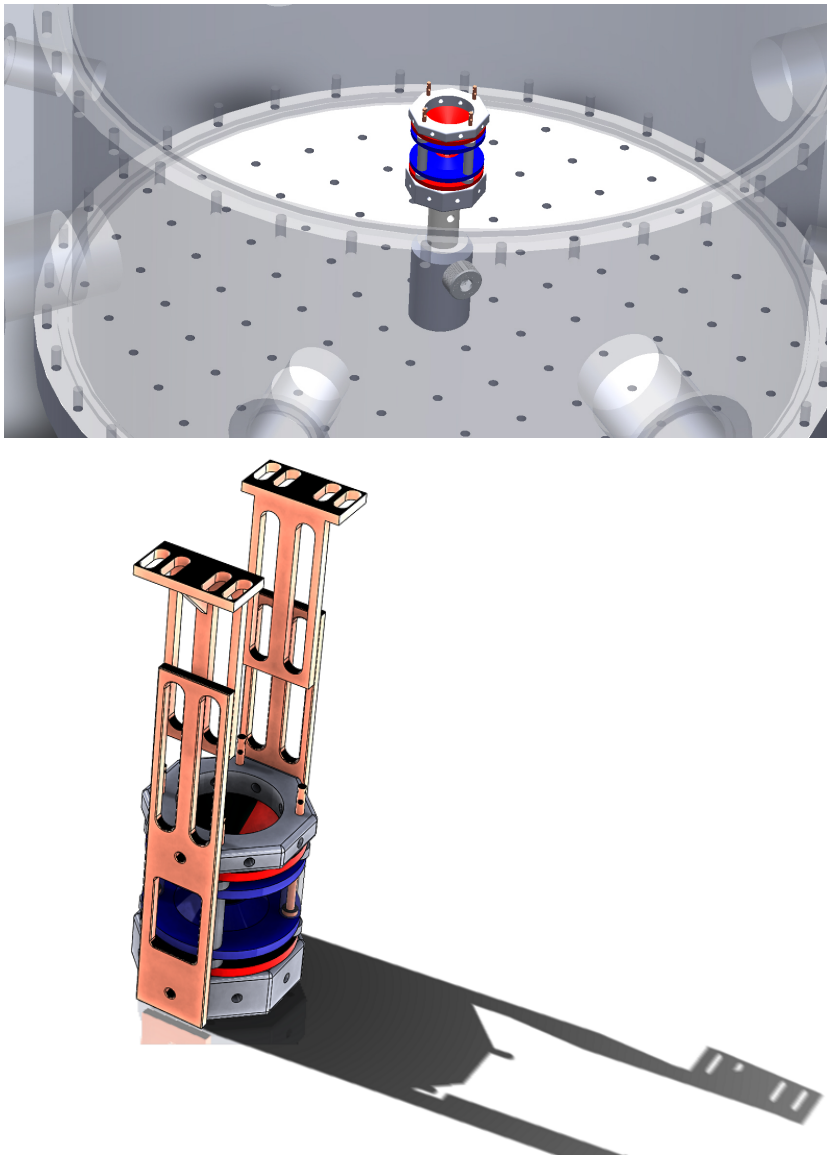

Figure 3.2.2: Top: Rendering of the ion trap in its position held from the bottom with vacuum-compatible optical posts. Bottom: Cryogenic mount for the ion trap.

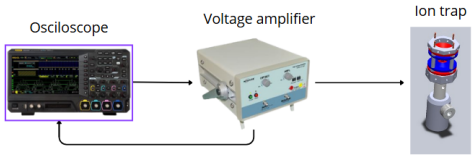

Figure 3.2.3: Sketch of the power supply system for the ion trap

3.2.1 Ion trap power supply

3.2.1.1 HA 1600 voltage amplifier

The setup consists of a signal generator, a Rigol MS0574 Oscilloscope. This device has two LO ports capable of generating various types of signals (sine wave, ramp, square wave, etc). The output voltage can be set up to 5Vpp. The oscilloscope output is connected to a HA-1600 voltage amplifier, which can amplify the input signal by $\times 200$ with a maximum voltage of 1600 Vpp. The amplifier can correctly amplify signals without loss of power up to 200kHz. With this system, we can now set any voltage from $0 - 1000$ Vpp and any frequency from $DC - 200$ kHz. We can also set different types of waveforms. The signal output is monitored using the same Rigol MS0574 Oscilloscope using the $1/200$ signal output channel from the HA-1600 power amplifier. Fig. 3.2.3 shows a sketch of the trap voltage setup.

This setup allowed for ample control of the trapping system; however, due to the low voltage of the oscilloscope, we can only use a limited range of frequencies without lowering the q_u stability parameter. To solve this issue and allow greater control of the trapping potential we decided to use a signal generator instead of the oscilloscope to generate the frequency, this new device allows for voltages up to 10 V and 1 MHz signal output, allowing us to exploit the full extent of the HA voltage and frequency range. In addition, we used the LO from the Oscilloscope to add a second, much smaller (a few centivolt) frequency, to use as a resonant tone analyser. This analysis system allows us to ensure that the frequencies that are being measured by the data acquisition system are the secular frequencies of the particle. Fig. 3.2.4 shows a sketch of the new system. The system also serves as a particle rejection system, as exiting the resonant frequencies of unwanted trapped particles after injection is a very efficient and controlled way of doing particle rejection.

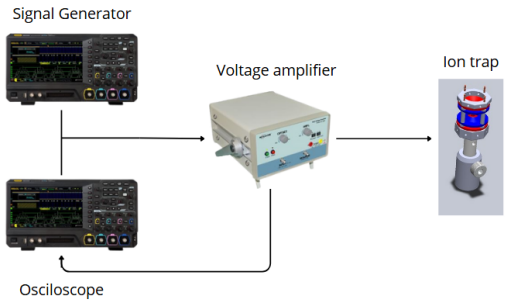

Figure 3.2.4: Sketch of the power supply system with the second LO to allow for resonant frequency analysis

3.3 Optical system

TPD experiments on a single nanoparticle, such as the experiments to be carried out on the CODE system, will not emit sufficient molecules for mass spectrometers to detect, so we must then detect desorption of ices on the surface of the NP with a different method than what is generally used in TPD experiments. As explained in section 2.1.1.1, particles inside the ion trap oscillate at frequencies associated with their mass-to-charge ratio and with the voltage and frequency of the ion trap. We can use this frequency value to determine the mass of a trapped nanoparticle, but we must have a system capable of measuring the frequency of the trapped nanoparticle. In order to measure the secular frequencies of trapped nanoparticles, we employ an optical system to illuminate the nanoparticles and measure the light scattered by the NP. The system can be divided into two subsystems: illumination and detection. The whole system is listed in fig 3.3.1 and a photograph of the system is shown in fig 3.3.2.

3.3.1 Illumination

To measure the frequency, we illuminate the particle in such a way that the intensity of the scattered light varies with the phase (or position) of the particle. This measurement will be more precise if the variation of intensity is higher with each cycle. To ensure this, we must have a beam diameter small enough so that the variation with its Gaussian distribution for the amplitude of the oscillations of the trapped nanoparticles (< 0.2mm) is high enough for the Fourier analysis of the system to easily detect the secular frequencies. The profile of the laser will

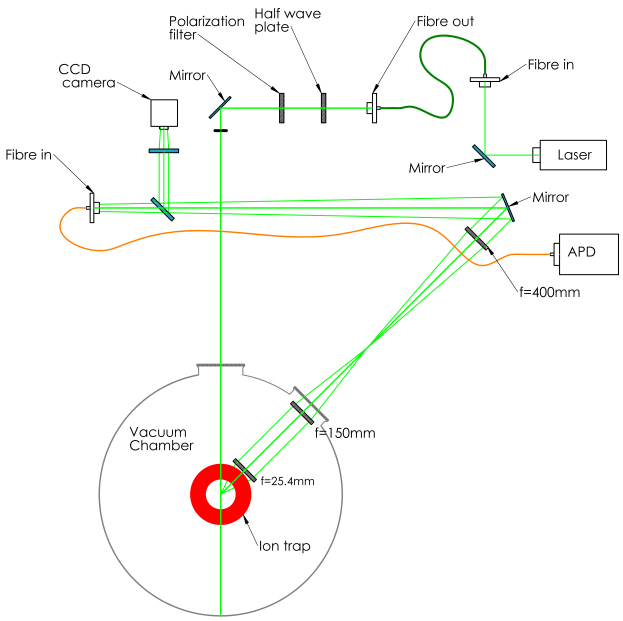

Figure 3.3.1: Sketch of CODE's optical system. Both illumination and reception systems are shown. The illumination system encompasses everything from the laser to the ion trap, and the reception system encompasses everything from the ion trap until the APD. All components are listed.

also affect the capacity of the system to correctly measure the secular frequencies of the particle. Care must be taken to ensure a clean Gaussian beam profile (TEM 00) as shown in figure 3.3.3. Modes such as TEM 10 and 01 can cause multiple peaks in a single oscillation, and thus give us incorrect measurements of the particle's frequency.

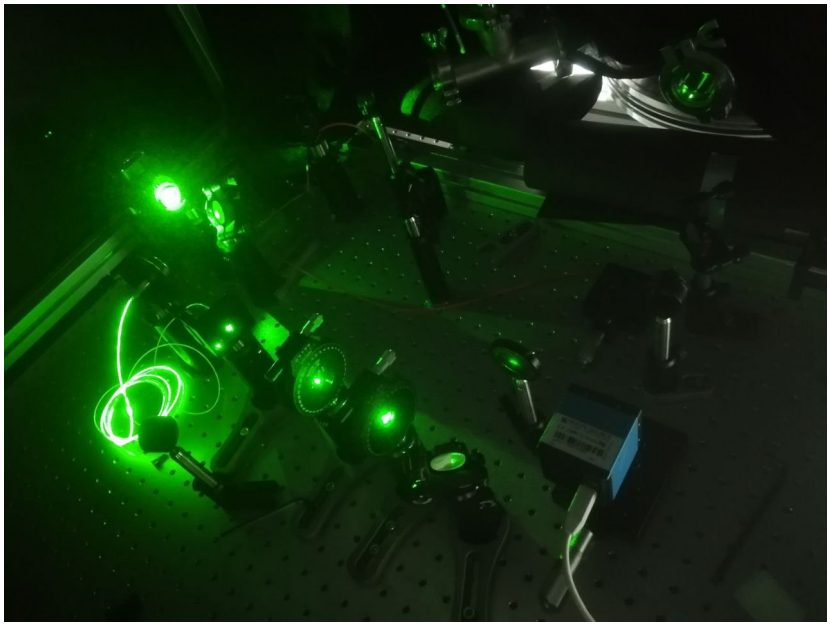

Figure 3.3.2: Picture of the CODE optical system without cross illumination covers for a complete view.

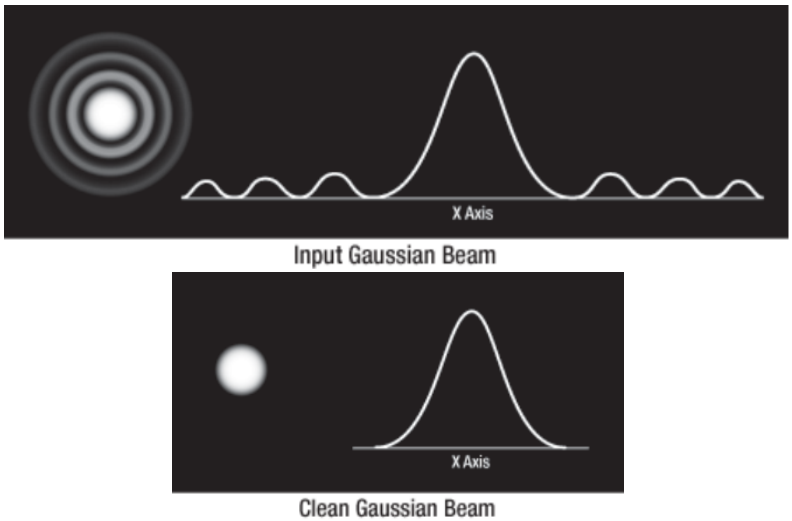

Figure 3.3.3: Comparison between a clean (bottom) and an unclean (top) Gaussian beam

The laser used for the experiment is a 532nm laser from Civil laser (LSR532NL Civil laser 500mW) Its characteristics are detailed in table 3.3.1. The laser has a multi-mode output (Specifications state that its output is near TEM 00, but experimentally, it has shown this is not true). To clean the laser beam, it is passed through a single-mode optical fibre to remove the unwanted modes.

Output Wavelength	532	nm
Output power Max	500	mW
Spatial mode Near	TEM 00	
Pointing Stability	< 0.05	mrad
Beam Diameter (1/e2):	< 2.5	mm
Beam divergence (Full angle)	< 1.5	mrad

Table 3.3.1: LSR532NL Civil laser specifications

Light scattered from particles much smaller than the wavelength of the incident light, as is the case for the CODE experiment, is scattered within the Rayleigh scattering regime. In the Rayleigh scattering regime, the scattered light from a particle much smaller than the wavelength is given by:

$$I_{scattered} = I_0 r^6 \frac{1+\cos^2\theta}{2d^2}\left(\frac{2\pi}{\lambda}\right)^4 \left|\frac{m^2-1}{m^2+1}\right|^2 \tag{3.3.1}$$

here d is the distance to the particle, r the radius of the particle θ the scattering angle and m the refractive index. As we can see in 3.3.1 the intensity of scattered light increases with θ with a maximum at 90°. We use a 45° angle for our reception system due to experimental constraints. Rayleigh scattering will polarise unpolarized light, and maintain the polarisation of polarised light. Fig. 3.3.4 shows the polarisation rate of scattered light as a function of the scattered angle for unpolarized light, and 3.3.5 shows the distribution of scattered light for different polarisations with respect to the scattering plane. The degree of polarisation for incident unpolarized light follows:

$$P = \frac{1-\cos^2\theta}{1+\cos^2\theta} \tag{3.3.2}$$

This value is independent of the particle size (whilst the particle remains within the Rayleigh limit), thus polarisation of the scattered light gives us no additional information; however, we can use polarisation of the incident light to attempt to reduce unwanted reflections.

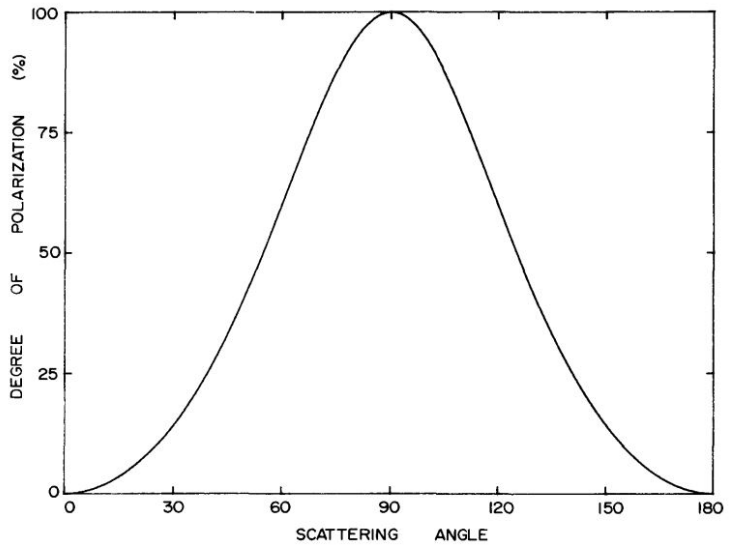

Figure 3.3.4: Polarisation of Rayleigh scattered unpolarized light

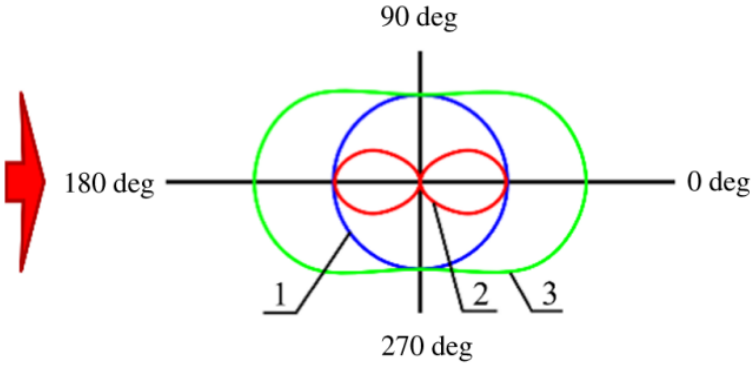

Figure 3.3.5: Rayleigh scattering light distribution for different polarisations from (Polarised light). 1,2 & 3 show the light distribution for Perpendicular to the scattering plane, Parallel to the scattering plane and unpolarized light.

3.3.1.1 Detection system

The reception system, as shown in Fig. 3.3.1, can guide the scattered light from the trapped nanoparticles into two different devices. A CCD camera, Imaging Source DMK 41AU02 and an Avalanche PhotoDiode Laser Components Count 50C. A tiltable mirror is used to guide the light either to the APD (down position) or the camera (up position). The reception system uses 3 plano-concave lenses to focus the light into the APD and 1 extra lens for the camera. The first lens is a 25.4mm plano-concave lens placed at $\sim$ 25.4mm from the centre of the trap, the

second lens has $f = 100mm$, and the final lens has $f = 500$mm, this gives a zoom of $\sim \times 15.5$.

The main analysis mode is done via the APD. The APD emits TTL pulses when it receives a photon, which are then counted by an FPGA, and it then sends the information to a computer at 100 kHz. The program in charge of monitoring the APD shows us both the number of pulses vs time and a Fourier spectrum of the signal. A detailed review of the FPGA system is listed in section 3.5, and the program is shown in Fig. 3.3.6.

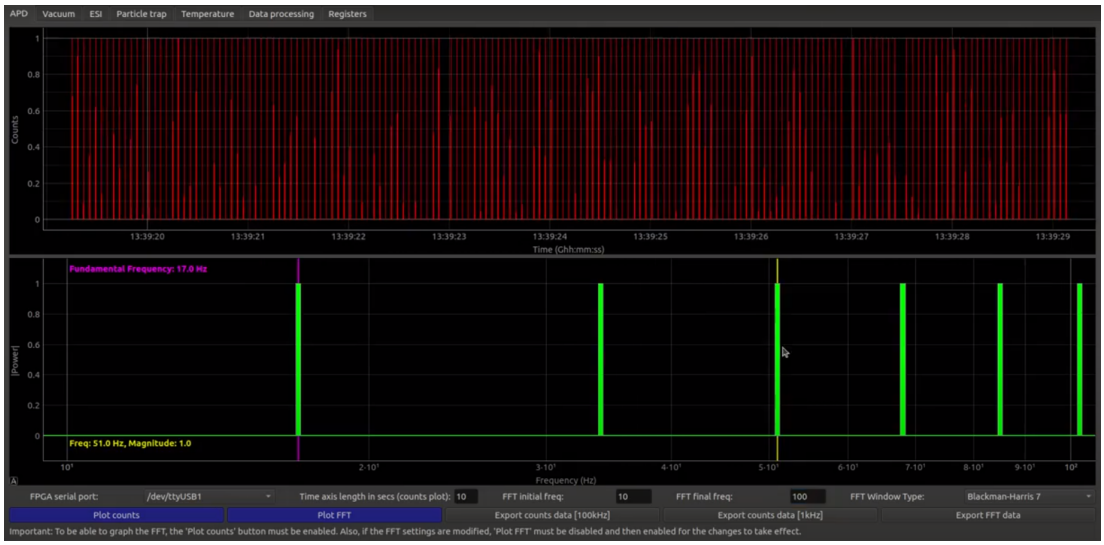

Figure 3.3.6: CODEs control software. The red graph shows the counts sent by the APD with a 500 Hz sample rate. The green graph shows an FFT of the APD counts with a 0.1 Hz resolution and a maximum frequency of 50 kHz.

The secondary analysis mode of the system is via the CCD camera. For the camera system, an additional lens of $f = 125$ mm with a zoom of $\sim \times 3.9$. The camera system gives us a robust troubleshooting viewing mode inside the trap, allowing for easy visualisation of the trapped particle to ensure a correct trapping process. Additionally, we can more easily detect any stray reflection that would increase the noise in the APD signal. The camera's line of sight was characterised using a standard microscope calibration matrix and has a size at focal distance of 1.5 mm $\times$ 1.2 mm. The camera also allows us to view the Lissajous curves created by the motion of the particle, while this might not be crucial for frequency analysis, it gives us a good estimate of the relationship of the $\omega_{r,0}$ & $\omega_{z,0}$ relation

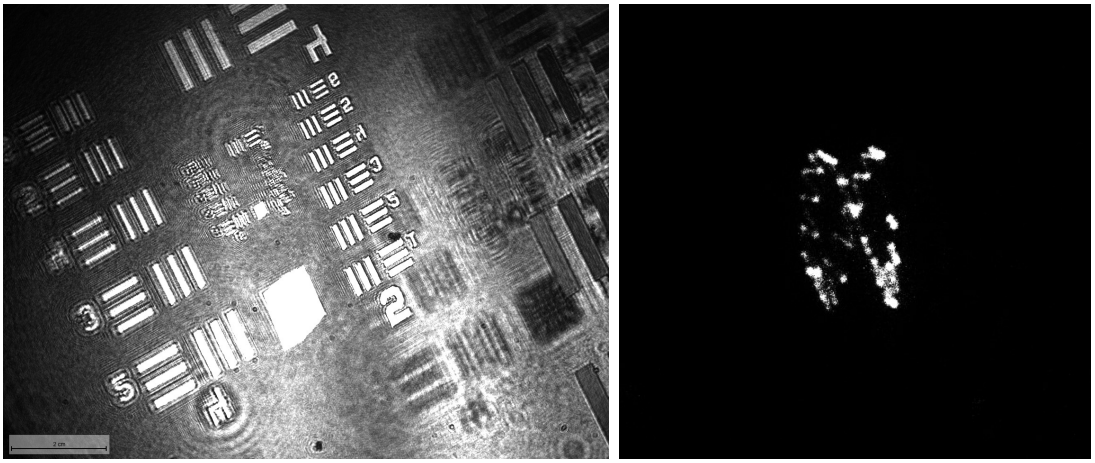

Figure 3.3.7: Left: Line of sight of the CCD camera, a minimum resolution is $1.20\mu m/pixel$. Right: A nanoparticle trapped inside the CODE experiment. The long exposure time allows us to easily view the Lissajou curves of the motion.

3.4 Charge stepping system

To study the mass and mass changes of a trapped nanoparticle inside an ion trap, we must first measure its charge. To measure the charge of a trapped NP, we must naturally first measure its secular frequencies; either ω_r or ω_z can be used for these measurements. Using the secular frequencies of the particle, we can acquire the mass-to-charge ratio of the NP M/Q

$$\omega_{u,n} = \left(n + \frac{1}{2}\sqrt{a_u^2 + \frac{q_u^2}{2}}\right)\Omega \tag{3.4.1}$$

Here we will generally use the first frequency $n = 0$, and for the case of CODE, we tune the voltage of the traps to have $V_{DC} = 0$ so that $a_u = 0$, we then have that:

$$\omega_{u,0} = \frac{1}{2\sqrt{2}} q_u \Omega \tag{3.4.2}$$

$$\omega_{u,0} = \frac{1}{2\sqrt{2}} \frac{8V_0 Q}{M(r_0^2 + 2z_0^2)\Omega^2}\Omega \tag{3.4.3}$$

$$\frac{M}{Q} = \frac{2^{3/2} V_0}{\omega_{u,0}(r_0^2 + 2z_0^2)\Omega} \tag{3.4.4}$$

Once we have calculated the M/Q ratio of the particle, we can do some fine adjustment of the frequencies to ensure that we are in a stable region of the (a,q) graph (2.1.5 for reference) to ensure that the NPs stay trapped. Depending on the polarity of the particle (+ or -), we will use a different system: if the trapped NP are negatively charged, we will use the electron gun (Prevac ES40C1 with a Prevac ES40PS power source), if the particle is positively charged, we can take advantage of the ions generated by the cold cathode gauge to charge our NPs.

Once we are able to change the charge of the NPs, we can proceed with the derivation of the charge from the data. To do this, we can consider the smallest charge step $1e$, we then have that the charge will be $Q_c = Q + e$, and we will have a new frequency:

$$\omega_c = \frac{2^{3/2} V_0 Q_c}{M(r_0^2 + 2z_0^2)\Omega} \tag{3.4.5}$$

We can redefine $\frac{2^{3/2}V_0}{(r_0^2+2z_0^2)\Omega}$ as K for readability and we have:

$$\omega_c = K \times Q_c/M \tag{3.4.6}$$

we can then expand our Q_c term and compare both functions $\omega_c - \omega = \Delta\omega$

$$\omega_c = \frac{KQ_c}{M} \tag{3.4.7}$$

$$\omega_c = \frac{K}{M}(Q + e) \tag{3.4.8}$$

$$\Delta\omega = \frac{K}{M}(Q - Q + e) \tag{3.4.9}$$

$$\Delta\omega = \frac{Ke}{M} \tag{3.4.10}$$

$$M = \frac{Ke}{\Delta\omega} \tag{3.4.11}$$

Thus, we can obtain the mass of a trapped ion M from the amplitude of the frequency shift from a known charge step.

3.5 Data acquisition & control software

The CODE software is custom-built for the experiment. It was built by our team's software engineer, Brian Andler and Prof. Sobarzo. It allows for control of all components capable of communication with other hardware (roughing pumps, for example, do not have direct control from the software). Fig. 3.5.1 shows a diagram of the architecture of the program. The program uses different communication interfaces for the different instruments connected to the CODE workstation; each instrument can have one or more modules that process writing and reading.

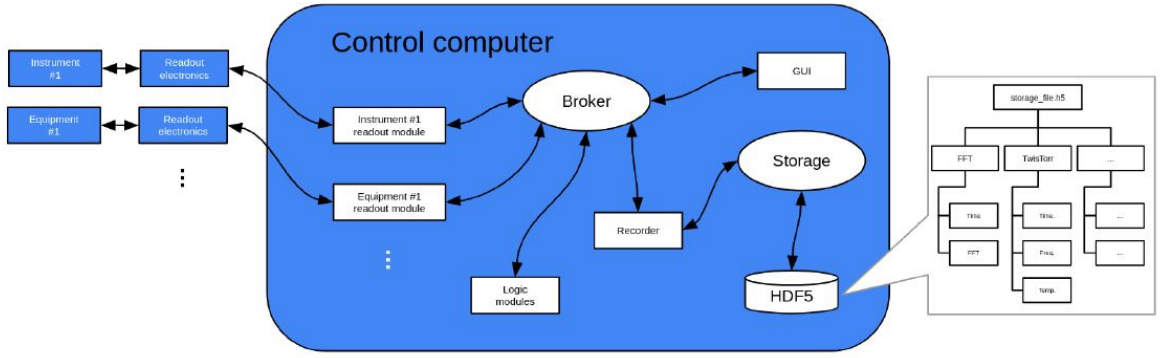

Figure 3.5.1: CODE software system architecture

The control system uses a server-client architecture implemented using gRPC; the system uses 2 servers, the broker and storage, shown in fig 3.5.1 as white ovals. The broker controls the communication between the 3 different modules of the control system. There is no direct communication between the different modules, and the Storage server holds the data. The modules that connect the equipment can either only read or write, and if necessary, can do both at the same time to ensure only the necessary data is consumed.

The data flow of the system is shown in fig 3.5.2, the red lines indicate data flow from the APD, the green lines are instruments connected through RS485, in magenta data from the E-gun and in blue data from the oscilloscope. The solid lines indicate data flow coming from each device/node, while the dotted lines indicate setting values for each device/node.

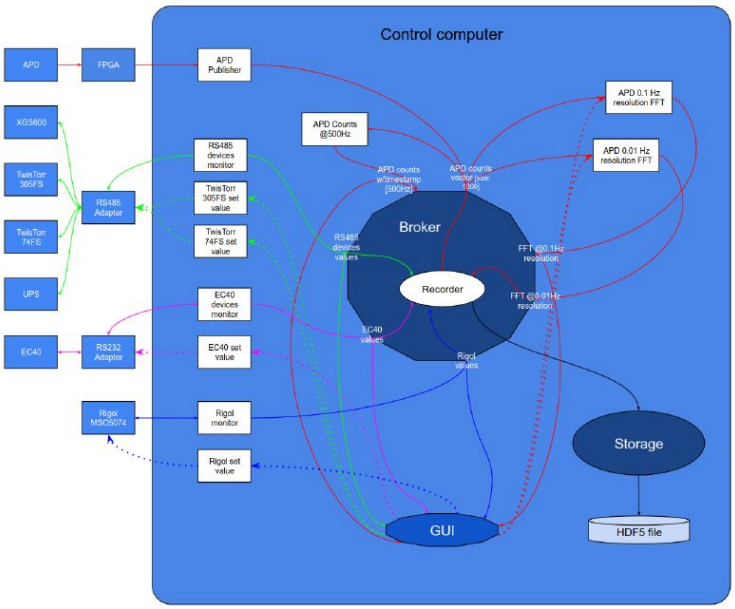

Figure 3.5.2: Data flow in the code system, APD data is shown in red, RS485 connections shown in green, E-gun in magenta and oscilloscope data in blue.

The different instruments that are connected to the CODE workstation are connected by different communication protocols (fig 3.5.3) used for the different instruments. Some instruments, like the APD and the laser, need to be connected to another system to allow the workstation to correctly communicate with the control system.

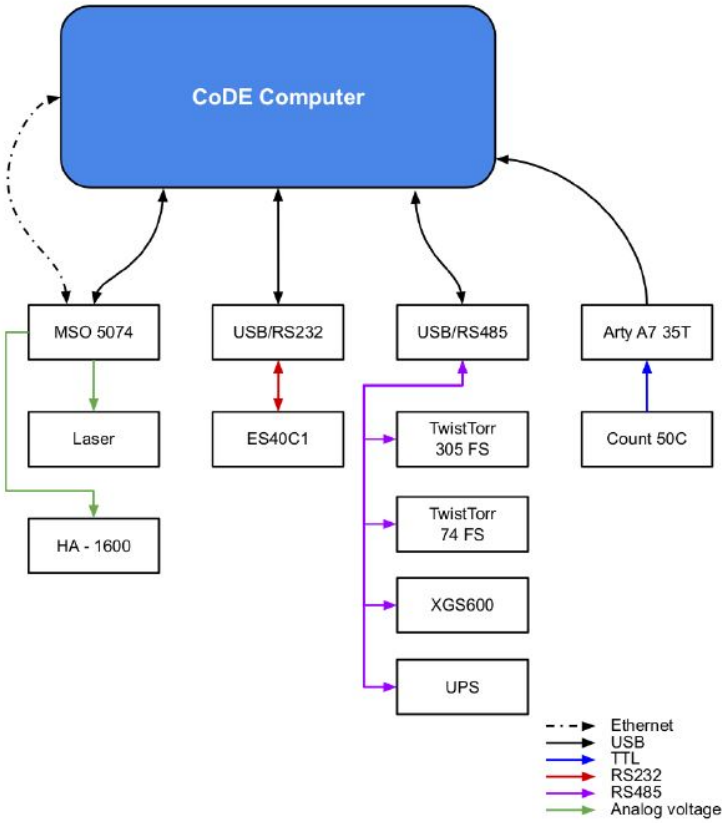

Figure 3.5.3: The connection scheme of the CODE experiment, each system uses a distinct connection type to prevent communication issues

The GUI of the CODE control system is shown in Fig. 3.5.4. The GUI has 5 different tabs that control different parts of the experiment. There is also a side panel with general information of the experiment from each tab, such as vacuum level, trap voltage, electron gun status and APD on/off. The APD tab shown in fig 3.5.4 allows for quick viewing of the APD signal (a 500 Hz version), its FFT (0.1 Hz resolution) and a waterfall graph of the peak intensities of the FFT. The vacuum tab handles the turbo pumps (on/off) and shows a graph of the pressure. The electron gun tab controls the electron gun and shows a graph of the highest peak of the APD FFT vs time to see the change in frequency with charge steps for charge stepping procedures. The trap tab controls the Rigol oscilloscope used to generate the signal that powers the trap; it also shows a graph of the oscilloscope signal of the trap voltage.

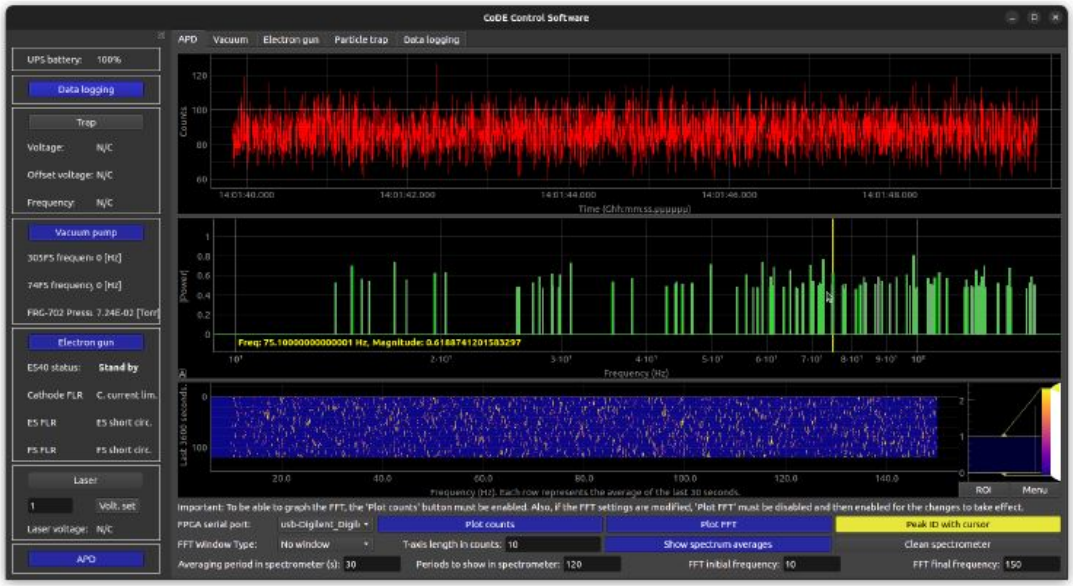

Figure 3.5.4: Control system's GUI interface, the different tabs on the top control different parts of the experiment, shown is the APD tab where we can see a 500Hz APD count graph in red, an FFT of the APD signal with $0.1Hz$ resolution in green and a waterfall graph of the FFT peaks in yellow.

The final tab, the data tab shown in fig 3.5.5, is where we set up our data file generation for the CODE system. The files are formatted in HDF5 format to reduce file size and computation time in analysis. To create files, one must first choose what variables the files will hold. Data from each tab can be stored in the data files, with the condition that the corresponding instruments are connected to the software. For the APD data, the counts are outputted in grouped arrays of 100 counts, in the case of the FFT, the base FFT used in data storage is a 100 second FFT sample with $0.01Hz$ resolution, one can set how many FFTs will the program average beofre writing in the data file, files can be set in any folder, and can be set to a fixed amount of time before generating a new file to avoid inefficiently large files in long experiments.

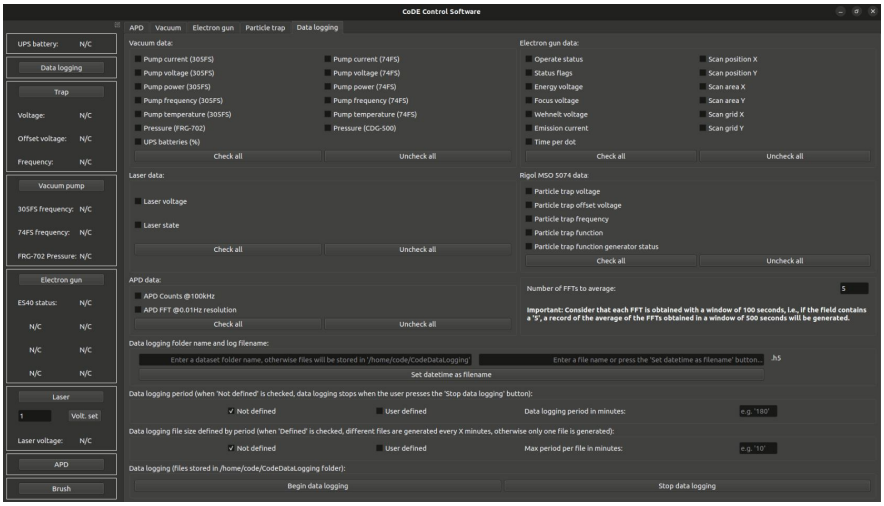

Figure 3.5.5: Data tab of the control system shown are all of the tabs that allow for different information to be stored in the data files.

Chapter 4

Particle injection

4.1 Particle injection system

The particle injection system is one of the most critical components of the experiment, as its correct functioning will determine our control over the properties of the injected nanoparticles. In this section, we will explain the systems used in the CODE experiment to inject nanoparticles into the ion trap inside the vacuum chamber.

4.1.1 Electrospray Ionisation (ESI)

The experiment uses an Electrospray Ionisation System to inject charged nanoparticles into the vacuum system. The following discussion is a summary of Kebarle and Verkerk (2009) and Banerjee and Mazumdar (2012).

Electrospray ionisation is a soft ionisation method that allows for multiple charging [M + zH]z+ ions. This method is compatible with analytes within a wide range of masses and compositions, from organic molecules such as peptides, polymers and proteins to inorganic ions with masses from kilodaltons to hundreds of megadaltons.

Electrospray ionisation can be divided into three steps to better understand the process. 1) Charging of solution droplets at the tip of the capillary emitter. 2) The fission process of the charged droplets and the disintegration process by which the analytes pass into the gas phase. All of these stages occur at atmospheric pressure; the ESI system does not require vacuum to function, but it is used to

inject charged analytes into vacuum systems.

The capillary used in ESI is maintained at high voltage ($2 - 4$kV), because of this electrical field at the capillary tip is extremely high; its value can be calculated considering that the tip is opposite to a large grounded counter electrode by the following equation.

$$E_c = \frac{2V_c}{r_c \ln(4d/r_c)} \tag{4.1.1}$$

Here V_c is the applied potential, r_c the capillary outer radius and d the distance from the tip to the counter electrode. We can see that E_c is inversely proportional to r_c with a weak dependence on the distance to the counter electrode. The solution used in ESI is typically a polar solvent (typically methanol, water, acetonitrile or a mixture of these) will be penetrated by the electric field, since the field will be higher at the capillary tip the solution will become polarized around this point and the positive and negative electrolytes in the solution will move under the influence of this field (according to the polarity of the field, since our ESI system runs on positive charge we will consider this as basis in this discussion) in our case this will lead to an increase in positive ions near the surface of the tip droplet. The forces due to this polarisation of the droplet cause a change in the shape of the droplet into a cone called the Taylor cone. The electrical field acts against the surface tension, increasing the surface of the Taylor cone. If the field is sufficiently strong, the tip will become unstable and emit a fine jet of droplets that are charged by the positive ions of the Taylor cone.

We can use an approximate equation derived by Smith (1986)) for the potential to generate electrospray V_{on}.

$$V_{on} \approx \left(\frac{r_c \gamma \cos(\theta)}{2\varepsilon_0}\right)^{1/2} \ln\left(\frac{4d}{r_c}\right) \tag{4.1.2}$$

Here γ is the surface tension, ε_0 the permittivity in vacuum, r_c the radius of the capillary, and θ is the half angle of the Taylor cone. Analysing typical solvents used for ESI, we can see that water (H_2O) has the highest surface tension, hence

will require higher potentials to generate the Taylor cone. This potential will be the same for both the positive and negative modes. High potentials, particularly in clear water (due to the high V_{on}), can lead to electric discharges. Electric discharges in the ESI reduce its performance (reduced amount of analyte ions generated), more so in the presence of these discharges, discharge-generated ions are created, such as $H_3O^+(H_2O)_n$ from water or $CH_3OH_2^+(CH_3OH)_n$ from methanol.

The charged droplets generated in the electrospray will move in the direction of the counter electrode. While moving, they will shrink due to solvent evaporation; the energy for this evaporation is provided by the ambient gas. This size reduction will cause the electrical field normal to the surface of the droplets to increase; it will reach a limit once the repulsion between the charges inside the droplet is larger than its surface tension and will cause it to split into multiple smaller droplets via a release of a small jet. This process is called Coulomb fission or Coulomb explosion and is given by the Rayleigh equation:

$$Q_{Ry} = 8\pi(\varepsilon_0 \gamma R^3)^{1/2} \tag{4.1.3}$$

Here Q_{Ry} is the droplet charge, g the surface tension of the solvent, R the radius of the droplet and ε_0 the electrical permittivity. Peschke et al. (2004) calculated that about 40% of solvent is lost due to evaporation whilst a mere 2% is lost due to fission. This loss of solvent means that the concentration of solutes in the droplet will increase 29-fold.

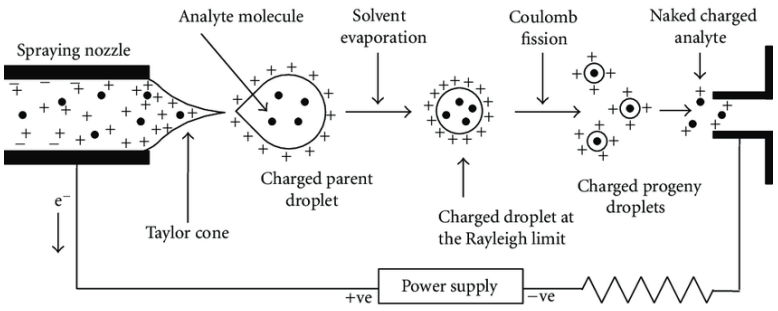

Figure 4.1.1: Schematic representation of an Electrospray Ionisation System (ESI)

The last part of the process, the formation of gas phase ions, has been explained by two different mechanisms, the Charge Residue Model (CRM) and the Ion Evaporation Model (IEM). The CRM model explains the process for larger analytes (macromolecules and nanoparticles), while the IEM is used to explain the process for smaller ions. Since we work with large silica nanoparticles, we will focus this discussion on the CRM model as it is better suited to explain the conditions of the CODE experiment.

The Charge Residue Model states that some of the droplets only contain a single analyte. Due to the solvent evaporation process, the solvent would evaporate, leading to a gas phase ion, with the charges of the droplets attached to the surface of the analyte. This model was based on theoretical evidence (later experimental data were in line with the theory) that the evaporating droplets stay close to the Rayleigh limit (within 75% of the value). We can then approximate the number of charges on the analyte by relating its size (considering spherical macromolecules or nanoparticles) from $M = 4/3\pi\varphi R^3 N_A$ with the Rayleigh limit charge of a droplet of the same size to yield:

$$Z = 4\left(\frac{\pi\gamma\varepsilon_0}{e^2 N_A \varphi}\right) \times M^{1/2} \tag{4.1.4}$$

This relation is obtained from replacing the value for the Radius of the analyte in equation 4.1.3. This is in good agreement with historical experimental data that give an M exponent of 0.53.

4.1.2 ESI in the CODE experiment

The ESI system for the CODE experiment then requires precise control of the following variables to form an efficient ion injection system.

- Distance Capillary Emitter $[mm]$
- Voltage power supply $[V]$
- Syringe pumping speed $[nLm/min]$
- Size of the emitter
- Solvent

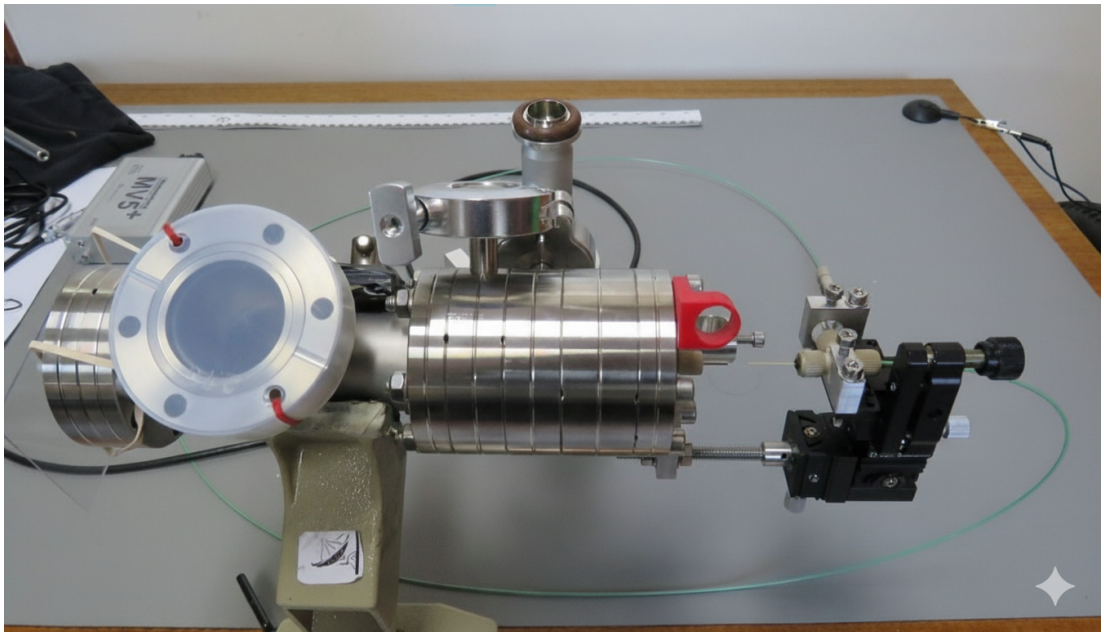

Figure 4.1.2: The Molecular spray UHv4i electrospray system before being connected to the experiment.

Fig 4.1.2 shows the setup for the ESI system, CODE uses a Molecular spray UHV4i electrospray system mounted on a single axis platform allowing for both motion on the $X-Y$ plane (from the Molecular spray UHV4i) and the Z axis (single axis platform) the power source of the ESI allows us to set a positive voltage within the range of $0-5000\,\mathrm{V}$. To pump solvent onto the capillary, CODE uses a model 1002X New Era Pump system microfluid syringe pump; the flow can be set up to $9990nL/min$.

Optimisation of the electrospray plume was done via observation with a small microscope. The optimisation was done with the following criteria: Stability of the Taylor cone size of the ESI plume, condensation on the entrance capillary. Stability of the Taylor cone is crucial for a consistent ion flow in vacuum, the shape of the plume will impact the density of nanoparticles per cm^2 so we do not want the ESI plume to be to large finally the condensation on the entrance capillary signifies that the evaporation process of the nanoparticles is not fully completed for a % of the droplets, this will strongly affect the systems capacity to inject ions into the vacuum system. Additionally, the plume position was adjusted using a long exposure deposition gradient as a reference. The optimised values for the ESI systems are the following: distance $22cm$, voltage $4190V$, flow $850nL/min$, solvent clear water, emitter internal diameter is $108\mu m$. Fig. 4.1.3 shows the ESI

plume generated by the CODE experiment.

Figure 4.1.3: ESI emitter plume using the previously detailed parameters

4.1.3 Injection to vacuum by ESI

We know from previous tests that the ESI system is correctly generating gas phase ions; however, confirmation and characterisation of the ion flow at the position of the trap inside the vacuum system is not secured just by optimising the ESI system. Thus, tests were done to ensure that particles are effectively entering the vacuum system up to the position of the trap.

Two different configurations were tested for vacuum injection; for each configuration, two tests were done to analyse the effectiveness of the configuration. Scattered light analysis using both an action camera and an APD, and a deposition test on a glass wafer that is analysed with an electron microscope to see if there are particles attached to the surface

For the first setup tested, the travel length of the ESI ions was increased by adding an additional four-way connection to the vacuum system. This increased the travel distance of the ions by an additional 15cm, with a total travel distance of 45cm (near the suggested maximum working distance of 52cm stated by the supplier). The travel length was increased in an attempt to reduce the speed of the nanoparticles. The vacuum chamber was placed at 10^{-3}mbar by injecting argon into the chamber. The second setup removed the extension of the injection system, reducing the travel length. The reduced travel length should increase the density of particles per cm^2 at the position of the trap.

When looking at the results for the first configuration, we found no evidence of particles flying by both the APD and camera measurements and glass deposition.

For the second "short" configuration, again the APD and camera could not detect flying particles. When analysing these negative results, one explanation other than a lack of flying particles is that the time the particles stay within the line of sight of the light detection system is too low to generate enough signal for the APD or action camera to detect. The camera system views an area of $\sim 1.5 \times 1.2\,\mathrm{mm}$

Results for this setup were almost completely negative, no visualisation of the particles with the APD or action camera and no visualisation of particles in the sample holder

4.2 Particle deceleration simulations

Particles ionised by the ESI system enter the vacuum chamber at incredibly high speeds (around $100 - 350 m/s$); this presents an issue to the experiment since split ring ion traps are not designed to trap fast moving particles, the AC electrical field will not remove enough energy from the particle to successfully trap it (considering that the phase of the AC is such that the deceleration is maximum). In order to trap particles coming from the ESI system, deceleration of said particles is critical. To decelerate said particles, we propose 3 different methods: 1)Deceleration via Oscillating Electrical fields, 2)Deceleration via collision with non-reactive molecules (gas collision) and 3)Deceleration via optical force. Various simulations of the ESI/Trap system were computed in order to understand the most effective ways to decelerate our particles. In the following section, details of the work done in simulations to find a solution to this problem are presented.

Speed requirements

We must first understand the speed requirements of the SRET. As mentioned before, the SRET is not able to capture fast-moving particles; there is a threshold velocity that these particles must have for them to be trapped by the trap. Simulations in SIMION were done to estimate the maximum speed that the trap can tolerate, to determine our goals for the decelerating system. The simulation were done by placing the ions within a spherical distribution around the centre of the trap and given an initial speed along the X axis (this is the direction that they would fly from experimentally) the mass of the particles is that of a 300nm particle (this are the particles that were being used experimentally at the time

of the simulations) and a charge of 2.5E+7 from the calculations of ESI particle charge from 4.1.4. Figure 4.2.1 shows the results of the simulations. We can see that for speeds of $0.0015mm/\mu sec$ the amount of particles trapped is very small; however, since the system only needs a single trapped nanoparticle, we can still consider this as the maximum speed for trapping.

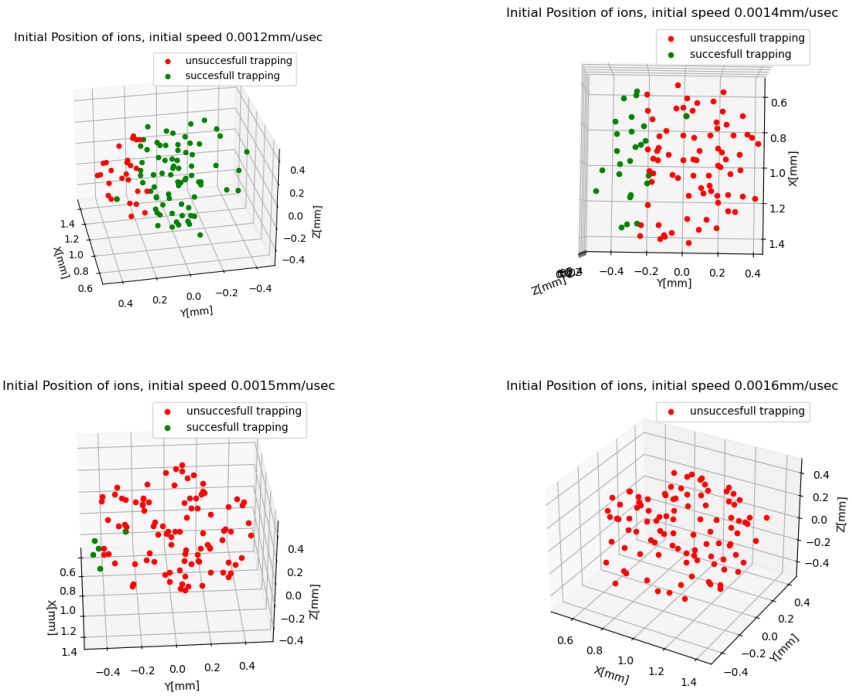

Figure 4.2.1: Results for trapping speed analysis for 4 different speeds, the speed for each graph is listed in its title. We can see that for speed greater than $0.0015mm/\mu sec$ the SRET is unable to trap these particles.

4.2.1 Electrical deceleration

We first proposed a simple system, an electrically charged plate placed before the trap with a pinhole in the centre to allow ionised particles to go through the plate. Initially, the plate (dubbed slowing plate) was to be charged with a DC potential to allow it both to slow down the ions and allow for charge selection of incoming particles. With a DC potential, the only possible position for the plate would be behind the SRET. All positions considered are along the z-axis of the ESI injection system. If the plate is placed in front of the SRET, a DC potential would not slow down the incoming particles, since a DC potential has a conservative nature. When placing the plate behind the SRET, complications

arise with the superposition of the electrical fields. For the DC potential to be effective at decelerating particles, high voltages must be used; this strong potential would strongly reduce the capacity of the SRET to trap ions. For this system to function, pulsed voltages should be used for the SRET to receive the particles without a disturbed potential; however, this would need a complex control system that could discern when a particle is trapped (instead of just a flow of untrapped particles) to turn off the pulsed DC potential to prevent it from destabilising the trapped particle. This method was neglected due to the complexity of the control system.

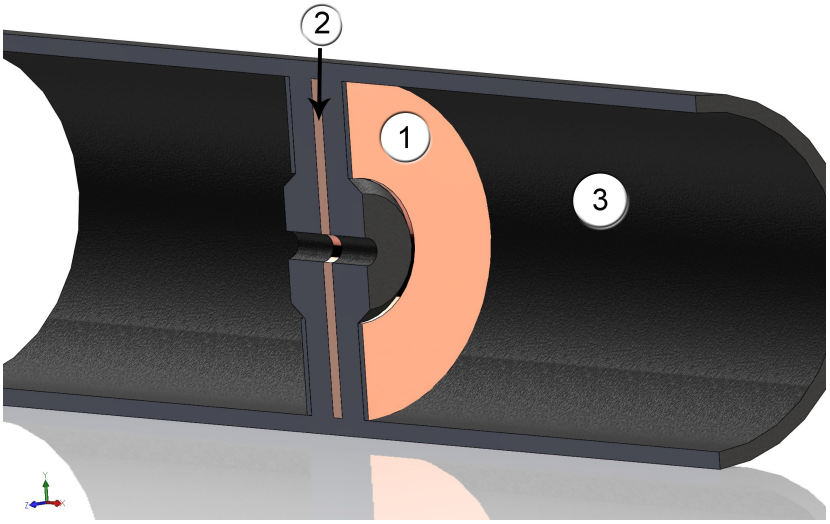

Figure 4.2.2: 3D sketch of the slowing plate system with its components listed. 1. The charged disk plates, there is an identical plate placed mirrored to it at the other side of 2. 2; a Grounded Copper disk to direct the electrical field through the centre hole. 3 the insulating surrounding.

The other configuration studied was placing the plate before the SRET. The design consists of two disk plates charged oppositely, with a grounding plate placed in the middle. The system is surrounded by an insulting material to constrain the E-field. A sketch of the design is shown in figure 4.2.2 is the design proposed for our slowing plate with its different components listed. The idea of the design is to generate a large potential gradient between both electrodes to decelerate the ions. Fig. 4.2.3 shows a 2D and 1D representation of the Potential of the system in a DC configuration. The simulations for the system were done in ANSYS Electromagnetic Desktop using the Maxwell 2D simulator with a finite elements

model. Here we can see and define two parts of the potential: the central high slope differential and the outer softer ramps; we will use the central slope to decelerate the ions.

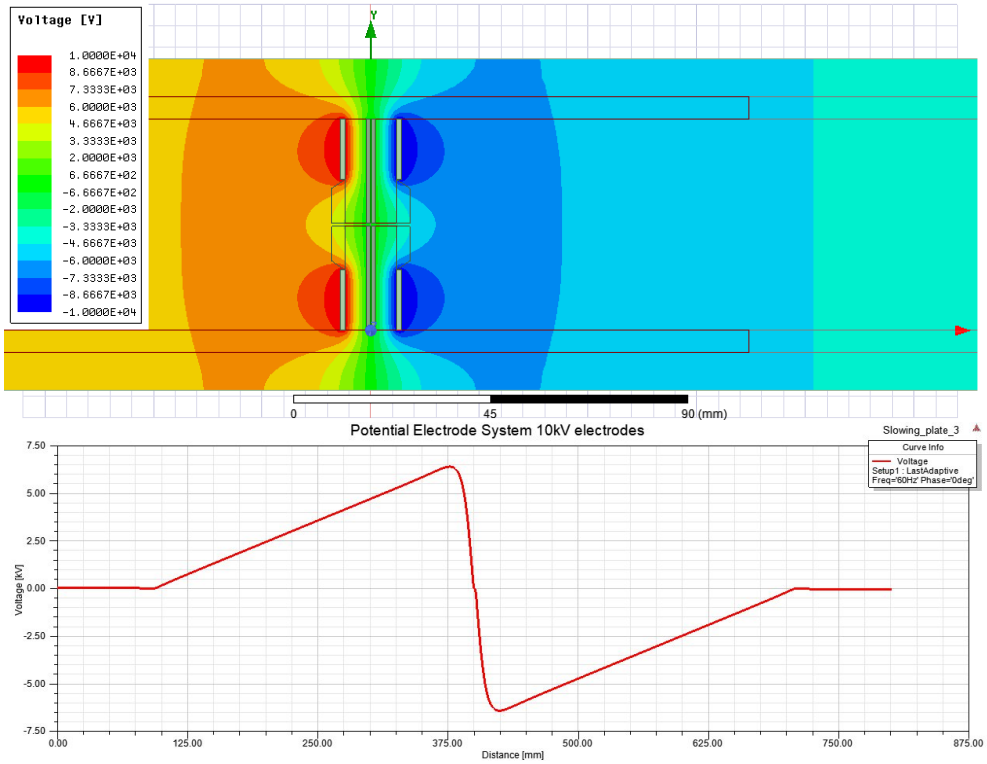

Figure 4.2.3: Top: 2D view of the Electric potential for the ANSYS Maxwell 2D simulation of the deceleration system. Bottom, 1D potential of the simulation along the x-axis.

Now that we have a plausible design, we can begin ion flight simulations. For this simulation, the SIMION software was used. This program is a specialised program to simulate the movement of ions in electromagnetic environments. For the system to work, a square function must be used to reduce the accelerating force created by the electrodes. Initial simulations used the ideal case where the square function is such that the high position has a length equal to the time that a particle takes to fly through the centre area, and a low position with a length equal to the time it takes a particle to fly through the external area. All ions had the same initial speed for this ideal case simulation.

Fig. 4.2.4 shows the results of these simulations. Ions were successfully slowed down by 35.7% using a voltage of $6kV$. We can now study the non-ideal case of a square function. The simulations set the system to have a fixed frequency,

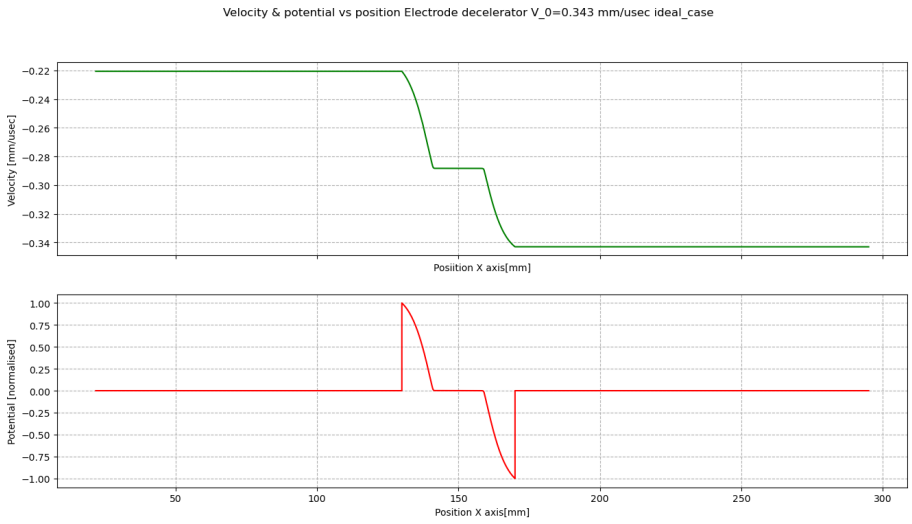

Figure 4.2.4: Ideal case of the deceleration system. Top: Particle speed vs Position through the deceleration system. Bottom: Potential vs position of the particles.

whilst particles are continuously flying through. Particles are set with the same initial speed and are fired at a fixed rate of $1\mu sec$. This represents a more realistic scenario since we have no control over when particles are entering the system with respect to the phase of the decelerator. Fig. 4.2.5 shows the results for the most effective frequency. We can see that most of the particles maintain their velocity, and about the same amount are both accelerated and decelerated. Accelerated particles do not affect the functionality of the trap and will always exist as a consequence of the phase of the system (phase alignment results in decelerated particles, phase inversely aligned results in accelerated particles).

When analysed, we see that the period of the frequency is equal to the time a particle flying at $343m/s$ takes to go through the centre of the system, so this is the closest simulation to the ideal case. We can take advantage of the relation between frequency and speed to use the system as a rough speed filter/analyser, it will only work or better said, it will be most effective. Fig. 4.2.6 shows the effect of a $5kHz$ frequency. We can clearly see a fall in the effectiveness of the system when not in resonance.

The simulations for the AC slowing system show promising results, being able to reduce the speed of particles as a function of both frequency (tuning according to the speed of the particles) and voltage (overall strength of the E-Field or

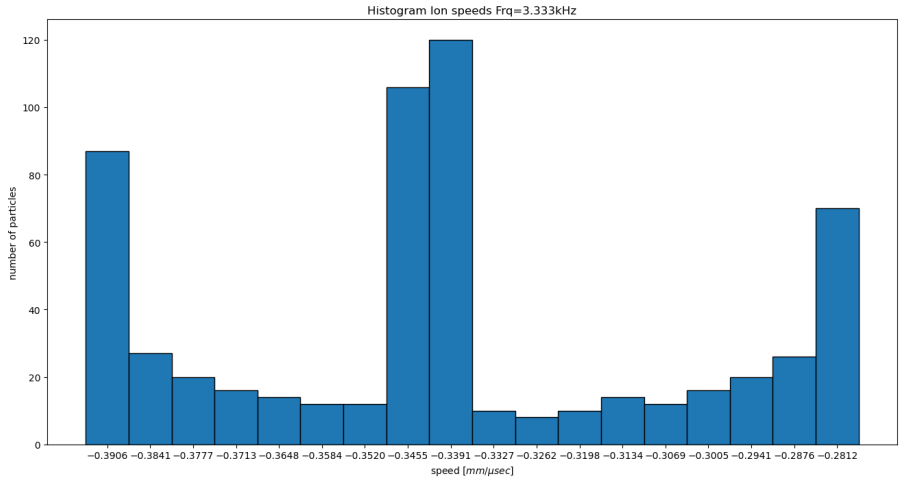

Figure 4.2.5: Histogram of the speeds of nanoparticles after deceleration for slowing frequency= $3.333kHz$. Initial speed of particles was 0.343 $mm/\mu sec$

magnitude of deceleration). Construction of a working prototype of the system is expected, but is not considered within the scope of this work.

4.2.2 Gas collision deceleration

A reliable method of decelerating ionised particles is via elastic collisions with a buffer gas. Argon is mainly used as a buffer gas for this method as it is non-reactive, ensuring that the ions will remain intact after collisions, and it is a relatively heavy atom (considering other commercially available noble gases).
For our experiment, we simulated the effect that argon collisions will have on the speed of the ions; for this, we used a hard collision model. The code for this model is the base hard collision model that is provided by SIMION. The code uses the following features and assumptions:

- Ion collisions follow the hard-sphere collision model.
- Energy transfers occur solely via these collisions.
- Ion collisions are elastic.
- Background gas is assumed neutral in charge.
- Background gas velocity follows the Maxwell-Boltzmann distribution.
- Background gas mean velocity may be non-zero.

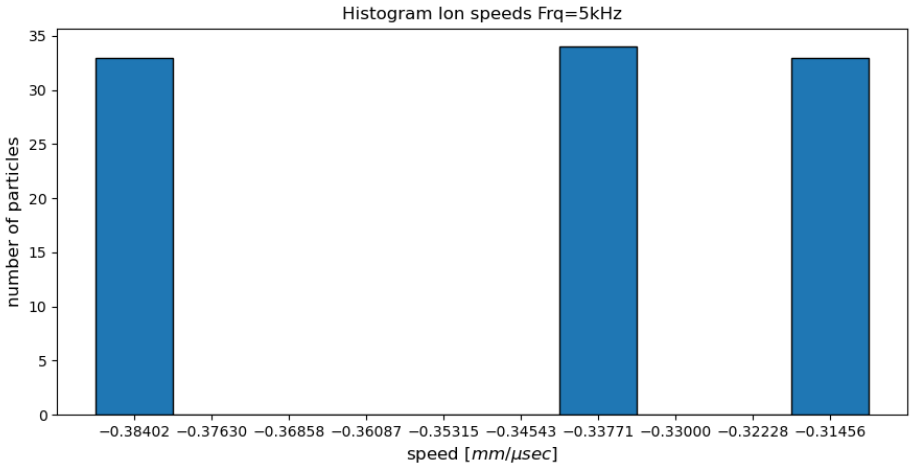

Figure 4.2.6: Histogram of the speeds of nanoparticles after deceleration for slowing speed = $5kHz$. Initial speed of particles was 0.343 $mm/\mu sec$

- Kinetic cooling and heating of ions due to collisions are simulated.
- Kinetic cooling and heating of background gas is assumed to be negligible over many collisions.

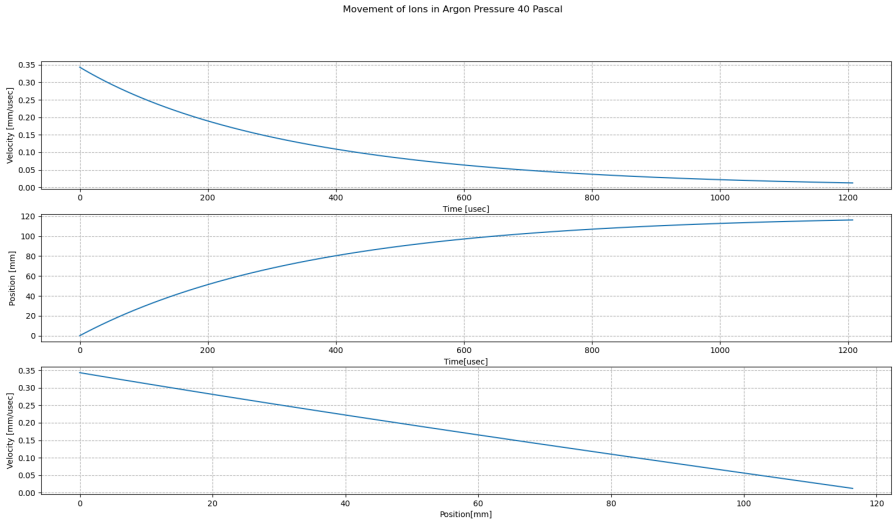

Figure 4.2.7: Results of the hard sphere collision simulation for argon deceleration.

For our simulation, we consider a space with 40 Pa (pascals) of pressure, the particles move along a distance of 12 cm and their speed is recorded. The results of the simulations are shown in fig 4.2.7, which shows that argon deceleration is highly effective at slowing down the ions. However, this effectiveness is limited

by the pressure requirements of the system. The SRET cannot function properly within the range of 10^{-1} mbar due to electric discharges peaking at this pressure range, so we must limit the pressure to a maximum pressure of 10^{-2} mbar(1 pascal). If we follow Epstein's drag equation to calculate particle deceleration in vacuum conditions, we have that:

$$F_{drag} = \frac{8}{3} a^2 n m_{Ar} v v_{avg} \tag{4.2.1}$$

Here a is the radius of the particle, n the number density of argon atoms in the chamber m the mass of argon and v_{avg} is the average speed of argon. We see from this equation that the drag force stays linear with number density, so reducing the pressure from 40 Pa to 1 Pa will reduce the deceleration rate by 40 times. To solve this issue, we can use a differential pumping system to create a pocket of increased pressure in the antechamber of the ESI system.

4.2.3 Optical deceleration

Optical trapping (optical tweezers) is a known technique using the potential gradient of a laser beam to trap particles. What we aim to do is slightly different, using the scattering and absorption forces of either the optical system laser or the CO_2 infrared laser we can remove kinetic energy from it. We can follow the equations from Ashkin (2006) and Torres-Turiján et al. (2011) for the optical forces for a particle in the Rayleigh regime.

The gradient force

$$\vec{F}_{grad} = (\vec{P} \cdot \vec{\nabla})\vec{E} = \quad 1/2\alpha\nabla\vec{E}^2 \tag{4.2.2}$$

$$\text{polarizability in free space } \alpha = \quad \left(\tfrac{n^2-1}{n^2+2}\right) r^3 \tag{4.2.3}$$

$$\text{polarizability in a dielectric medium } \alpha = \quad n_b \left(\tfrac{m^2-1}{m^2+2}\right) r^3 \tag{4.2.4}$$

$$\text{where } m = \quad \tfrac{n_a \text{ (index of sphere)}}{n_b \text{ (index of medium)}} \tag{4.2.5}$$

$$\vec{F}_{grad} = 1/2 n_b \left(\frac{m^2-1}{m^2+2}\right) \nabla\vec{E}^2 \tag{4.2.6}$$

The scatter force:

$$F_{scat} = \frac{P_{scat}}{c} \text{ where P=Rayleigh scattered power} \tag{4.2.7}$$

$$\vec{F}_{scat} = \frac{\vec{I}_0}{c}\frac{128\pi^5 r^6}{3\lambda^4}\left(\frac{n^2-1}{n^2+2}\right)^2 \text{ where } \vec{I}_0 = \text{ incident beam intensity} \tag{4.2.8}$$

$$\vec{F}_{scat} = \frac{\vec{I}_0}{c}\frac{128\pi^5 r^6}{3\lambda^4} n_b \left(\frac{m^2-1}{m^2+2}\right)^2 \tag{4.2.9}$$

and the absorption force

$$F_{abs} = \frac{n}{c}|P|C_{abs} \tag{4.2.10}$$

$$C_{abs} = k^4|\alpha^2|/4\pi \tag{4.2.11}$$

$$k = 2\pi n/\lambda \tag{4.2.12}$$

$$F_{abs} = \frac{n}{c}|P|4\pi^4|\alpha \tag{4.2.13}$$

Using these equations, we can calculate the force the laser systems apply to the particle and analyse if it is strong enough to be used for deceleration. Fig. 4.2.8 shows the results for the CO laser system at 15W. We can see that the maximum acceleration from the absorption force is not high enough to have a meaningful effect on the particle (considering that we have an initial speed of $\sim 343m/s$).

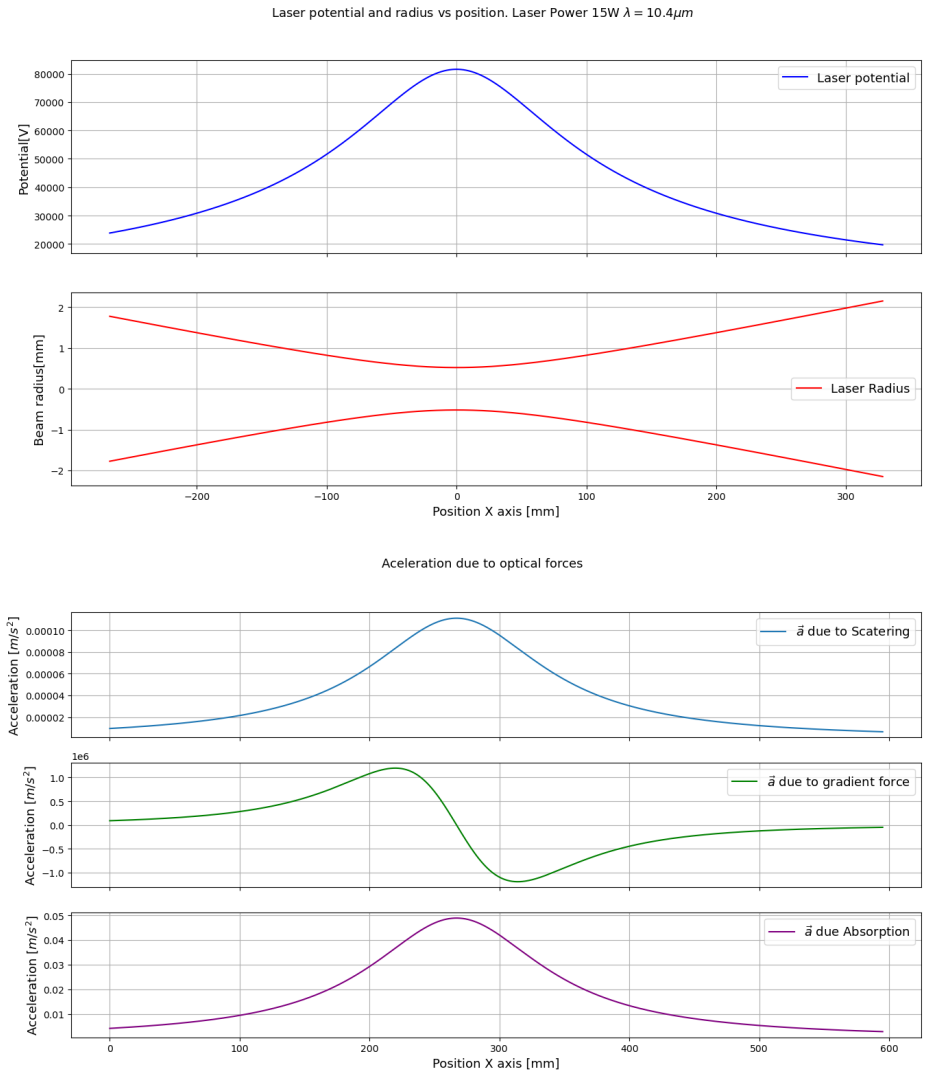

Figure 4.2.8: Top: The shape and Potential of the CO laser for 15W power output, considering a laser radius of 50λ

The analysis for the 532nm laser at $0.4 Watts$(the laser itself has a maximum output of 0.5W, but we consider here the power loss of the optical system) as shown in fig 4.2.9. We can see that the 532nm light is much more effective at decelerating the silica particles; we see that the gradient force has the most prominent effect.

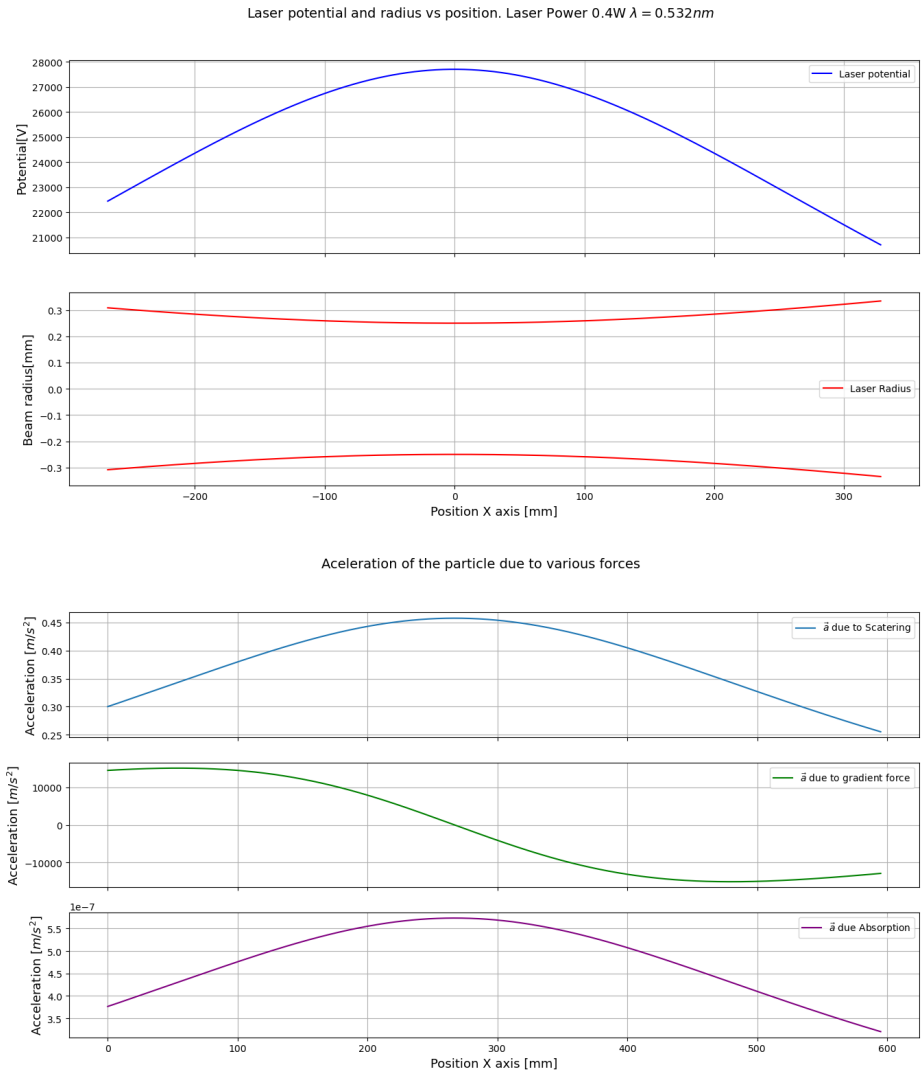

Figure 4.2.9: Top: The shape and Potential of the $532nm$ laser for 0.4W power output, considering a laser radius of $0.25mm$

4.2.4 Triboelectric charging injection

Having stated our experimental limitations with ESI injection, we devised an alternative method of injection for the CODE experiment that could fulfil our injection requirements, but with the advantage of being a more robust system, understanding that this may limit our capacity to manipulate the particles in injection.

Our new system consists of a motor-actuated brush placed on top of the trap. Figure 4.2.10 shows a picture of the actual system placed in the vacuum chamber. The brush is placed in contact with the topmost electrode of the system, and the

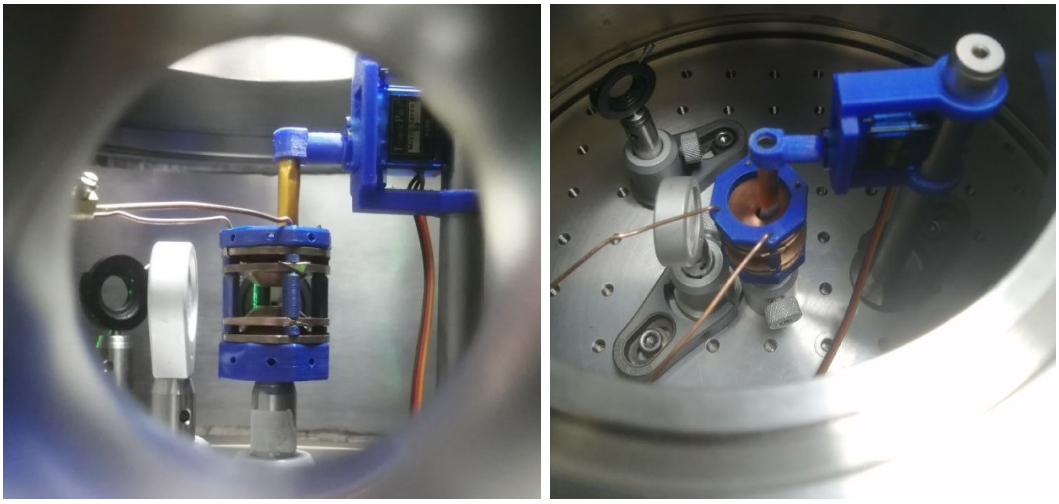

Figure 4.2.10: The brush for the triboelectric injection system of the CODE experiment as seen from the top (opened chamber) and through the lateral viewport.

motion gently presses the brush against the electrode.

The system takes advantage of gravity to move the particles into the ion trap. Because of the small distance the particles have to travel 4mm from the brush to the trap centre, particles do not accelerate enough to prevent trapping. Yielding a consistent trapping rate for the system. The brush system is controlled with an Arduino Uno connected to the CODE workstation. An injection cycle in the trap consists of one full brush stroke (left and right motion) and a return to the 0 central position.

To maximise the trapping capabilities of the system, the pressure is set to $5 \times 10^{-3} mbar$. At this pressure, for each brush cycle, between $0-4$ particles are trapped, with the V_0 and Ω parameters largely affecting the number of particles trapped. Trapping values for the SRET are $V_0 = \sim 700\,\mathrm{V}$ $\Omega = 800\,\mathrm{Hz}$ with this values for a 500 nm silica particle of mass $1.73 \times 10^{-16} kg$ the maximum charge that can be stably trapped is $Q \sim 10e$. Particles trapped in these conditions have a ω_z distribution within the $\sim 40 - 80\,\mathrm{Hz}$. Once the particles are trapped, the trap frequency Ω can be increased up to $3 - 4kHz$. Higher frequencies increase the ω value for a charge step, increasing the accuracy of the mass determination.

Particles injected with this method can be charged by 2 distinct interactions: 1) triboelectric charging with the brush (brush-particle interaction),2) triboelectric charging with the electrode (particle-electrode interaction). When looking at the

effective trapping area of the SRET, an effective volume of radius $\sim 1.5\,\text{mm}$, it is likely that particles directly in contact with the electrodes do not reach the effective trapping volume, so it is more likely that particles trapped in the SRET come directly from the bristles of the brush. So we must then consider a dielectric to dielectric interaction, from the nanoparticles and the brush. Predicting this interaction with accuracy is not an easy task. From Matsusaka et al. (2010) we know that charging via collision can be affected by multiple variables and is very sensitive to experimental conditions. We will only give an estimation of the effect that on the initial charge of the particles, following Schlemmer et al. (2004) and Frimmer et al. (2017) SiO_2 particles are lightly positively charged $\sim n \times 10e$ with $n < 10$ expected, which is concordant with the expected trapping charge. We can consider the motion of the particles in a brush cycle as multiple collisions with the multiple bristles of the brush and other particles. We can then hypothesise that the charge distribution of the particles will narrow as the charge of the particles will distribute between the brush and the nanoparticles. Additionally since the particles are in direct contact for a prolonged time with the brushes we can consider the effective work function equation as an estimate of the charges we will have in our nano particles for silica from Guerreiro et al. (2023) we have that its work function is within the range of $5.4eV$ for the brush, made from nylon we have from Arridge (1967) that its work function is $\sim 4.2 - 4.4eV$. With these values and the effective work function equation:

$$\Delta q_c = C_0 \frac{-(\phi_1 - \phi_M)}{e} \text{C } cm^{-2} \tag{4.2.14}$$

Here we are presented with a problem: C_0 is the effective capacitance of the system, which is not in the scope of this work to calculate. We can then resolve to use an alternative equation from Davies (1969) for the charge density:

$$\sigma = 1.77 \times 10^{-13} \frac{(\phi_n - \phi_s)}{\lambda} \tag{4.2.15}$$

Here, lambda is the charge penetration depth that we will consider the diameter of the nanoparticles of $500nm$ And we can multiply the given surface charge by

the area of the particle, and we obtain a value of $q = -8.1e$. This falls within the same expected range from Schlemmer et al. (2001) and what we expect for our trapping potential.

Chapter 5

Data & Data analysis

5.1 Trapped Particles

To verify that the CODE experiment is working as intended, multiple test runs were done in order to ensure trapping stability, particle charge (positive or negative), functionality of the injection system, particle clumping and the correct measurement of the M/Q ratio.

5.1.1 Purchased nanoparticles

Initial tests were done with purchased 500nm nanoparticles in powdered format. Initial trapping of the NPs was effective within the range of $\Omega = 500 - 2500Hz$,$V = 500V$; however, upon inspection of the secular frequencies of the trapped NP, we found that it was unstable, varying within the range of $\pm 1Hz$ as shown in fig 5.1.1

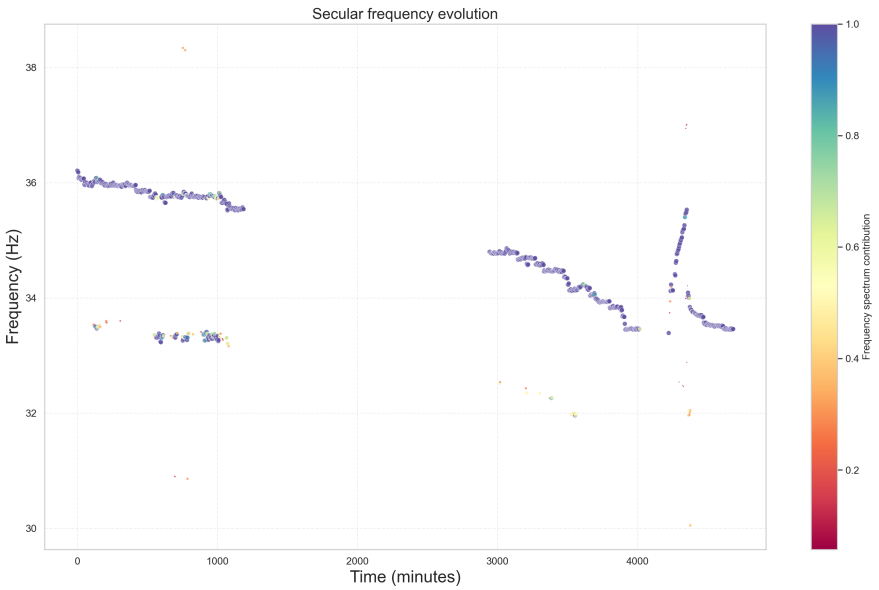

Figure 5.1.1: Secular frequency vs time for a trapped nanoparticle, we can see a clear instability in the secular frequencies.

Upon inspections of the CODE experiment to understand the origin of the instability, we found that the issue could be the nanoparticles themselves. Care was taken to ensure no internal system, such as a pressure gauge or the electron gun, was unintentionally affecting the charge of the particles when not in use by ensuring no powered device was within the line of sight of the trapped NPs.

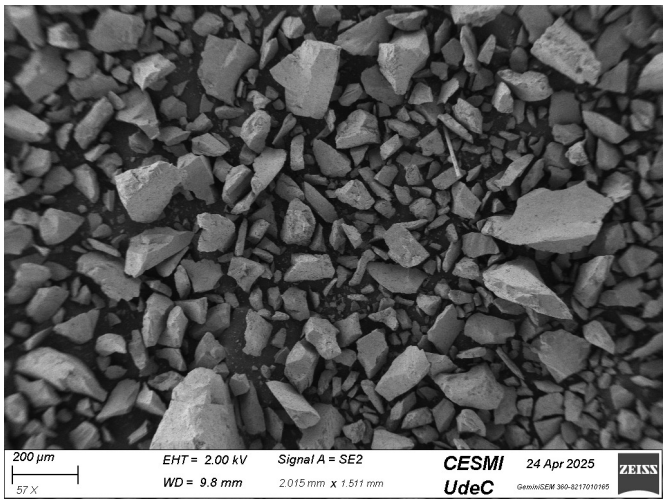

Figure 5.1.2: Nanoparticles viewed with an electron microscope, we see a large variation in size distribution, and this distribution is within the range of $\sim 100\mu$m.

Upon inspection of the particles with an electron microscope, we found that the

NPs were much larger than stated in the data sheet, as shown in Fig. 5.1.2. Particles are not within the size range of $300 - 700$nm we expected, furthermore upon closer inspection to individual fragments, shown in fig 5.1.3, we see clumping of shards of smaller nanoparticles, thus part of the changes in secular frequency could be explained due to small shards of the cluster separating from the main body whilst it is trapped, depending on the surface charge and size of the shard this could resolve into an increase or decrease of the M/Q ratio of the trapped nanoparticles.

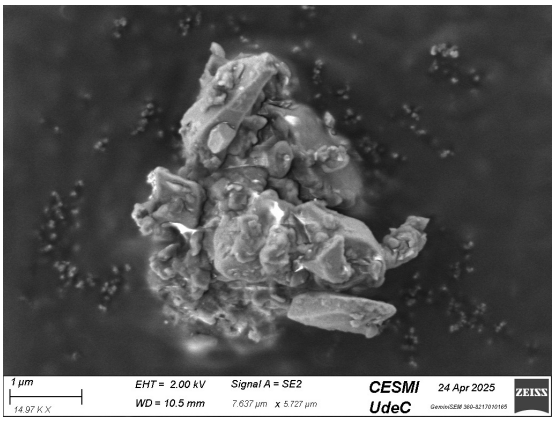

Figure 5.1.3: Shown is a purchased nanoparticle. We see that it is composed of a large clump of smaller silica shards; this can potentially affect its stability when trapped by the separation of the smaller, loosely attached shards.

It was later found that the instability of the charge was likely due to charge variation from Argon ion collisions, generated from the pressure gauge, even though it was not in the line of sight of the trap. This was then used to do our initial charge stepping procedures.

5.1.2 Laboratory made nanoparticles

Following the previous tests, it was evident that the nanoparticles that were currently in use were not suitable for this experiment. New particles were fabricated in the Udec Facilities and are shown in Fig. 5.1.4. Following the Stober method for silica nanoparticle formation (Stöber et al. (1968)), we can fabricate our own silica nanoparticles. The Stober method is a hydrolysis-condensation, that forms spherical silica nanoparticles from silicon alkoxides (tetraethyl orthosilicate, TEOS) using alcohol as a medium. The process uses ammonia as a catalyst by increasing the pH of the solution. The process can produce particles with a size

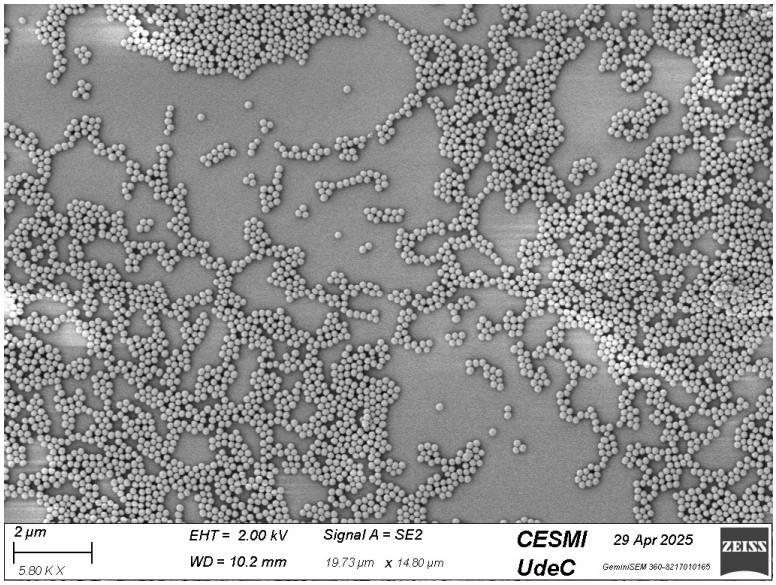

Figure 5.1.4: Particles dried on a glass wafer show a disperse monolayer of nanoparticles. This method of drying the NPs reduces the chance for clumps to form.

from $\sim 50\,\text{nm}$ up to $\sim 1\,\mu\text{m}$. The particles created have a Polydispersity Index (PDI) of < 0.1. Since particles prepared this way are dissolved, we must first dry them for triboelectric injection.

Following Li et al. (2024), we know that silica nanoparticles formed using the Stöber method have a residual layer of OH molecules bonded to the surface when removed from the solution. This layer will affect the surface charge of the nanoparticles and the clumping of the NPs. To try to solve this issue, we heat the NPs at $220°C$ to remove the unwanted layer. When heating and drying the NPs, we must also take into account the conditions in which they are dried. To ensure minimal clumping, the particle solution is placed onto a glass wafer. The solution will spread evenly on the wafer, reducing the number of layers of NPs when the liquid is removed. Fig. 5.1.4 shows an image of the particles when dried with this method, confirming that minimal layers of nanoparticles are formed.

When trapped, the laboratory-made nanoparticles (LNP for abbreviation) showed stable orbits for long trapping periods. Fig. 5.1.5 shows a graph of the change in frequency over time for a trapped LNP, showing stable secular frequencies, as also seen in Frimmer et al. (2017) where they see no change in particle charge under 10^{-5}mbar, validating the stability of our system.

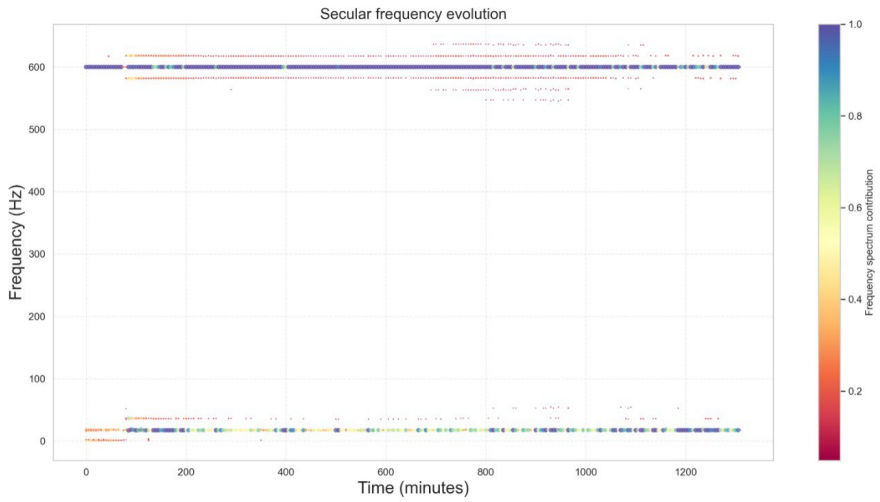

Figure 5.1.5: Frequency vs time for a trapped laboratory-made nanoparticle. We see a clear improvement in the stability over time for the trapped particle.

5.2 Charge stepping experiments

Charge stepping experiments to verify the mass and charge of the nanoparticles are the final step to verify the functionality of the CODE experiment, and ensure both our capacity to measure the mass of the nanoparticles, and validate the trapping of single nanoparticles.

Initial tests for charge stepping were done using our Agilent FRG 702 pressure gauge. This device ionises the atoms or molecules that collide with it, in the case of these experiments, the residual Argon from the trapping procedure. Some of these ionised atoms will reach the trapped nanoparticle, and it will experience charge variation. These tests were done with a trap configuration of $\Omega = 720\,\text{Hz}$, $V_0 = 774.65\,\text{V}$. This trap configuration is optimal for trapping nanoparticles within the range of $500-700\,\text{nm}$ for which a charge step is within the range of $\sim 0.8-5\,\text{Hz}$. Data samples are taken every 100 seconds to ensure that measurements of a charge step are not averaged and lost. The experiment was carried out by powering the pressure gauge in 1-hour cycles with 2-hour delays in between cycles to increase the chance for a charge step event to occur and to differentiate between charge stepping events and other unexpected phenomena.

Fig. 5.2.1 shows the raw measured frequencies for the mass measurement experiment. We see at time 11hrs and time 16hrs, we see the effect of the ions by the variation of the measured frequency. We can process the obtained

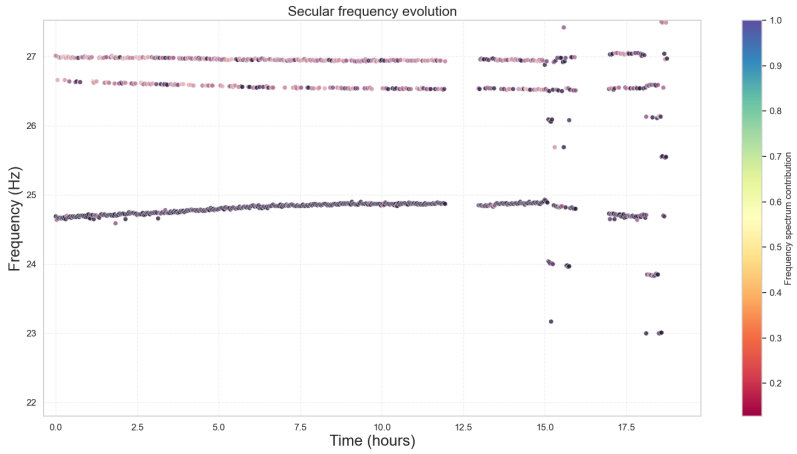

Figure 5.2.1: Frequency peaks of the APD signal for a trapped nanoparticle in the CODE experiment for a charge stepping experiment. The Fourier transform resolution is 0.01Hz pressure gauge is on from hour 15 to 16 and from hour 18 to 19. The colour graph shows the normalised amplitude of the peak in the spectrum.

spectra by curve fitting, via the Python scipy.optimize curvefit module to fit a Lorentzian curve to the spectrum peaks.

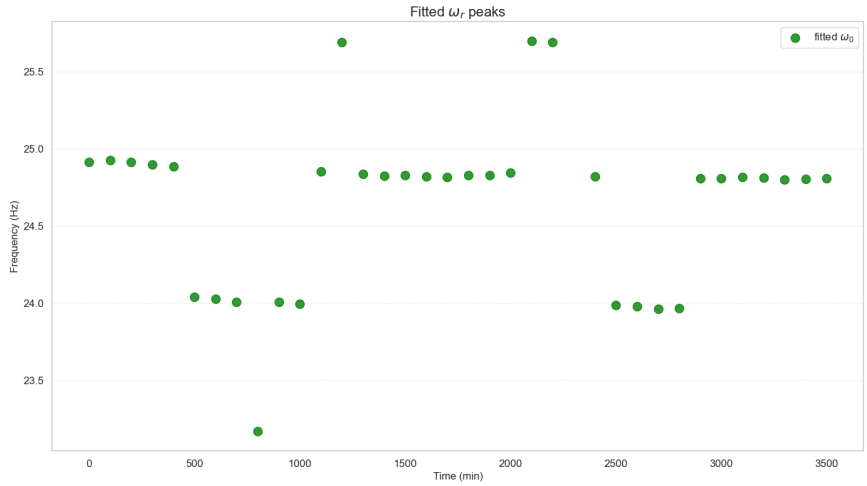

Figure 5.2.2: Fitted ω_r peaks vs time for the charge stepping process, we can see the frequency variation due to changes in charge of the trapped nanoparticle. Trap settings for the experiment where $\Omega = 720Hz$, $V_0 = 1549.3Vpp$

Appendix A4 shows the Programs used for data processing. Once the data is fitted, we can extract the single charge step size. We can see the fitted frequency in Fig. 5.2.2, with the charge steps clearly visible. We see in this charge-stepping process both positive and negative charge steps. Comparing with previous works in charge stepping, such as Schlemmer et al. (2001), where we see their charge

stepping process in Fig. 5.2.3, they attribute this variation to the emission of electrons from the trapped NP.

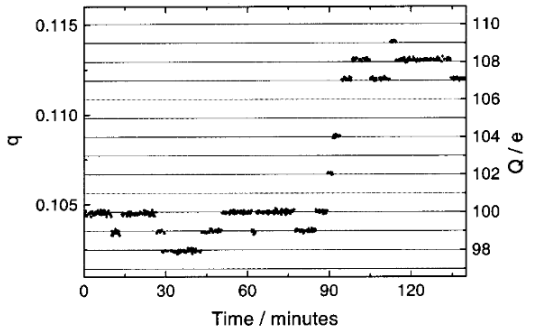

Figure 5.2.3: Charge stepping process from Schlemmer et al. (2001). We see the same process shape of charge stepping in this experiment as seen in the CODE experiment.

We can take the absolute value of each charge step and use the average to calculate the mass of the NP since we know that the charge step is a change of $1e$. We can use equation 3.4.9 to determine the mass of the trapped NP. This method yielded a mass of $M = 5.348 \times 10^{-16} \pm 7.44 \times 10^{-18}$ the mass of a single 160nm nanoparticle is app 4.718×10^{-18} this means that we have a small clump of ~ 54 nanoparticles, while we know that clumping of NP is an unwanted condition, in this case, as mentioned we expected a clump within this range of mass-size to be trapped with this trap settings.

Chapter 6

Experimental Validation & Future Development

6.1 Experimental Validation

The following sections highlight the work done in the CODE experiment that validates the different milestones required for a working mass spectrometer. From trapping ions in vacuum to mass measurements of trapped NPs, the work done in this thesis sets the groundwork for the future of the CODE experiment's scientific data acquisition, measuring desorption energies of species on the surface of trapped nanoparticles.

6.1.1 Trapping in vacuum

We have shown the capacity to trap particles in vacuum for indefinite amounts of time, as shown in fig 6.1.1, where we see stable trapping of NPs for +12 hours with a continuous frequency measured. This has been seen for all particles trapped under vacuum that survive the pressure drop from trapping pressure $5 \times 10^{-3} mbar$ to working pressure at $\sim 1.5 \times 10^{-6} mbar$, with the survivability increasing dramatically with a slow gradient in the pressure change.

It is important to note that constant frequency measurements were achieved after ensuring that the cold cathode pressure gauge was not accidentally changing the charge of the trapped NPs. Fig 6.1.2 shows a particle trapped for multiple days in the ion trap while being affected by the cold cathode gauge, it was initially

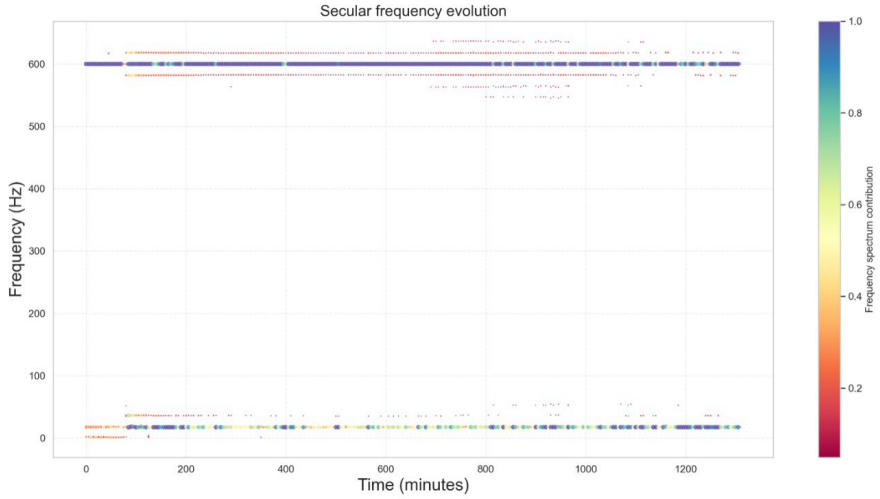

Figure 6.1.1: Trapped nanoparticle in the CODE experiment measurements taken at 2×10^{-6}mbar pressure measurements taken for 20 hours showing consistent frequency measurement.

hipothesized that this frequency shift were due to mass loss from fragmentation (this particle was a purchased nanoparticle see appendix A3 for references) however following work with the system in its final stages showed evidence of charge stepping from pressure gauge ions with a comparable experimental setup.

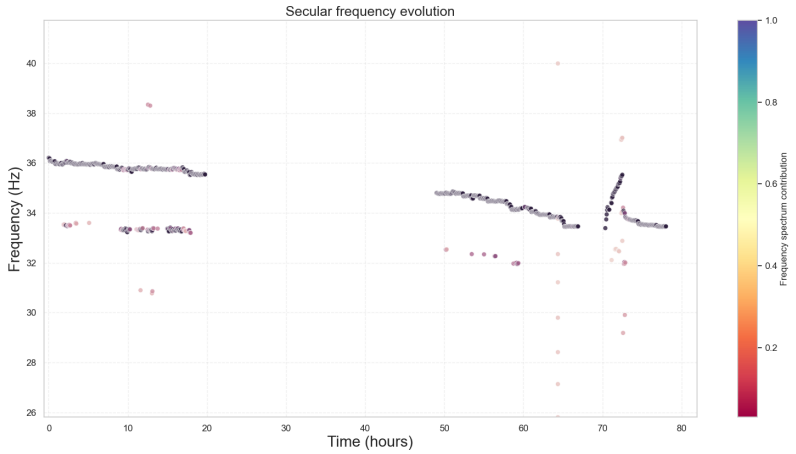

Figure 6.1.2: Secular frequencies for a trapped purchased nanoparticle. Initially, it was hypothesised that the frequency changes were due to mass changes; however, later work revealed that ions generated away from the line of sight can still reach the trapped NPs.

The triboelectric injection system has proved to be an effective method to trap NPs in vacuum; one load of NPs on the brush can be used for +4 injections, with some variation in efficiency depending on the Ω and V_0 selected. The system has

proven to be robust and low-cost; however, this same system can be upgraded by several means. A modification to the vacuum chamber with the system setup within a load-lock to allow recharging the supply of NPs without losing vacuum would be a great improvement to the system, allowing for changing of particles used and brush material. Greater quality and different materials for the brush can improve particle distribution and reduce clumping. The system could also be modified into a vibrating grating made with materials that will induce a charge on the particles via triboelectric charging

6.1.2 Single particle trapping

All frequency spectrums generated by the CODE experiment and images taken with the CCD camera show only a single particle trapped. It is important to understand that this does not necessarily mean that the trapped NP is not a clump, but that we can easily determine if multiple particles or particle clumps are being trapped. In the events when multiple particles were trapped, bombardment ions from the pressure gauge, or electrons from the e-gun, or an extra frequency tone added to the tap voltage, proved effective at removing unwanted ions. Fig. 6.1.3 shows the frequency spectrum of trapped nanoparticles at different times, whilst unwanted additional NPs are being removed from the trap, we see the expected additional peaks at low frequencies caused by interactions between trapped NPs.

When analysing the mass of our trapped NPs, we found that they are concordant with clumps of NPs with masses equivalent to NP size within the range of $600 - 750\,\text{nm}$, rather than individual $160\,\text{nm}$ NPs.

Silica nanoparticles made with the stöber method have a layer of OH as shown in Fig. 6.1.4 from Li et al. (2024). Due to our method of injection, the clumping of the NPs could be explained by the interaction of the OH layers between NPs. This could be solved by the removal of the OH layer via heat; however, we currently only have the capacity to heat our NPs to $220^{\circ}C$, which should reduce the amount of $\text{Si} - \text{OH}$, but it is not sufficient to fully remove this layer. An important update to the experiment would be the capacity to reliably heat the NPs up to $\sim 600^{\circ}\,\text{C}$ before entering vacuum or ideally inside the vacuum chamber to prevent recontamination.

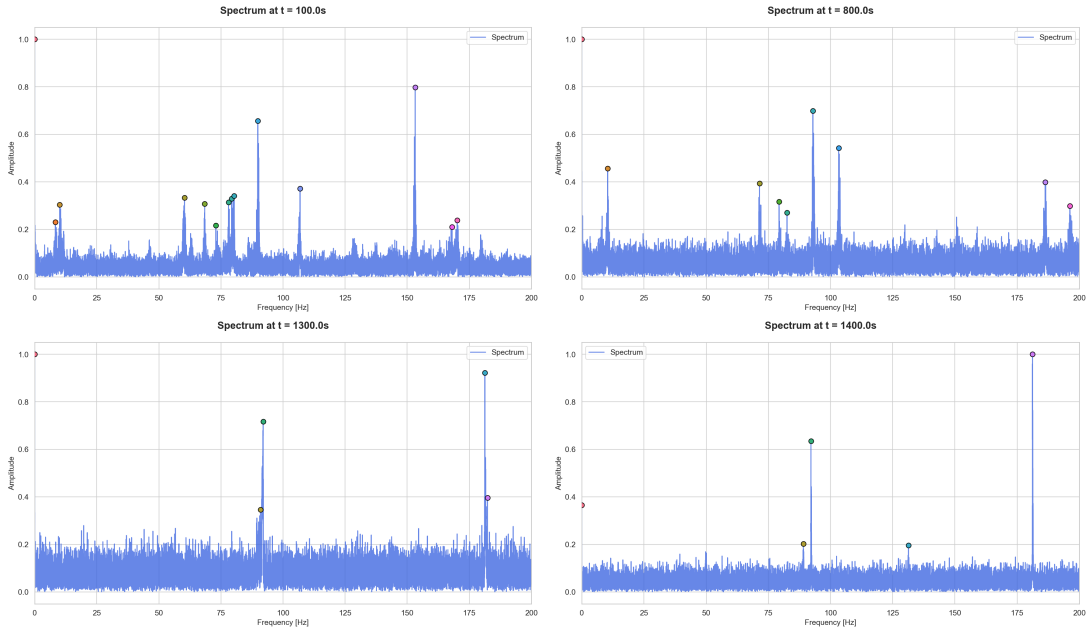

Figure 6.1.3: Spectrum for multiple trapped particles as their are being removed, we can see at time 100s and 800s the presence of multiple frequency peaks, this is an expected behavior of having multiple trapped NPs, we can later see the reduction of peaks to two main peaks, the two $\omega_{n=0}$ secular frequencies of a single trapped ion.

6.1.3 Mass determination

Charge stepping has been successful both with ions from the pressure gauge and with electron bombardment from the electron gun. For this process to work, the system must be set to the fastest frequency acquisition rate of 100s to ensure a single charging process is recorded per spectrum. Our main bottlenecks in mass precision at this time for the CODE experiment are mainly trap geometry and voltage stability. Trap geometry will be improved with the arrival of the PEEK-fabricated SRET trap shown in 6.2.3.

6.2 Future Development

6.2.1 Cryogenic system

To reach our objective of studying binding energies on the surface of dust nanoparticles, it is critical to have a cold environment. This can be achieved with a cryogenic system. We have purchased a cryogenic system for the CODE

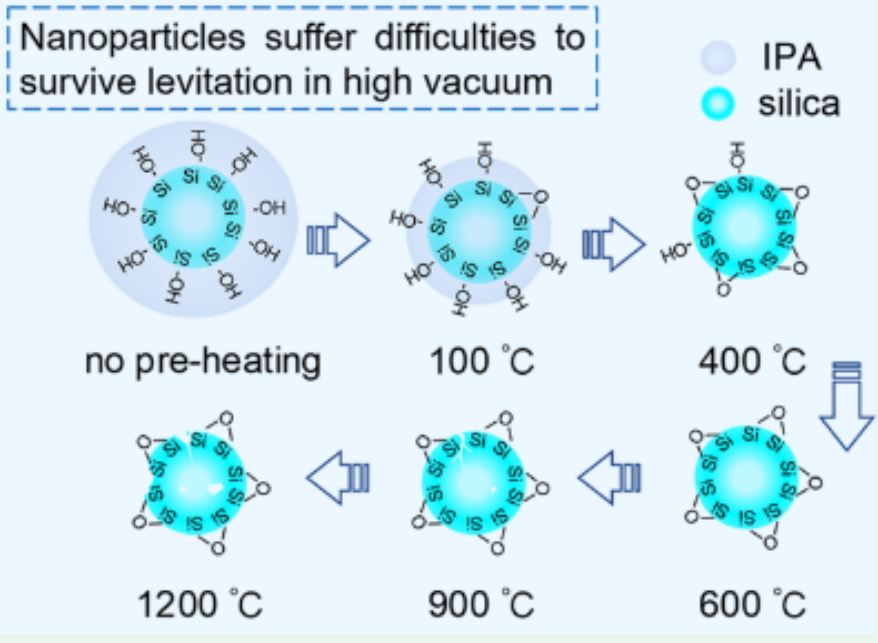

Figure 6.1.4: Representation of the removal of the OH layer from silica as the temperature of the NP increases.

experiment set to be implemented after the scope of this PhD work. The purchased system is a Coldedge CH-104 cold head shown in fig 6.2.1

The CODE experiment setup has a heat load for the cold head within the range of $2.71W$ following our cryostat's heat vs power graph shown in fig 6.2.2.

We are set to reach temperatures within the range of $(25 - 30\text{K})$ with a heating system capable of going up to 355 K. The temperature is controlled using a standard Lakeshore model 335 two-channel temperature controller. The designs for the support of the ion trap system to the cold head are already done and shown in fig 3.2.2, and the manufactured parts are shown in fig 6.2.3, allowing for a simple yet robust connection to the cold head. Additionally, the system allows calibration of both the X,Y planes and the Z axis to allow for corrections due to thermal contraction when the system is in use. The support is easily adaptable to other cold head systems for future updates with more powerful systems.

Figure 6.2.1: The CODE experiments cold head, it is attached from the top with a custom-made adapter that allows for the connection of the trapping system inside.

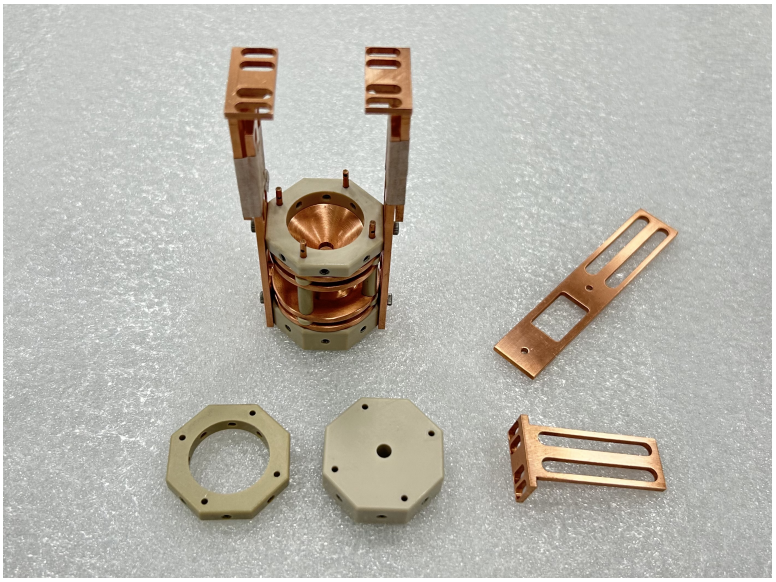

Figure 6.2.3: Trap mounture for the cold head system, manufactured by Shenzen best parts. The dielectric components are made of PEEK plastic.

This improvement will allow us to obtain binding energies from the trapped NP using adsorption isotherms Kumar et al. (2019). We can obtain the isoteric

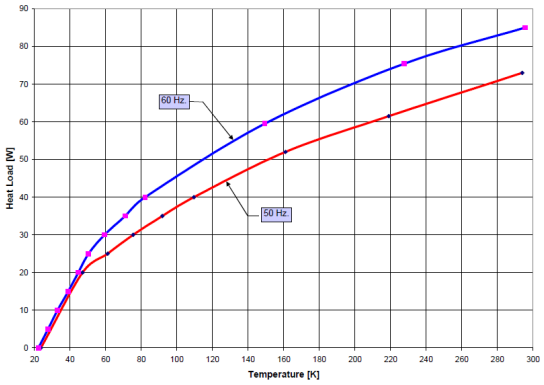

Figure 6.2.2: The Ch-104 heat load graph, with our current heat load of 2.71W, we can see that the expected temperature is within the range of $20 - 30$K

enthalpy of adsorption $\Delta_{ads}H$ that is related to the binding energy of the adsorbed molecules by

$$\Delta_{ads}H = E_b - RT \tag{6.2.1}$$

for a fixed temperature for a mole of adsorbate. Using this process allows us to obtain binding energies for different gases to the surface of the trapped nanoparticles, without the necessity of specifically heating up the nanoparticles, reducing the complexity of binding energy experiments. Additionally, the reduction of temperature inside the vacuum chamber to cryogenic temperatures will increase the vacuum of the system, increasing the sensitivity of the system to the NPs secular frequencies.

6.2.2 Atomic beam lines and surface chemistry

At the moment, the CODE experiment is able to work with 5 different gases using the gas line shown in section 3.1.2. However, as discussed in the introduction, many reactions in the ISM also involve atomic species such as H, O and N. Reactions such as $H + O$ and $H + O_2$, $CO + H$, are of astronomical relevance (Ioppolo et al. (2008), Ioppolo et al. (2011)). Thus one of the future objectives of the CODE experiment is to measure molecule formation on the surface of the trapped NP.

To achieve this goal, the first logical step is to have the capacity to inject atomic species into the vacuum chamber. To inject atomic species into a vacuum system,

an atomic beam source is required. In the case of CODE, we have studied the use of an RF atom source. Fig. 6.2.4 shows the specs for an RF atom source that has been considered for the CODE experiment and can work with multiple gases such as N_2, H_2, Ar, O_2.

	NL-ATS30	NL-ATS60
Mounting flange	NW63CF (4.5" O.D)	NW100CF (6" O.D.)
UHV compatible	Yes, Bakeable up to 250°C	
In-vacuum length	275mm	
In-vacuum diameter	60mm	96mm
Beam diameter	30mm	60mm
Gas Compatibility and discharge tube/aperture plate material	O_2 Quartz, Alumina	
	N_2 PBN, Quartz	
	H_2 Quartz, PBN, Alumina	
	Ar Quartz	
Aperture plate design	0.5mm diameter holes as standard 37 holes as standard (other diameters and number of holes on request)	
Gas Flow	0.1-10Sccm for O_2 and N_2 dependent on aperture plate design	
RF Power	50-300W	50-600W
RF Tuning	Automatic	
Shutter	Manual or Automated	
Cooling	Min Water flow 1.0l/min	
Optical plasma monitoring	Optional	
Ion beam deflection plates	Optional	
Power Supply Specification (Optional)		
RF Power Supply	13.56MHz, 600W (35Amps @ 4.5KV peak) Automatic matching network including controller Forward power metering: +/-1% full scale, +/-1% reading Output power stability: +/0.5% long term, +/-1% Watt Single phase, 100-240VAC, 50/60Hz	
DC Power supply (deflection plates)	Up to 500V, up to 1mA Single phase, 100-240VAC, 50/60Hz	

Figure 6.2.4: Specification for the proposed RF atom source, of the 2 options shown, the ATS30 is preferred due to compatibility with the experiment.

Detecting species on the surface of a NP

Measuring reaction outcomes caused by the injection of atomic and/or molecular species on the surface of a single trapped nanoparticle requires indirect forms of measurement, such as action spectroscopy sketch shown in fig 6.2.5. This method used to study both surface films (Wu et al. (2017) Wu et al. (2018)), and gas phase aggregates (Asmis (2012) Wellman and Jockusch (2015)).

Action spectroscopy uses rare gas atoms such as Argon or Neon as messengers bound to surfaces or aggregates at low temperature. These messengers will desorb when excited by IR radiation in resonance with a vibrational mode of the studied species, using a method to detect the desorbed messenger atoms, such as a quadrupole mass spectrometer. A plot of the rare gas desorption rate vs the IR photon energy will represent a vibration spectrum of the studied gas or surface.

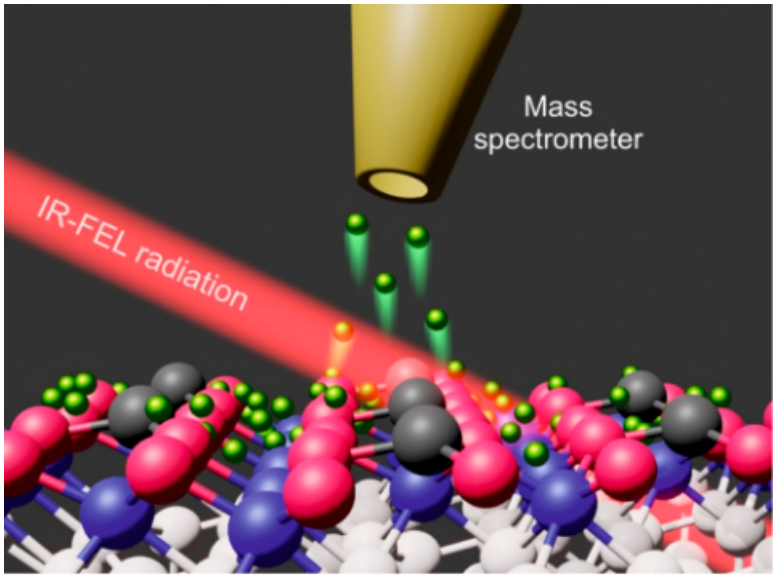

Figure 6.2.5: Sketch of a surface action spectroscopy setup taken from Liu et al. (2020)

Fig. 6.2.6 shows a photon energy vs mass spectrometer intensity graph for an action spectroscopy experiment. The IR radiation used to excite the vibrational mode is generated by a tunable light source such as Free Electron Lasers (FEL) (Liu et al. (2020)) or super continuum lasers (Hoffmann et al. (2020)), to excite individual vibrational or rotational modes for the adsorbed species.

Action spectroscopy can be adapted to be used with our system; however, using tunable light sources such as a FEL is unlikely due to monetary constraints, other tunable photon sources must be considered. Due to the incredibly small amount of material that can be absorbed and then desorbed our system is not able to use traditional standard methods for species detection such as quadrupole mass spectrometers, XPS or IRAS, however, we can use action spectroscopy, as we can measure the mass change of the nanoparticle and its ice layers due to desorption due to vibrational excitation of species.

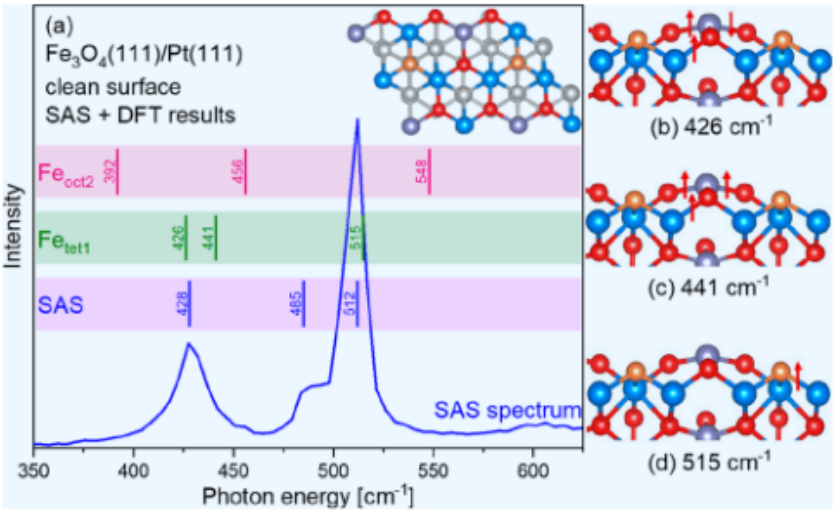

Figure 6.2.6: Photon energy vs mass spectrometer signal intensity, shown are the vibrational modes for Fe_{tet1} and Feoct2 terminations of $Fe_3O_4(111)$

6.3 Conclusion

We have shown the extensive work done to design and build the CODE experiment over the course of this PhD thesis. If we look back at the objectives of the thesis, we see that we were able to implement a system capable of injecting nanoparticles in vacuum into the ion trap and trapping single nanoparticles (with the aforementioned limitations for small nanoparticles), measuring their masses. While we at the moment cannot adsorb species onto the trapped NPs this is only because of time delays on the construction and implementation of the cold head mount for the trapping system. The experiment is able to inject different gases into the vacuum chamber with its gas line, and adsorption is then only a limitation of lowering the temperature of the system.

We can confidently say then that we have successfully built a non-destructive mass spectrometer. While this thesis work might have concluded, as shown in the previous section, there is still much work to be done to fully exploit the capacities of the CODE experiment. We have built the foundations for a promising experimental future to study dust surface chemical processes in an attempt to understand complex organic molecule formation in the interstellar medium.

Bibliography

Arridge, R. G. C. (1967). The static electrification of nylon 66. *British Journal of Applied Physics*, 18(9):1311–1316.

Ashkin, A. (2006). *Optical trapping and manipulation of neutral particles using lasers*. World Scientific, Singapore, reprint volume with commentaries edition.

Asmis, K. R. (2012). Structure characterization of metal oxide clusters by vibrational spectroscopy: possibilities and prospects. *Physical Chemistry Chemical Physics*, 14(26):9270.

Banerjee, S. and Mazumdar, S. (2012). Electrospray Ionization Mass Spectrometry: A Technique to Access the Information beyond the Molecular Weight of the Analyte. *International Journal of Analytical Chemistry*, 2012:1–40.

Bowker, M. (2016). The Role of Precursor States in Adsorption, Surface Reactions and Catalysis. *Topics in Catalysis*, 59(8-9):663–670.

Criscienzo, M. D., Dell'Agli, F., Ventura, P., Schneider, R., Valiante, R., Franca, F. L., Rossi, C., Gallerani, S., and Maiolino, R. (2013). Dust formation in the winds of AGBs: the contribution at low metallicities. *Monthly Notices of the Royal Astronomical Society*, 433(1):313–323. arXiv:1304.7120 [astro-ph].

Cuppen, H. M., Walsh, C., Lamberts, T., Semenov, D., Garrod, R. T., Penteado, E. M., and Ioppolo, S. (2017). Grain Surface Models and Data for Astrochemistry. *Space Science Reviews*, 212(1-2):1–58.

Davies, D. K. (1969). Charge generation on dielectric surfaces. *Journal of Physics D: Applied Physics*, 2(11):1533–1537.

Esser, T. K., Hoffmann, B., Anderson, S. L., and Asmis, K. R. (2019). A cryogenic single nanoparticle action spectrometer. *Review of Scientific Instruments*, 90(12):125110.

Frimmer, M., Luszcz, K., Ferreiro, S., Jain, V., Hebestreit, E., and Novotny, L. (2017). Controlling the net charge on a nanoparticle optically levitated in vacuum. *Physical Review A*, 95(6):061801.

Garrod, R. T. and Herbst, E. (2006). Formation of methyl formate and other organic species in the warm-up phase of hot molecular cores. *Astronomy & Astrophysics*, 457(3):927–936.

Guerreiro, A. N., Costa, I. B., Vale, A. B., and Braga, M. H. (2023). Distinctive Electric Properties of Group 14 Oxides: SiO2, SiO, and SnO2. *International Journal of Molecular Sciences*, 24(21):15985.

Hoffmann, B., Esser, T. K., Abel, B., and Asmis, K. R. (2020). Electronic Action Spectroscopy on Single Nanoparticles in the Gas Phase. *The Journal of Physical Chemistry Letters*, 11(15):6051–6056.

Ioppolo, S., Cuppen, H. M., Romanzin, C., Van Dishoeck, E. F., and Linnartz, H. (2008). Laboratory Evidence for Efficient Water Formation in Interstellar Ices. *The Astrophysical Journal*, 686(2):1474–1479.

Ioppolo, S., Fedoseev, G., Lamberts, T., Romanzin, C., and Linnartz, H. (2013). SURFRESIDE2: An ultrahigh vacuum system for the investigation of surface reaction routes of interstellar interest. *Review of Scientific Instruments*, 84(7):073112.

Ioppolo, S., Van Boheemen, Y., Cuppen, H. M., Van Dishoeck, E. F., and Linnartz, H. (2011). Surface formation of CO2 ice at low temperatures: Surface formation of CO2. *Monthly Notices of the Royal Astronomical Society*, 413(3):2281–2287.

Kammler, T., Kolovos-Vellianitis, D., and Küppers, J. (2000). A hot-atom reaction kinetic model for H abstraction from solid surfaces. *Surface Science*, 460(1-3):91–100.

Kebarle, P. and Verkerk, U. H. (2009). Electrospray: From ions in solution to ions in the gas phase, what we know now. *Mass Spectrometry Reviews*, 28(6):898–917.

Kumar, K. V., Gadipelli, S., Wood, B., Ramisetty, K. A., Stewart, A. A., Howard, C. A., Brett, D. J. L., and Rodriguez-Reinoso, F. (2019). Characterization of the adsorption site energies and heterogeneous surfaces of porous materials. *Journal of Materials Chemistry A*, 7(17):10104–10137.

Li, A. and Draine, B. T. (2012). THE CARRIERS OF THE INTERSTELLAR UNIDENTIFIED INFRARED EMISSION FEATURES: AROMATIC OR ALIPHATIC? *The Astrophysical Journal*, 760(2):L35.

Li, C., Ma, Y., Wang, J., Ying, Q., Zhu, S., Fu, Z., Jiang, X., Yang, H., Liang, T., Gao, X., and Hu, H. (2024). Morphological Tracking and Tuning of Silica Nanoparticles in Optomechanical Systems for Enhanced Stable Levitation in Vacuum. *ACS Applied Nano Materials*, 7(22):25493–25499.

Liu, Y., Wu, Z., Naschitzki, M., Gewinner, S., Schöllkopf, W., Li, X., Paier, J., Sauer, J., Kuhlenbeck, H., and Freund, H.-J. (2020). Elucidating Surface Structure with Action Spectroscopy. *Journal of the American Chemical Society*, 142(5):2665–2671.

March, R. E. and Todd, J. F. J. (2005). *Quadrupole ion trap mass spectrometry*. Number v. 165 in Chemical analysis. J. Wiley, Hoboken, N.J, 2nd ed edition.

Matsusaka, S., Maruyama, H., Matsuyama, T., and Ghadiri, M. (2010).

Triboelectric charging of powders: A review. *Chemical Engineering Science*, 65(22):5781–5807.

Ossenkompf, V. (1993). Dust coagulation in dense molecular clouds: the formation of fluffy aggregates. *Astronomy and Astrophysics*.

Peschke, M., Verkerk, U. H., and Kebarle, P. (2004). Features of the ESI mechanism that affect the observation of multiply charged noncovalent protein complexes and the determination of the association constant by the titration method. *Journal of the American Society for Mass Spectrometry*, 15(10):1424–1434.

Potapov, A., Jäger, C., and Henning, T. (2020). Ice Coverage of Dust Grains in Cold Astrophysical Environments. *Physical Review Letters*, 124(22):221103.

Potapov, A. and McCoustra, M. (2021). Physics and chemistry on the surface of cosmic dust grains: a laboratory view. *International Reviews in Physical Chemistry*, 40(2):299–364.

Sabri, T., Gavilan, L., Jäger, C., Lemaire, J. L., Vidali, G., Mutschke, H., and Henning, T. (2013). INTERSTELLAR SILICATE ANALOGS FOR GRAIN-SURFACE REACTION EXPERIMENTS: GAS-PHASE CONDENSATION AND CHARACTERIZATION OF THE SILICATE DUST GRAINS. *The Astrophysical Journal*, 780(2):180.

Santoro, G., Sobrado, J. M., Tajuelo-Castilla, G., Accolla, M., Martínez, L., Azpeitia, J., Lauwaet, K., Cernicharo, J., Ellis, G. J., and Martín-Gago, J. (2020). INFRA-ICE: an ultra-high vacuum experimental station for laboratory astrochemistry. *Review of Scientific Instruments*, 91(12):124101. arXiv:2011.09297 [astro-ph].

Schlemmer, S., Illemann, J., Wellert, S., and Gerlich, D. (2001). Nondestructive high-resolution and absolute mass determination of single charged particles in a three-dimensional quadrupole trap. *Journal of Applied Physics*, 90(10):5410–5418.

Schlemmer, S., Wellert, S., Windisch, F., Grimm, M., Barth, S., and Gerlich, D. (2004). Interaction of electrons and molecules with a single trapped nanoparticle. *Applied Physics A: Materials Science & Processing*, 78(5):629–636.

Smith, D. P. H. (1986). The Electrohydrodynamic Atomization of Liquids. *IEEE Transactions on Industry Applications*, IA-22(3):527–535.

Stöber, W., Fink, A., and Bohn, E. (1968). Controlled growth of monodisperse silica spheres in the micron size range. *Journal of Colloid and Interface Science*, 26(1):62–69.

Technologies, A. (2011). *HIGH AND ULTRA-HIGH VACUUM FOR SCIENCE RESEARCH*. Agilent Technologies.

Theulé, P., Endres, C., Hermanns, M., Bossa, J.-B., and Potapov, A. (2019). High-

resolution gas phase spectroscopy of molecules desorbed from an ice surface: a proof-of-principle study. arXiv:1912.09839 [astro-ph].

Tielens, A. (2022). Dust Formation in Astrophysical Environments: The Importance of Kinetics. *Frontiers in Astronomy and Space Sciences*, 9:908217.

Torres-Turiján, J., Ortega-Mendoza, J. G., Zaca-Morán, P., Chávez, F., Ramírez-San-Juan, J. C., Ramos-García, R., Zapata-Nava, O. J., and Felipe, C. (2011). Radiation forces on Au nanoparticles considering infrared beams. page 80113Q, Puebla, Mexico.

Ventura, P., Criscienzo, M. D., Schneider, R., Carini, R., Valiante, R., D'Antona, F., Gallerani, S., Maiolino, R., and Tornambé, A. (2012). Dust formation around AGB and SAGB stars: a trend with metallicity?: *Stardust from AGB and super-AGB stars. Monthly Notices of the Royal Astronomical Society*, 424(3):2345–2357.

Wellman, S. M. J. and Jockusch, R. A. (2015). Moving in on the Action: An Experimental Comparison of Fluorescence Excitation and Photodissociation Action Spectroscopy. *The Journal of Physical Chemistry A*, 119(24):6333–6338.

Wu, Z., Płucienik, A., Feiten, F. E., Naschitzki, M., Wachsmann, W., Gewinner, S., Schöllkopf, W., Staemmler, V., Kuhlenbeck, H., and Freund, H.-J. (2017). Vibrational Action Spectroscopy of Solids: New Surface-Sensitive Technique. *Physical Review Letters*, 119(13):136101.

Wu, Z., Płucienik, A., Liu, Y., Naschitzki, M., Wachsmann, W., Gewinner, S., Schöllkopf, W., Kuhlenbeck, H., and Freund, H.-J. (2018). Surface action spectroscopy with rare gas messenger atoms. *Review of Scientific Instruments*, 89(8):083107.

Yocum, K. M., Smith, H. H., Todd, E. W., Mora, L., Gerakines, P. A., Milam, S. N., and Widicus Weaver, S. L. (2019). Millimeter/Submillimeter Spectroscopic Detection of Desorbed Ices: A New Technique in Laboratory Astrochemistry. *The Journal of Physical Chemistry A*, 123(40):8702–8708.

Appendix A

A1 Vacuum

A1.1 Theory of vacuum systems

A1.1.1 Throughput

Throughput is the amount of gas being removed from the vacuum system. It is expressed by the letter Q and has units of Pressure/Time. It is described for passive components (pipes and ports) as :

$$Q = C * (P_1 - P_2) \tag{A1.1}$$

Here, we define the conductance of a component C In the case of active components, we can relate the throughput to the pumping speed:

$$Q = S * P \tag{A1.2}$$

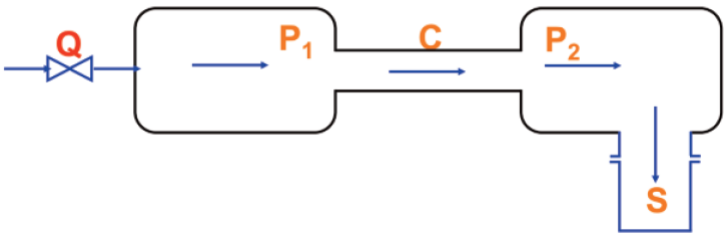

Figure A1.1: Sketch for the throughput of a vacuum system

A1.1.2 Conductance

The conductance of a pipe is directly related to its dimensions and the properties of the gas; it is defined by two different equations according to the flow regime. For a tube of circular cross-section and in the absence of turbulence, The conductance from the Hagen–Poiseuille derivation in the viscous flow regime is:

$$C = 32600 \frac{D^4}{\eta L} P_{av} [Ls^{-1}] \tag{A1.3}$$

where the diameter D and length L of the tube are in centimetres, the average pressure P_{av} is in torr, and the viscosity of the gas η is in micropoise (μP)).

For the case of molecular flow, the conductance of a pipe is defined as:

$$C = \frac{D^3}{L} [Ls^{-1}] \tag{A1.4}$$

In a similar way to electrical theory, the conductance of a complicated array of multiple pipes can be expressed as a single equivalent tube using the network equations:

$$C_{series} = \left[\frac{1}{C_1} + \frac{1}{C_2} + ... \right] \tag{A1.5}$$

$$C_{parallel} = C_1 + C_2 + C_3 + ... \tag{A1.6}$$

By using the network equations, we can reduce a complex vacuum system to a single equivalent conductance as shown in figA1.2 and calculate the net pumping speed of the system

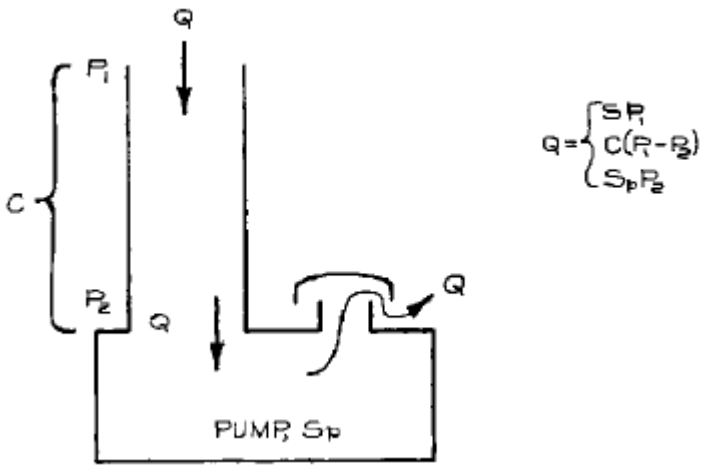

Figure A1.2: Equivalent conductance vacuum system **?**

The net pumping speed is given by:

$$S = \frac{Q}{P_1} \tag{A1.7}$$

and the vacuum pumps pumping speed is

$$S_{pump} = Q/P_2 \tag{A1.8}$$

Since the throughput is the same in all the systems, we can relate these values using Eq. 42, and we get:

$$\frac{1}{S} = \frac{1}{S_{pump}} + \frac{1}{C} \tag{A1.9}$$

A1.1.3 Gas Load

Gas load is the rate gas enters the system volume. It is the sum of multiple phenomena acting in the vacuum system

- Outgassing (desorption): Release of gas that has accumulated on system surfaces when they are exposed to the atmosphere
- Diffusion: Gas particles present in the vessel walls at the start of (initial) pumpdown and released into the system during operation
- Permeation: Gas migrating into the system through the vessel walls from the atmosphere and released into the system during operation
- Process: Gas introduced during process

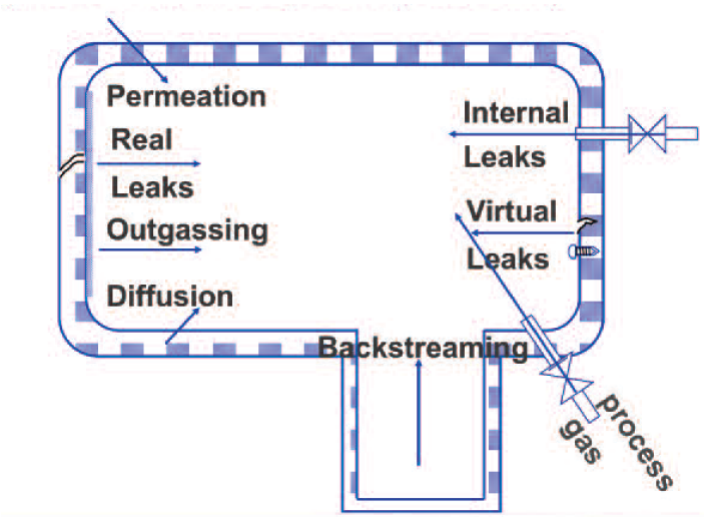

Figure A1.3: Origin of gas load in a vacuum system Technologies (2011)

A1.1.4 Outgassing

It is the rate of gas evolution from solid materials; it depends both on the nature of the solid and the absorbate. A rough, porous, or polar surface adsorbs more gas than a clean, polished surface. The outgassing rate from a surface decreases slowly, roughly as e^{at} (a property of the surface and the adsorbate, as well as a strong function of temperature). Baking a vacuum chamber to 150 to 200 ºC under vacuum will encourage outgassing and result in a lower ultimate pressure after the chamber cools.

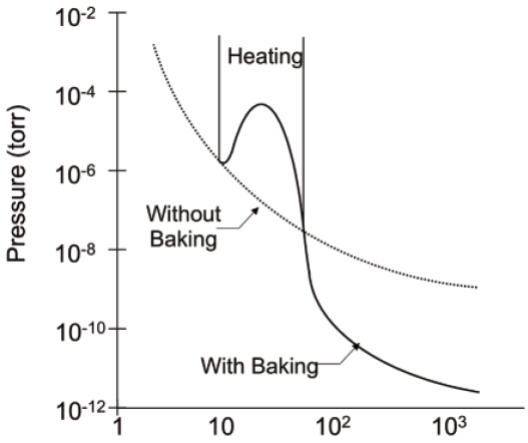

Figure A1.4: Effect of baking on achieved vacuum Technologies (2011)

A1.1.5 Minimum achievable pressure

The gas load of a system can be understood as a throughput and can be used to define the minimum achievable pressure. We can define the gas load as the sum of the throughput of all gas load sources.

$$Q_{gas_load} = Q_{permeation} + Q_{volume} + Q_{Leak} + Q_{diffusion} + Q_{Outgas} + Q_{process} \quad \text{(A1.10)}$$

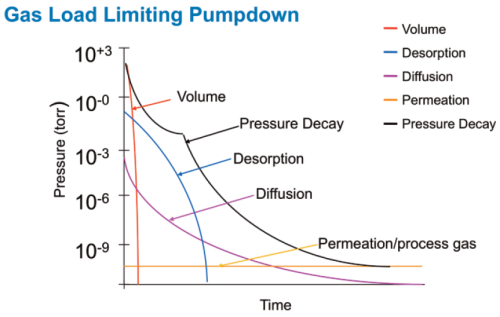

Figure A1.5: Effects on achievable pressure from the different gas load sources

We can use Eq. 43 to determine the minimum pressure by calculating the pressure from the gas load throughput and the system pumping speed

$$P_{minimum} = \frac{Q_{Gas_Load}}{S_{system}} \quad \text{(A1.11)}$$

A1.1.6 Pumping speed

The time required to pump a chamber of volume V from pressure P0 to P is:

$$t = \frac{V}{S} \ln\left(\frac{P_0}{P}\right) \tag{A1.12}$$

However, this equation might deviate from the real time, since it assumes a constant net pumping speed, and only the gas that resided in the container at the start of the pumpdown. For a typical vacuum system that goes down to the molecular flow regime, the equation has to be done in two steps, one for the rough vacuum and one for high-ultra high vacuum

A2 100MHz power supply

The first iterations of the CODE ion trap system featured a Jordan TOF product D-1203 Power supply. This system generates a variable voltage $0 - 4000$Vpp at a fixed 1MHz frequency. The voltage can be controlled with a $0 - 9V$ input voltage. The system was setup and trapping tests were carried out, however this tests where unsuccessful, upon further analysis our initial assumptions mass to charge ratio where off, with our now more accurate values of $\sim$ n $\times$ 10e of charge (again following Schlemmer et al. (2001) and Frimmer et al. (2017)) with this charge values a frequency of $1MHz$ is to high for trapping as the $q_{r,z}$ stability parameter reaches values ~ 0.

Our next step was to attempt to modify the internal system to do this. We had to first simulate the entire D-1203 Power supply to identify the components that needed to be changed in order to change the frequency of the generated voltage. We first calculated a frequency range that is suitable for trapping as our objective frequency. We found that within the range of a few kHz the trap's voltage range $0 - 4000Vpp$ is adequate for trapping our particles. To implement this frequency change, we simulated the entire D-1203 power supply in LTspice; the schematic simulation is shown in Fig. A2.1.

It was determined that the large inductance coil is what drives the frequency of the system. We analysed what value was required for the inductance, and in

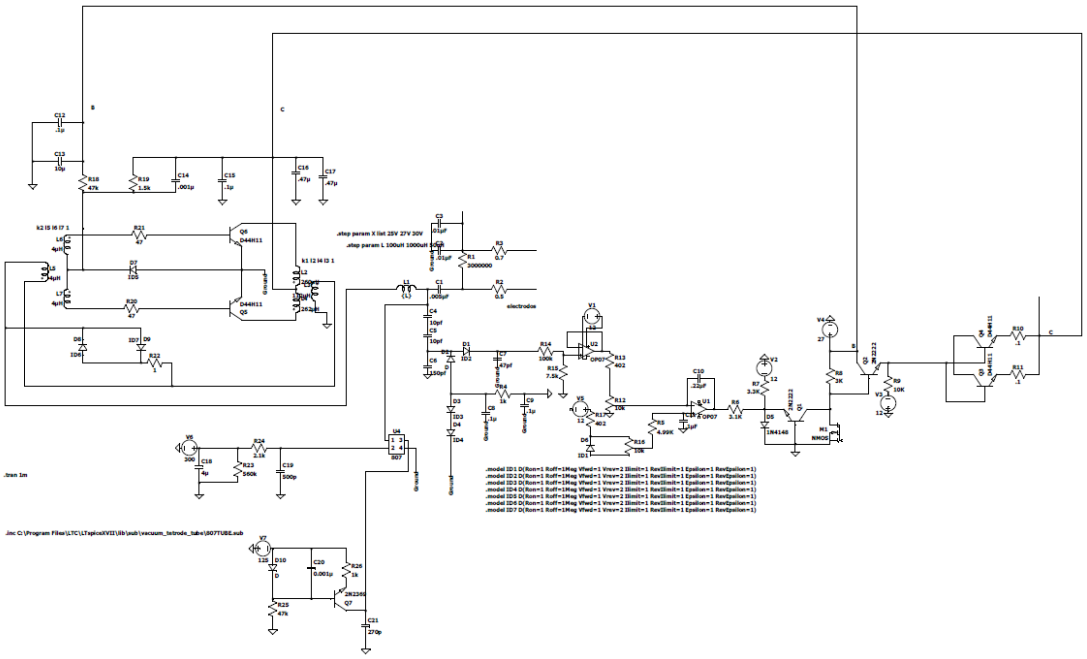

Figure A2.1: LTSpice simulation of the D-1203 Power supply

parallel, we tested varying the inductance of the system to determine if it was feasible to change the frequency of the system without damaging the device and adding unwanted noise to the signal sine wave output. We found that we could not add additional coils to the inductance; rather the we could only add another coil in sequence or decouple the existing coil. Furthermore, to obtain our objective frequency values, the inductance of the coil would have to be modified significantly. A modification of the coil was done, but it proved ineffective, as it destroyed the form of the sine wave signal of the power supply. These results showed us that attempting to modify this device proved a futile endeavour, and we took to the task of finding alternative solutions.

A3 Nanoparticle electron microscope images

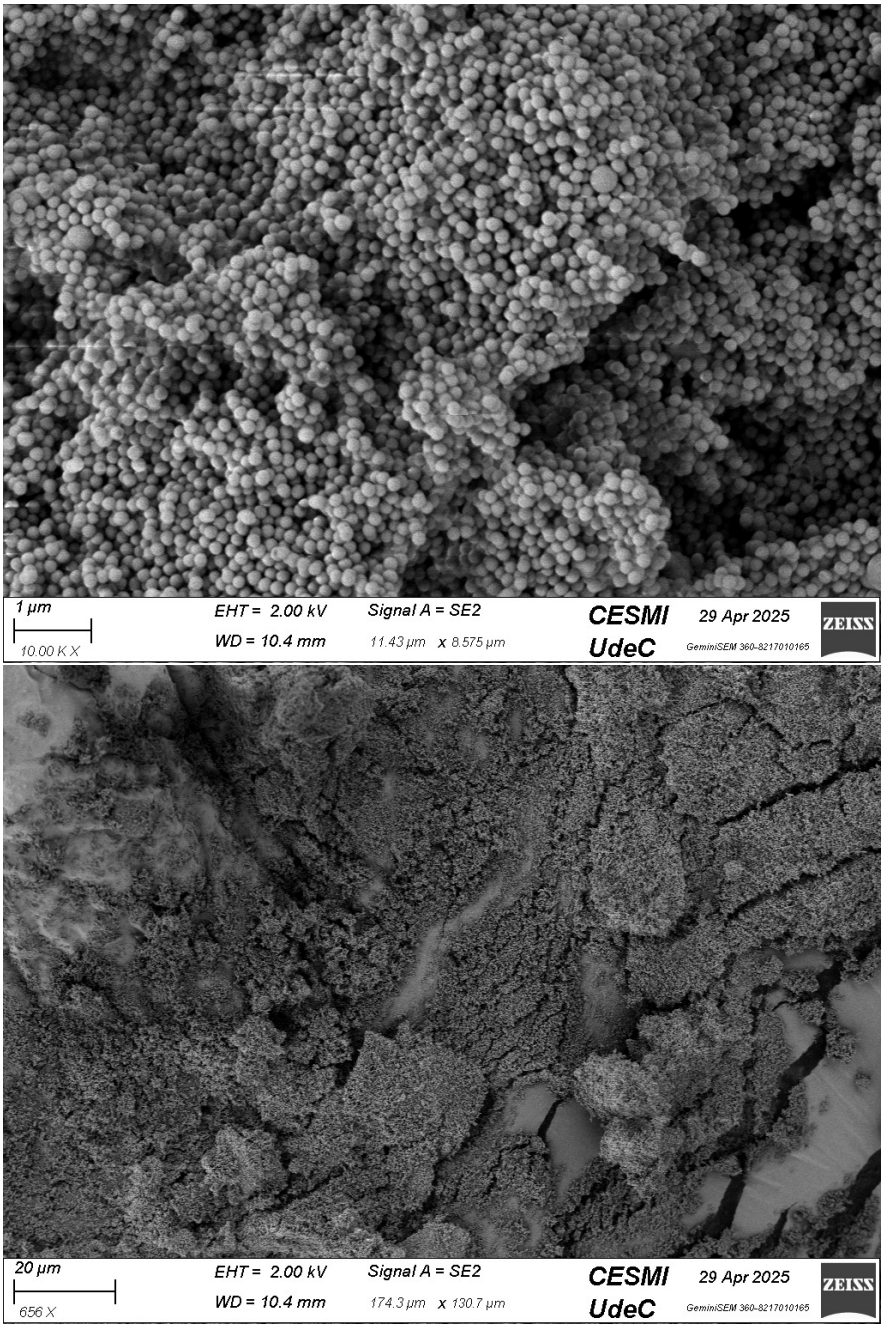

Figure A3.1: Particles made in situ with the Stober method. This sample is first centrifuged and then dried in an oven before deposition for the electron microscope.

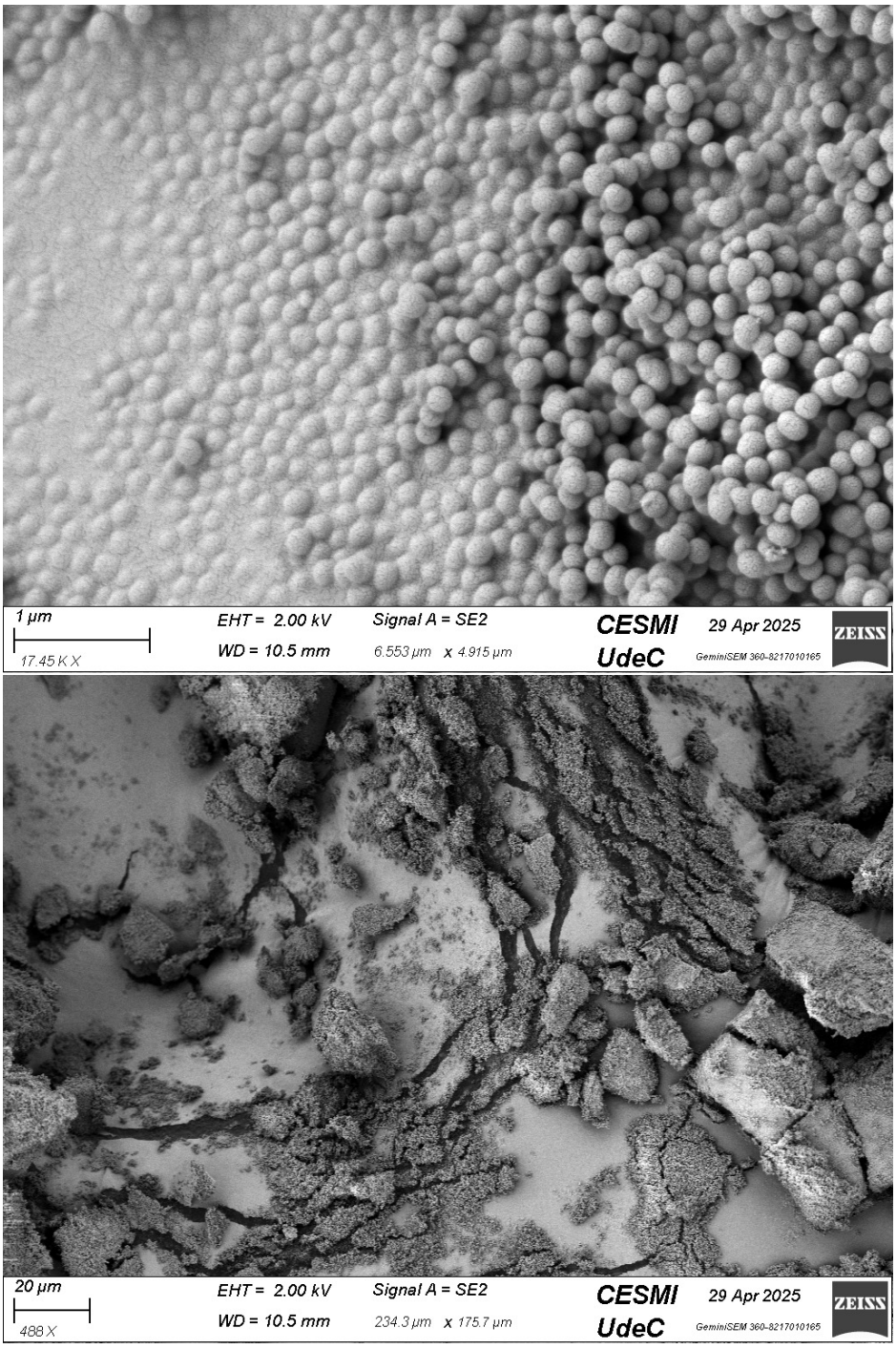

Figure A3.2: Particles made in situ with the Stöber method. This sample was only dried in an oven before deposition.

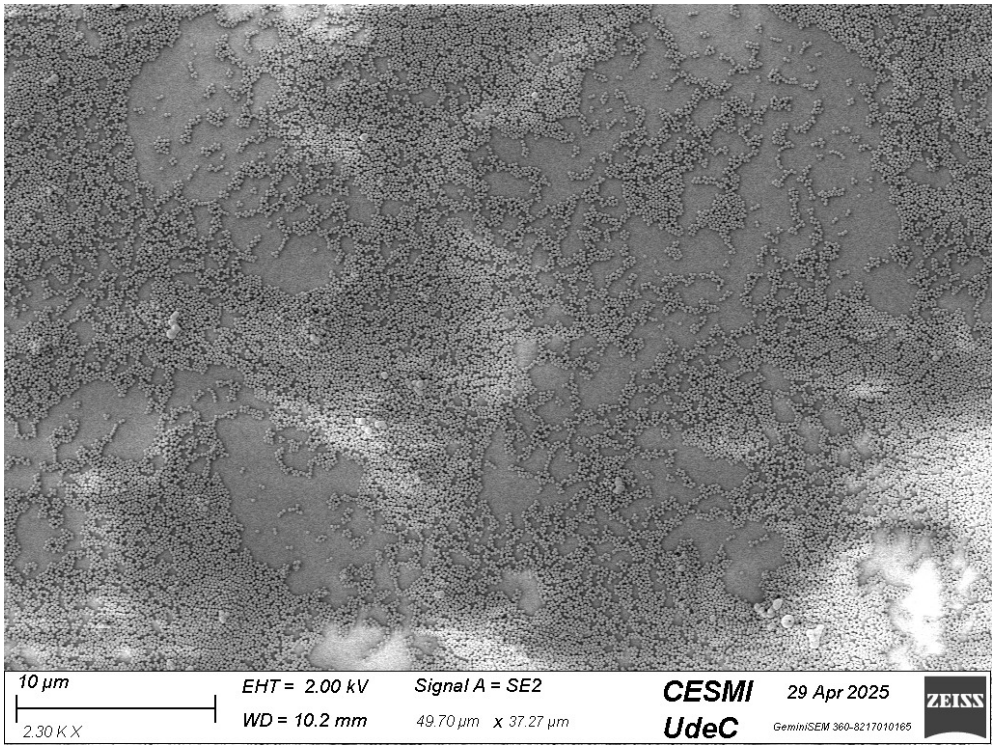

Figure A3.3: Particles made in situ with the Stöber method. This sample was deposited on a glass wafer before being placed in an oven to dry.

A4 Data processing programs

A4.1 Lorentzian fitting for data files program

```
    # -*- coding: utf-8 -*-
"""
Created on Tue Jul 22 13:27:43 2025

@author: N_Mar
"""


# -*- coding: utf-8 -*-
from uncertainties import ufloat
import numpy as np
import h5py
import matplotlib.pyplot as plt
import seaborn as sns
# import scipy.signal as spy
```

```
import pandas as pd
import os
# import glob
from tqdm import tqdm
import peakutils
import matplotlib.cm as cm
from scipy.optimize import curve_fit
from lmfit.models import LorentzianModel
from itertools import zip_longest
# ============================================================================
# CONFIGURATION
# ============================================================================
sns.set(style="whitegrid", palette="colorblind", font_scale=1.1,
        rc={"figure.figsize": (10, 6), "axes.titlesize": 14, "axes.labelsi

# Physical constants
OMEGA_TRAP = 720    # Hz
R_O = 5.22          # mm
Z_O = 3.691         # mm
V_O = 270           # Volts
V_DC = 0

# Analysis parameters
INITIAL_FREQ = 23
FINAL_FREQ = 26
FREQ_STEP = 0.01




FREQ_TOLERANCE = 0.5
MIN_AMPLITUDE_RATIO = 0.1
 multiplier=3
# File processing
INPUT_DIR = "charge_stepping_fast"
OUTPUT_DIR = "resultscharge_stepping_fast"
CREATE_SUBDIRS = True
```

```
# Precomputed indices
LOW_IDX = int(INITIAL_FREQ / FREQ_STEP)
HIGH_IDX = int(FINAL_FREQ / FREQ_STEP)
region_frequencies = np.arange(INITIAL_FREQ, FINAL_FREQ, FREQ_STEP)
region_frequencies_for_lorentz = np.arange(INITIAL_FREQ, FINAL_FREQ, FREQ_STEP/10



file_name = "single_particle_charge_isolated_1_-_2025-10-03_095854.h5"
print(f"\nProcessing {file_name}...")

# Create output directory
output_dir=OUTPUT_DIR
file_output_dir = os.path.join(output_dir, file_name) if CREATE_SUBDIRS else outp
os.makedirs(file_output_dir, exist_ok=True)

# Data containers - using dynamic band names
time_stamps = []
# band_data = {name: [] for name in BAND_NAMES}
# frequency_lines = {name: [] for name in BAND_NAMES}
file_path=INPUT_DIR+"\\" + file_name
absolute_times = []  # Store absolute timestamps



def lorentzian(omega, A, omega0, Gamma, C):
    return C + (A * (Gamma/2)**2) / ((omega - omega0)**2 + (Gamma/2)**2)

#omega =x, omega0 centre A amplitude Gamma width, C offset
Lor_peaks=[]
frequency_lines=[]
try:
    with h5py.File(file_path, 'r') as F:
        # Check if 'FFT' dataset exists
        if 'FFT' not in F:
            print(f"Error: 'FFT' dataset not found in {file_path}")
```

```
first_time = F['FFT'][0][0]
num_records = len(F['FFT'])


for i, fft_data in enumerate(tqdm(F['FFT'], desc=file_name, total=
    timestamp, full_fft = fft_data
    time_val = timestamp - first_time
    time_stamps.append(time_val)

    # Extract frequency region
    region = full_fft[LOW_IDX:HIGH_IDX]
    # region = (region-region.min())/(region.max()-region.min())
    peaks_lor_1=[]
    peaks_lor_2=[]
    # Detect peaks with robust error handling
    try:
        avg_height=np.mean(region)
        avg_height_norm = np.mean((region-region.min())/(region.ma
        peak_indexes=peakutils.indexes(region,thres=avg_height_norm
        peak_indices = peak_indexes
        peak_amps = region[peak_indexes]
        peak_freqs = region_frequencies[peak_indexes]
        #lets try to fit a Lorentzian to the observed peak

        #First we must give initial parameters to the fitting fucn
        try:
            p0=[peak_amps[np.argmax(peak_amps)],peak_freqs[np.argm
            bounds=([0,INITIAL_FREQ,0.01,0],[1,FINAL_FREQ,1,np.mea
            popt, pcov = curve_fit(lorentzian, region_frequencies,
            A_fit, omega0_fit, Gamma_fit, Base = popt

            #compare second function
            # Lor= LorentzianModel()
            # Lor.set_param_hint('amplitude',min=avg_height,max=1-
            # Lor.set_param_hint('center',min=INITIAL_FREQ,max=FINA
            # Lor.set_param_hint('sigma',min=0.01,max=1)
```

```
            # guess=Lor.guess(region,x=region_frequencies)
            # fit=Lor.fit(region,guess,x=region_frequencies)
            L_peaks=float(omega0_fit)
            L_peaks_amps=float(A_fit)
            Lor_peaks.append((L_peaks,L_peaks_amps,float(time_val)))
        except Exception as e:
            print(f'error generating lorentzian fit at time {time_val}s:
            Lor_peaks.append((peak_freqs[0],peak_amps[0],time_val))


        peaks = list(zip_longest(peak_freqs, peak_amps))

    except Exception as e:
        print(f"Error detecting peaks at time {time_val}s: {e}")
        peaks = []

    # Categorize peaks into bands using the dynamic names
    for freq, amp in peaks:
        frequency_lines.append((freq, amp ,time_val))



    # Create spectrum plot periodically (every 5% of timepoints)
    if i % max(1, num_records // 20) == 0:
        try:
            fig, ax = plt.subplots(figsize=(12, 7))
            title = f"{file_name} - Spectrum at t = {time_val:.1f}s"
            fig.suptitle(title, fontweight='bold')

            # Plot spectrum
            sns.lineplot(x=region_frequencies, y=region, ax=ax,
                         color='royalblue', alpha=0.8, label='Spectrum')
            plt.axhline(y=avg_height*multiplier,linestyle='--',color='bla
            # Plot peaks with colors by band
            colors = sns.color_palette("husl", len(peaks))
            for freq, amp in peaks:
                ax.scatter(freq, amp, color=colors[peaks.index((freq,amp)
                # print(freq,amp)
```

```
                    # Remove duplicate legend entries
                    ax.plot(region_frequencies_for_lorentz,lorentzian(regio
                    # ax.plot(region_frequencies,fit.best_fit,color='red',
                    handles, labels = ax.get_legend_handles_labels()
                    unique_labels = dict(zip(labels, handles))
                    ax.legend(unique_labels.values(), unique_labels.keys()


                    ax.set_xlabel('Frequency [Hz]')
                    ax.set_ylabel('Amplitude')
                    ax.set_xlim(INITIAL_FREQ, FINAL_FREQ)
                    # sns.despine(offset=5, trim=True)

                    plt.tight_layout()
                    plt.savefig(os.path.join(file_output_dir, f'spectrum_{
                                dpi=150, bbox_inches='tight')
                    plt.close()
                except Exception as e:
                    print(f"Error creating spectrum plot at time {time_val


except Exception as e:
    print(f"Error processing file {file_path}: {e}")

# Save frequency line data with empty band handling
try:
    band_df = pd.DataFrame({
        'time': [t for f, a, t in frequency_lines],
        'frequency': [f for f, a, t in frequency_lines],
        'amplitude': [a for f, a, t in frequency_lines]
    })
    # Sanitize filename
    band_df.to_csv(os.path.join(file_output_dir, f"{file_name}_Raw_peaks.c
except Exception as e:
    print(f"Error saving data for {file_name} : {e}")
```

```
try:
    Lor_data=pd.DataFrame({
        'time':[t for f,a,t in Lor_peaks ],
        'Lor_fit_1':[f for f,a,t in Lor_peaks],
        'Amp_fit_1':[a for f,a,t in Lor_peaks],
        })
    Lor_data.to_csv(os.path.join(file_output_dir,f"Lor_fit_{file_name}.csv"))
    print("Fitted data saved")
except Exception as e:
    print(f'Error saving Lorentzian {file_path}: {e}')

band_df['Time (min)']=band_df['time']/60

try:
    plt.figure(figsize=(14, 8))

    sns.set_color_codes(palette='deep')
    # Plot with unique color and style
    sns.scatterplot(
        data=band_df,
        x='time',
        y='frequency',
        palette='Spectral',
        hue='amplitude',
        s=100,
        alpha=0.8,
        legend=False

    )

    plt.scatter(Lor_data['time'],Lor_data['Lor_fit_1'],color='green',s=100,alpha=

    norm = plt.Normalize(region.min(), region.max())
    sm = cm.ScalarMappable(cmap='Spectral', norm=norm)
    sm.set_array([])
    cbar = plt.colorbar(sm,ax=plt.gca())
```

```
    cbar.set_label('Frequency spectrum contribution')
    # Add plot decorations
    plt.title(r'Fitted $\omega_r$ peaks', fontsize=16)
    plt.xlabel('Time (min)')
    plt.ylabel('Frequency (Hz)')
    plt.legend()
    plt.grid(alpha=0.3, linestyle='--')



    # Add horizontal grid lines only
    plt.gca().xaxis.grid(False)
    plt.gca().yaxis.grid(True)

    # Improve layout
    plt.tight_layout()
    plt.savefig(os.path.join(OUTPUT_DIR, f"{file_name}_fitted_data.png"),


    print(f"Created combined band plot for {file_name}")
except Exception as e:
    print(f"Error creating combined band plot: {e}")


#Lets make a delta frequency graph

delta_freq=[]

for a in range(0,len(Lor_peaks)-1):
    delta_freq.append((abs(Lor_peaks[a+1][0]-Lor_peaks[a][0]),Lor_peaks[a]


delta_df=pd.DataFrame({
    'time':[t for f,t in delta_freq],
    'frequency':[f for f,t in delta_freq]
    })
delta_df.to_csv(os.path.join(file_output_dir,f"step_size_{file_name}.csv")
```

```
try:
    plt.figure(figsize=(14, 8))

    # Plot with unique color and style
    sns.scatterplot(
        data=delta_df,
        x='time',
        y='frequency',
        s=100,
        alpha=0.8,
        legend=False

    )

    plt.xlabel('Time (min)')
    plt.ylabel('Frequency (Hz)')
    plt.grid(alpha=0.3, linestyle='--')
    plt.title('Absolute value of stepsize', fontsize=16)


    # Add horizontal grid lines only
    plt.gca().xaxis.grid(True)
    plt.gca().yaxis.grid(True)

    # Improve layout
    plt.tight_layout()
    plt.savefig(os.path.join(OUTPUT_DIR, f"{file_name}_step_size.png"), dpi=150)
except Exception as e:
    print(f"Error creating stepsize plot: {e}")


############################################################
############## CALCULATE MASS FROM STEPS ###########
############################################################

#Lets take the steps from non steps
step_mask= delta_df['frequency'] > delta_df['frequency'].mean()
```

```
#transform into radians
steps_value=delta_df[step_mask]*2*np.pi


#calcualte the value from various steps and get the deviation
average_value_steps=steps_value['frequency '].mean()
std_value_steps=steps_value['frequency '].std()

calculated_step=ufloat(average_value_steps,std_value_steps)

#we will assume that this step is a single charge step

#we will need a few variables
rho_particle = 2.2e3
e_charge=1.602176634E-19 #1 electron charge in coulomb [C]
OMEGA_TRAP = 720*np.pi*2    # Hz
R_O = 5.22/1000             # m
Z_O = 3.691/1000            # m
V_O = 1549.3/2              # Volts
V_DC = 0


#lets hold them in a comvenient form
Constant=np.sqrt(2)*V_O/(OMEGA_TRAP*Z_O**2*2)



mass= e_charge*Constant/calculated_step

particle_volume=(mass/rho_particle)

particle_diameter=(((particle_volume*3/(4*np.pi))**(1/3))*1E9)*2

q_r=Lor_data['Lor_fit_1'][0]*2*np.pi/OMEGA_TRAP
```

```
Initial_charge=Lor_data['Lor_fit_1'][0]*2*np.pi*mass/Constant/e_charge


print(f'Program finished mass calculation done. Particle diameter is {particle_di
print(f'Particle initial charge is {Initial_charge}, q_r parameter {q_r}')
```